MICROFLUIDIC CELL SEPARATION BASED ON CELL STIFFNESS

A Dissertation
Presented to
The Academic Faculty

by

Gonghao Wang

In Partial Fulfillment
of the Requirements for the Degree
Doctor of Philosophy in the
School of Mechanical Engineering

Georgia Institute of Technology
December 2014

MICROFLUIDIC CELL SEPARATION BASED ON CELL STIFFNESS

Approved by:

Dr. Todd Sulchek, Advisor
School of Mechanical Engineering
Georgia Institute of Technology

Dr. Alexander Alexeev
School of Mechanical Engineering
Georgia Institute of Technology

Dr. Wilbur Lam
School of Biomedical Engineering
Georgia Institute of Technology

Dr. Hang Lu
School of Chemical and Biomolecular Engineering
Georgia Institute of Technology

Dr. Peter Hesketh
School of Mechanical Engineering
Georgia Institute of Technology

Date Approved: 10. 02. 2014

I dedicate my five-year journey in cell separation to my parents and to my advisor Todd Sulchek.

Thanks to my understanding parents for their endless support and believing in me.

I am fortunate to work on a research topic that I truly enjoyed. Thanks to my advisor Dr. Sulchek for allowing me to select the research project before I arrived at Georgia Tech. I am thankful for his unique approach in guidance and encouragement. His influences will have a lasting impact on my life perspective.

ACKNOWLEDGMENTS

I acknowledge the following for their contributions:

- Todd Sulchek for advising the project, for his ingenuity, and valuable guidance in cell separation research.
- National Science Foundation for funding portions of the research (Project number CBET-0932510)
- Technological Innovations: Generating Economic Results (TI:GER) program at Georgia Tech and Emory University for funding portions of the research and for discovering market potentials of the research.
- Alexander Alexeev for his valuable insight and helpful discussions on fluid dynamics and cell mechanics and contributions to the numerical models of cell separation.
- Wilbur Lam for this helpful suggestions and stimulating discussions.
- Hang Lu for her valuable advice and help in microfluidic channel designs.
- Peter Hesketh for his helpful discussion and suggestions.
- Wenbin Mao for his help in cell modelling and numerical simulations.
- Jessica Walling, Jimmy He, Ernesto Escobar and Gwen Kui (TI:GER team members) for motivating real-world applications, for organizing customer interviews and identifying potential markets for the microfluidic cell sorters.
- David Hu for generous use of his high-speed camera.
- Kipp Schoenwald for his help in microfabrication and SEM imaging and discussions.
- Tom Bongiorno for his help with stem cell preparation and sorting.
- Patricia Pacheco for her help with cell culture and storage.
- Undergraduate students: Caitlin Henegar, Karan Patel, Krishna Patel, Rebecca Byler, Kaci Crawford and Cory Turbyfield for cell culture and AFM cell mechanics measurements.

TABLE OF CONTENTS

LIST OF TABLES

LIST OF FIGURES

LIST OF SYMBOLS AND ABBREVIATIONS

E	Young's modulus
δ	Indentation
n	Sample size
α	Microfluidic channel ridge angle
h	Microfluidic channel gap size
L	Microfluidic channel ridge spacing
B	Microfluidic channel ridge width
H	Microfluidic channel height
l	Microfluidic channel length
w	Microfluidic channel width
F_D	Hydrodynamic (drag) force
F_R	Elastic force
U	Energy associated with cell compression
G'	Storage modulus
G"	Loss modulus
υ	Poisson's ratio
d	Cell diameter
D	Microfluidic channel hydraulic diameter
Δy	Lateral/transverse cell displacement per ridge
S	Amount of cell deformation: cell diameter less channel gap size
η	Strength of secondary flow: the volumetric flow rate ratio between lateral and axial flows
β	Microfluidic channel sheath flow inlet angle
ΔP	Pressure difference between channel inlet and outlet
Q	Volumetric flow rate of the channel

AFM	Atomic force microscope/microscopy
BioMEMs	Biomedical micro-electromechanical systems
BSA	Bovine serum albumin
c.e.f.	Cell enrichment factor
CTC	Circulating tumor cells
CytoD	Cytochalasin D
DEP	Dielectrophoresis
DMEM	Dulbecco's Modified Eagle's Medium
DPBS	Dulbecco's Phosphate-Buffered Saline
FACS	Fluorescence-activated cell sorter
FBS	Fetal bovine serum
fps	Frames per second
LIF	Leukemia inhibitory factor

MACS	Magnetic-activated cells sorter
mEF	Mouse embryonic fibroblast cell
mESC	Mouse embryonic stem cell
PR	Photoresist
PDMS	Polydimethylsiloxane
PMMA	Poly(methyl methacrylate)
RBC	Red blood cells
SEM	Scanning electron microscope/microscopy
WBC	White blood cells

SUMMARY

Cell biophysical properties are a new class of biomarkers that can characterize cells into subgroups that indicate differences in phenotypes that may correlate with disease and cell state. Microfluidic biophysical cell sorters are platforms that utilize these newly developed biomarkers to expand biomedical capabilities for improvements in cell state detection and characterization. Cell biophysical properties are important indicators for cell state and function because they point to differences in cell structures, such as cytoskeletal arrangement and nuclear content. In particular, some diseases, such as cancer and malaria, can cause significant changes in cell biophysical properties. Therefore, cell biophysical properties have the potential to be used for disease diagnostics. Microfluidic systems which can interrogate these biophysical properties and exploit changes in biophysical properties to separate cells into subpopulations will provide important biomedical capabilities.

In this combined theoretical and experimental investigation, we explore a new type of cell sorter which utilizes differences in biophysical properties of cells. These biophysical properties that can be utilized to sort cells include size, elasticity and viscosity. We invented a microfluidic system for continuous, label-free cell separation that utilizes variations in cell biophysical properties. A microfluidic channel is decorated by periodic diagonal ridges that are designed to compress flowing cells in rapid succession. The physical compression, in combination with hydrodynamic secondary flows induced by the ridged microfluidic channel, translates each cell perpendicular to the channel axis in proportion to its biophysical properties. Through careful experimental and computational studies, we found that the cell trajectories in the microfluidic cell sorter correlated to these biophysical properties. Furthermore, we examine the effect of channel design parameters under various experimental conditions to derive cell

separation models that can be used to qualitatively predict cell sorting outcome. A variety of biophysical measurement tools, including atomic force microscopy and high-speed optical microscopy are used to directly characterize the heterogeneous population of cells before and after separation. Taken together, we describe the physical principles that our microfluidic approach can be effectively used to separate a variety of cell types.

The major contribution is the creation and characterization of a novel microfluidic cell-sorting platform that utilizes cell biophysical properties to enrich cells into phenotypic subtypes. This innovative approach opens new ways for conducting rapid and low-cost cell analysis and disease diagnostics through biophysical markers.

CHAPTER 1

INTRODUCTION

In this chapter, we start by giving an overview of the invention and development of cell separation technologies. Next, we discuss the significance of our research in microfluidic cell sorting which utilizes differences in cell biophysical property. Lastly, we will provide an outline of the thesis.

1.1 A Brief History and Development of Cell Separation

Cell separation is an analytical method that classifies cells from a mixture of populations into subgroups that share one or more common properties (Figure 1.1). The origin of cell separation can be traced back to 1940s when Wallace H. Coulter discovered the famous "Coulter Principle". Although the "Coulter Principle" is not directly used for sorting cells, it lays the foundation for counting cells in fluid. He was later awarded a U.S. patent, "Means for Counting Particles Suspended in a Fluid"[1] in 1953 for counting and sizing particles in suspended fluid. A decade later, Mack Fulwyler invented and developed the first prototypes of today's flow cytometers and published his work in "*Science*" journal. In 1970s, the first commercial fluorescence activated cell sorter (FACS) was released by Becton Dickinson.

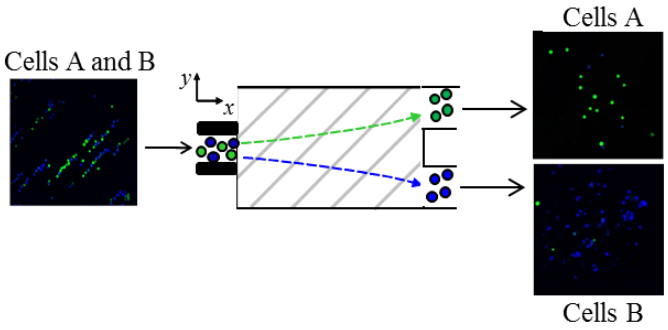

Figure 1.1. A cell-sorting schematic. The initial cell mixture contains two cell types that have difference in cell properties. The device exploits the difference to sort cells.

Prior to the advent of FACS, cell separation is mainly achieved through centrifugation which exploits size and/or density differences among cell types. The most common usage of this technique is to separate white blood cells from red blood cells. However, separation by size and/or density is limited since many cell types have similar size and/or density, yet differ in other properties such as surface proteins. Moreover cell separation through centrifugation is a batch process whereas FACS permits continuous cell separation using multiple cell parameters simultaneously.

Since the debut of FACS, it has proven to be one of the most powerful analytical tools for studying and isolating cells for many applications in research[2,3] and clinical settings[4,5]. Although many innovations have been developed over the last half century, the essential features of the FACS remain unchanged. A typical FACS is composed of a flow cell which carries and aligns the cell samples into a thin fluid stream, a detection system which commonly employs laser beams to emit fluorescent light signals which can be detected, a data collection system and an actuation system that sort cells according to the fluorescent signals (Figure 1.2a). Figure 1.2b

shows a commercially available cell sorting system manufactured by BD. Since the FACS sort cells using florescent signals, cells need to be labelled with antibodies in advance.

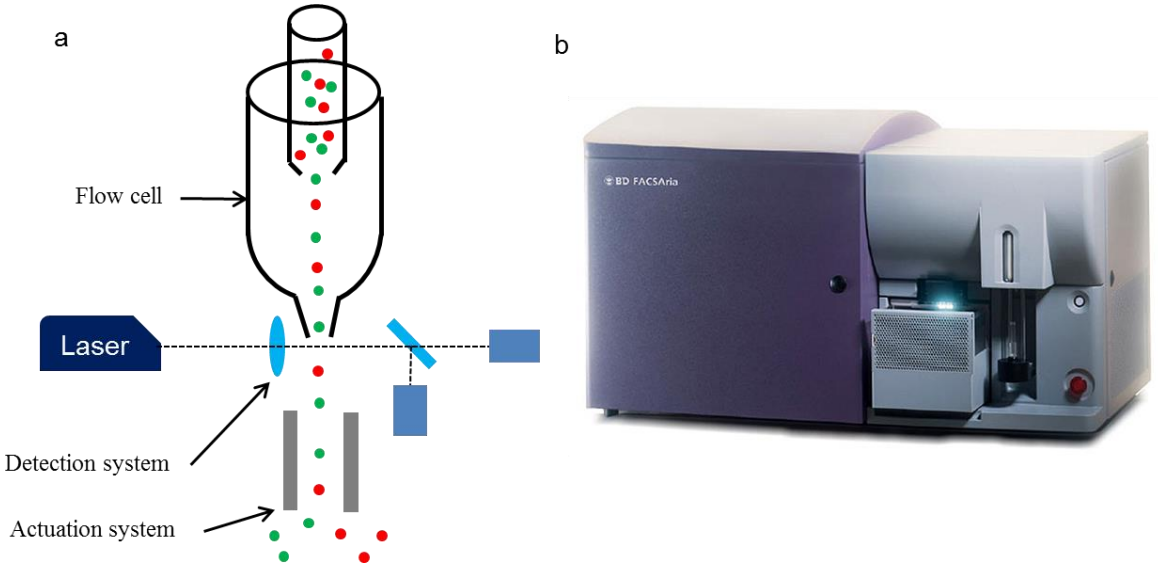

Figure 1.2. Commercially available cell sorting systems. a) Fluorescence activated cell sorter (FACS). b) FACSAria™ by BD: a commercially available bench top FACS.

An alternative cell separation approach called magnetic activated cell sorter (MACS) emerged in the 1980s. Magnetic beads are attached to selected cells and magnetic force is used to separate the cells. Unlike FACS which relies on laser and fluorescence, the MACS utilizes externally applied magnetic field and antibody coated magnetic particles to extract target cells from a mixture in suspended fluid (Figure 1.3a). MACS enabled both negative and positive selection. Due to this feature, MACS gained tremendous popularity in the life science industry and has become a standard procedure in many hospitals and research labs. Figure 1.3b shows the FDA-approved MACS that isolates rare circulating tumor cells from blood samples of patients with advanced cancers.

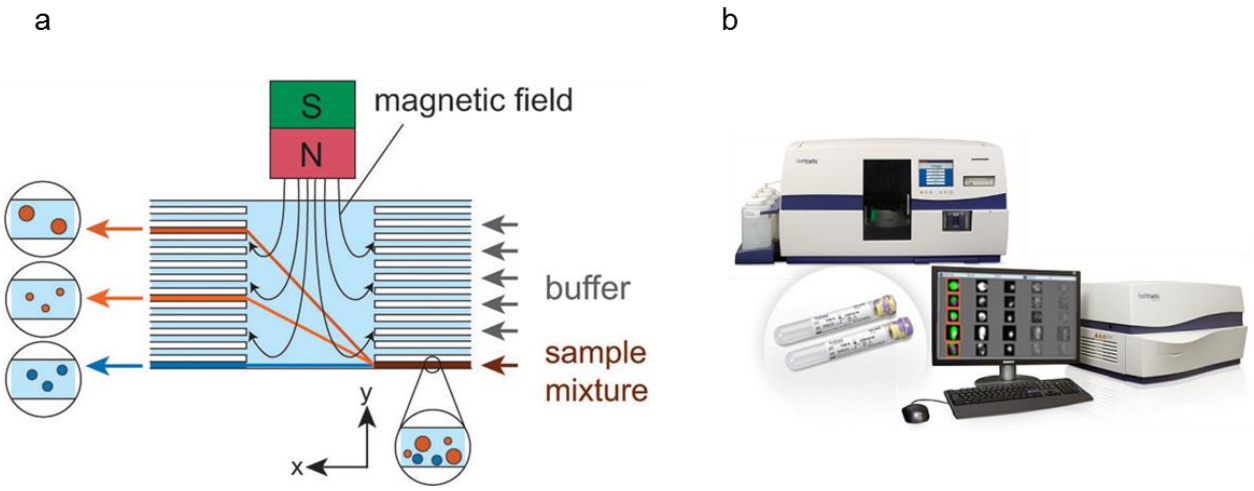

Figure 1.3. Commercially available magnetic-activated cell sorting systems a) Magnetic activated cell sorter (MACS). b) CellSearch: a commercially available and FDA-approved cell sorting system for capturing rare circulating tumor cells.

The arrival of FACS and MACS greatly broadened clinical and research capabilities by enabling cell sorting using many newly developed cell markers other than size and density. Although FACS and MACS are currently the most popular FDA-approved cell sorting systems routinely used in the hospital and research labs, other newly developed forms of "cell sorters" have gained traction in the last two decades.

The discovery of new biomarkers has fueled the effort to design and build new cell sorting platforms that can separation cells accordingly. Most existing biomarkers are derived from the relationship between biochemistry and cell biology. For instance, there is a group of biochemical markers (antibodies) which specifically bind to epithelial cell adhesion molecule EpCAM-positive cells that are routinely used for research[6]. In another example, a $CD34^+$ antibody is frequently used to capture cells that express $CD34^+$ receptors on cell surface, because the abnormal number of $CD34^+$ cells present in a human body is an indicator of several diseases[7,8]. In addition, biochemical markers are also regularly used for clinical cancer

diagnostics. Some of these biomarkers are highly specific so that they can identify a particular type of cancer in patients. For instance, biomarkers that specifically bind HER2-positive cells are used to identify a subset group of breast cancer patients. The HER2 test is required by the American Society of Clinical Oncology Guidelines[9] for all breast cancer patients. Consequently, many new cell sorting platforms that rely on cell surface receptors to enrich cells are being developed.

To supplement these antibody biomarkers, cell sorting based on biophysical properties have also emerged in recent years[10-12]. The breakthrough in biology that revealed links between cell mechanical properties and diseases such as cancer[13] and malaria[14] has motivated much effort in searching for new technologies that can exploit these variations for cell sorting. For example, the reduction of cell stiffness has been observed in many solid tumor cases. The hypothesis being explored is that the increased deformability helps tumor cells to escape and invade other parts of the body[13]. Although all of the findings that describe the relationships between cell mechanical properties and diseases are still under investigation and none of the cell sorters that based on using cell mechanical properties have been applied to clinical settings, further understanding of cell biology will validate these hypotheses in the near future. Likewise, the development of cell sorting based on cell biophysical variations may demonstrate huge benefits and expand our existing capabilities for utilizing biochemical cell sorting.

Originated from the semiconductor industry, micro-fabrication techniques enabled a broad range of manufacturing capabilities for making miniature systems which are frequently coined as the micro total analysis systems (μTAS). These devices typically have features that are smaller than 1 mm and can be fabricated based on techniques from traditional silicon processing. Some important benefits[15] of μTAS include ultrafast analysis[16], small sample volume

requirement[17], and high sensitivity[18]. One type of μTAS is lab-on-a-chip (LOC) devices which integrate several conventional bench-top analyses onto a single chip. LOC devices are cost-effective, and time-saving. In addition, they allow multiplex analyses and have the potential for point-of-care applications. Perhaps the most well-known LOC systems are microfluidic devices. Since year 2000, microfluidics has been widely researched for cell manipulation with over 28,000 publications dedicated to this application. Many new forms of "cell sorters" have been purposed and developed based on microfluidics. As examples, electrophoresis, dielectrophoresis, acoustophoresis, deterministic/obstacle induced flow, flow fractionation, hydrodynamic filtration, and inertia flow, have all been utilized to improve cell processing and analysis and have generated tremendous amounts of interest. Although most of these methods remain confined to research labs, some have demonstrated great potential to expand cell sorting capability in real-world applications such as isolation of rare circulating tumor cells[19,20], and gene analysis[21,22].

1.2 Motivation of the Research and Its Significance

The primary objective of this research is to utilize a new cell sorting method based on emerging microfluidic technology to sort cells that have different biophysical properties. As previously discussed, the observation of the changes in cell mechanical properties related to diseases have important implications for disease diagnostics. The mechanical state of single cells reveals important information regarding the overall health of the tissue, organ, and whole body of the individual from which they are taken[23]. As new and reliable biophysical markers have been developed, there is a vital need for high throughput methods to sort cells by these markers.

Abnormal cell mechanical stiffness can point to the development of various diseases. One critical aspect in innovating biomedical device is to improve sensitivity of the disease detection process (Figure 1.4). Diseases like cancers and infections have very weak signals for detection. For instance, cancer metastasis can be detected through isolating circulating tumor cells, but the number of diseased cells is less than 10 in 1 billion[24]. Traditionally, diseased cells have been identified through morphological differences with healthy cells, and fluorescent molecular markers are routinely used to separate specific subpopulations of cells. However, the morphological overlap between the diseased and healthy cells often poses a significant problem to accurate identification of cell populations. In addition to biomolecular markers, new biophysical markers which can be readily detected and used to rapidly sort cells are vital for improving separation of different cell subpopulations and accurately detecting specific disease conditions.

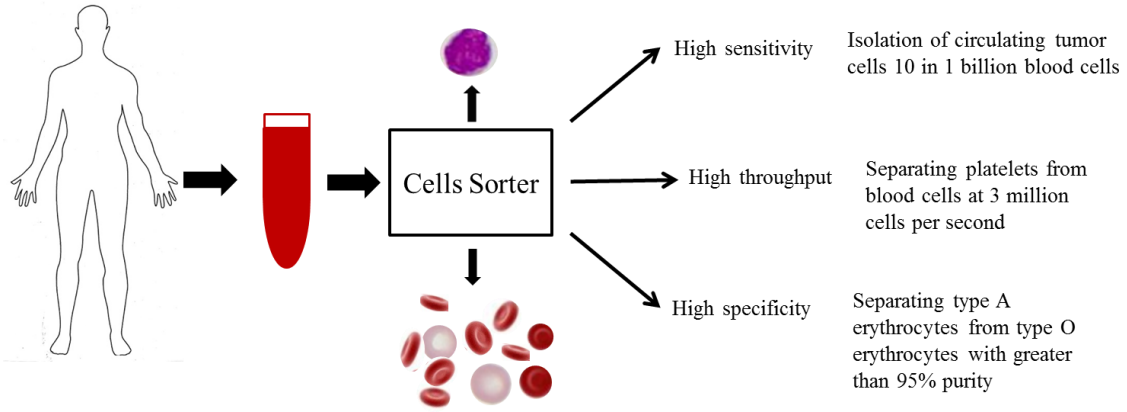

Figure 1.4. The advantages of cell-sorting platforms.

Methods that assay cell stiffness are not generally suitable for the high-throughput measurements required for enriching rare diseased cells amongst large numbers of normal cells—an essential step for a large number of biomedical assays. For example, stiffness

measurement tools such as atomic force microscopy (AFM) are not suitable for processing large numbers of cells required for enriching rare cancer cells amongst large numbers of noncancer cells. Although several microfluidic approaches have been described for the *measurement* of cell stiffness, there is a growing need for high-throughput sorting of mechanically distinct cells.

1.3 Thesis Overview

This thesis reports a newly developed microfluidic cell sorter which separates cells according to cell biophysical properties. In CHAPTER 2, the author describes the methods used to characterize cell biophysical properties and summarizes the recently discovered variations in cell biophysical properties as a result of various types of diseases. In CHPATER 3, the author reviews a group of new cell sorters and explains the principal mechanisms of cell sorting based on cell stiffness. In CHAPTER 4, the author describes the design and fabrication of the microfluidic cell-sorting platforms and elucidates the impact of design and operation parameters on cell sorting by stiffness. In CHAPTER 5, the author shows the results of cell sorting and demonstrates the capabilities of the cell sorter thorough cell separation by multiple cell biophysical properties. In CHAPTER 6, the author summarizes the research finding and concludes with limitations of the cell sorter and directions for its future development.

1.4 References

1. Coulter WH (1953) Means for counting particles suspended in a fluid. US Patent 2656508
2. Behar E, Chao NJ, Hiraki DD, Krishnaswamy S, Brown BW, et al. (1996) Polymorphism of adhesion molecule CD31 and its role in acute graft-versus-host disease. New England Journal of Medicine 334: 286-291.
3. Jamieson CHM, Ailles LE, Dylla SJ, Muijtjens M, Jones C, et al. (2004) Granulocyte-macrophage progenitors as candidate leukemic stem cells in blast-crisis CML. New England Journal of Medicine 351: 657-667.
4. Herzenberg LA, Parks D, Sahaf B, Perez O, Roederer M, et al. (2002) The history and future of the fluorescence activated cell sorter and flow cytometry: A view from Stanford. Clinical Chemistry 48: 1819-1827.
5. Mattanovich D, Borth N (2006) Applications of cell sorting in biotechnology. Microbial Cell Factories 5: 12.
6. Schulze K, Gasch C, Staufer K, Nashan B, Lohse AW, et al. (2013) Presence of EpCAM-positive circulating tumor cells as biomarker for systemic disease strongly correlates to survival in patients with hepatocellular carcinoma. International Journal of Cancer 133: 2165-2171.
7. Fadini GP, de Kreutzenberg S, Agostini C, Boscaro E, Tiengo A, et al. (2009) Low CD34+cell count and metabolic syndrome synergistically increase the risk of adverse outcomes. Atherosclerosis 207: 213-219.
8. Rotondo F, Sharma S, Scheithauer BW, Horvath E, Syro LV, et al. (2010) Endoglin and CD-34 immunoreactivity in the assessment of microvessel density in normal pituitary and adenoma subtypes. Neoplasma 57: 590-593.
9. Wolff AC, Hammond MEH, Hicks DG, Dowsett M, McShane LM, et al. (2013) Recommendations for Human Epidermal Growth Factor Receptor 2 Testing in Breast Cancer: American Society of Clinical Oncology/College of American Pathologists Clinical Practice Guideline Update. Journal of Clinical Oncology 31: 3997.
10. Wang GH, Mao WB, Byler R, Patel K, Henegar C, et al. (2013) Stiffness Dependent Separation of Cells in a Microfluidic Device. Plos One 8: 10
11. McFaul SM, Lin BK, Ma HS (2012) Cell separation based on size and deformability using microfluidic funnel ratchets. Lab on a Chip 12: 2369-2376.
12. Mohamed H, Murray M, Turner JN, Caggana M (2009) Isolation of tumor cells using size and deformation. Journal of Chromatography A 1216: 8289-8295.
13. Suresh S (2007) Biomechanics and biophysics of cancer cells. Acta Biomaterialia 3: 413-438.
14. Glenister FK, Coppel RL, Cowman AF, Mohandas N, Cooke BM (2002) Contribution of parasite proteins to altered mechanical properties of malaria-infected red blood cells. Blood 99: 1060-1063.
15. Khandurina J, Guttman A (2002) Bioanalysis in microfluidic devices. Journal of Chromatography A 943: 159-183.
16. Gregoratto I, McNeil CJ, Reeks MW (2007) Micro-devices for rapid continuous separation of suspensions for use in micro-total-analysis-systems (mu TAS). In: Paputsky I, Wang W, editors. Microfluidics, Biomems, and Medical Microsystems V. Bellingham: SPIE-Int Soc Optical Engineering.

17. Hosokawa K, Fujii T, Endo I (1999) Handling of picoliter liquid samples in a poly(dimethylsiloxane)-based microfluidic device. Analytical Chemistry 71: 4781-4785.
18. Kim YJ, Jones JE, Li H, Yampara-Iquise H, Zheng GL, et al. (2013) Three-dimensional (3-D) microfluidic-channel-based DNA biosensor for ultra-sensitive electrochemical detection. Journal of Electroanalytical Chemistry 702: 72-78.
19. Stott SL, Hsu CH, Tsukrov DI, Yu M, Miyamoto DT, et al. (2010) Isolation of circulating tumor cells using a microvortex-generating herringbone-chip. Proceedings of the National Academy of Sciences of the United States of America 107: 18392-18397.
20. Nagrath S, Sequist LV, Maheswaran S, Bell DW, Irimia D, et al. (2007) Isolation of rare circulating tumour cells in cancer patients by microchip technology. Nature 450: 1235-U1210.
21. Ottesen EA, Hong JW, Quake SR, Leadbetter JR (2006) Microfluidic digital PCR enables multigene analysis of individual environmental bacteria. Science 314: 1464-1467.
22. Zhong JF, Chen Y, Marcus JS, Scherer A, Quake SR, et al. (2008) A microfluidic processor for gene expression profiling of single human embryonic stem cells. Lab on a Chip 8: 68-74.
23. Dahl KN, Ribeiro AJS, Lammerding J (2008) Nuclear shape, mechanics, and mechanotransduction. Circulation Research 102: 1307-1318.
24. Yu M, Stott S, Toner M, Maheswaran S, Haber DA (2011) Circulating tumor cells: approaches to isolation and characterization. Journal of Cell Biology 192: 373-382.

CHAPTER 2

CELL BIOPHYSICAL PROPERTIES AS BIOMARKERS OF DISEASES

In section 2.1, we review methods that are used to characterize cell biophysical properties. For each method, we discuss the advantages and weaknesses and present examples of applications. In particular, we show in detail about using the atomic force microscopy (AFM) to measure cell properties and the reasons for us to select the AFM as the primary method for our experiment. In Sections 2.2 and 2.3, we explain the relationships between cell structures, cell function and cell biophysical properties using examples from the literature as well as experimental data. Then, we demonstrate through experiments to show how cell biophysical properties can be used as a new class of biomarkers to distinguish diseased and healthy cells.

2.1 Measuring Single Cell Mechanics

Eukaryotic cells have complex structures that in general consist of a bi-lipid membrane enclosing cytoplasm and a nucleus (Figure 2.1). The cell is made of both liquid and solid phases with roughly 70% liquid. Although the cell is far from homogenous material, viscoelastic models derived for engineering materials can characterize the cell mechanical properties fairly well[1,2].

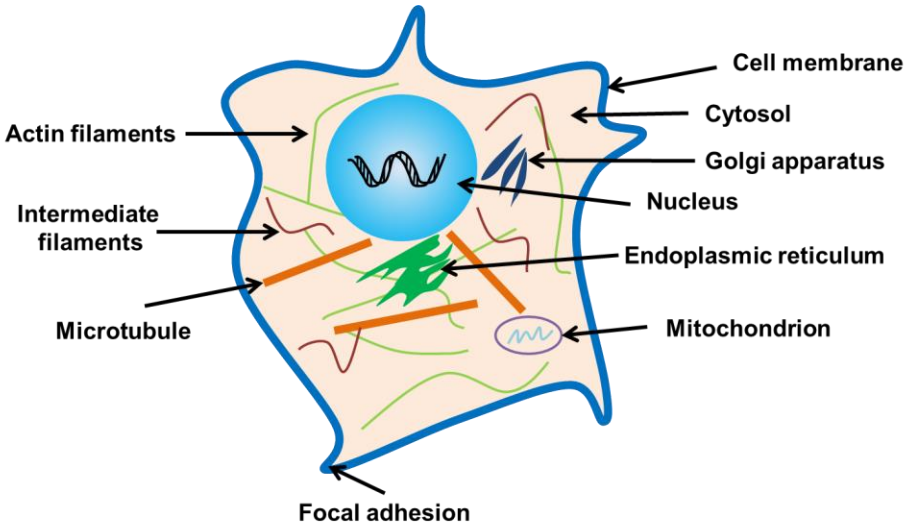

Figure 2.1. A depiction of a eukaryotic cell. The cell has a bi-lipid membrane enclosing organelles such as cytoskeleton, and nucleus.

Before separating cells using biophysical properties, we should understand the methods that can measure the differences in cell biophysical properties between cell populations. Cell biophysical properties require quantitative assessment by means of mechanical measurement. There are several key properties that can characterize the biophysical properties of eukaryotic cells, including cell size, cell stiffness, and cell viscosity[3]. These properties are a result of internal cellular structures that are linked to cell function and disease states.

Several tools have been developed to measure single cell mechanics. These tools apply a small force, typically ranging from pico- to nano-Newtons to cause some form of deformation of a single cell. Then, the measured deformation and applied force are recorded. The biophysical properties of the cells are derived from the relationship between the applied force and deformation. Some commonly employed single cell mechanics methods are micropipette aspiration[4,5] (Figure 2.2a), optical stretcher[6,7] (Figure 2.2b), magnetic tweezers[8,9] (Figure 2.2c), and atomic force microscopy[10-12] (Figure 2.2d).

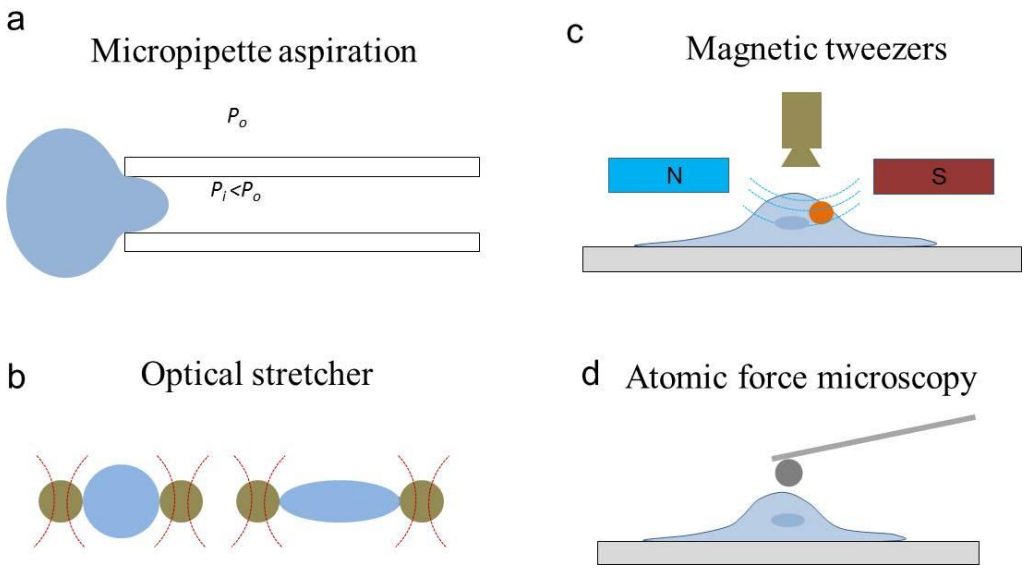

Figure 2.2. Cell mechanics measurement tools. a) Micropipette aspiration. Cells are siphoned into the pipette tip when the applied pressure is greater than the ambient pressure. b) Optical stretcher. Dual laser beams are used to deform cells in tension. c) Magnetic tweezers. Magnetic beads are phagocytized by the cells and an external magnetic field is applied to deform the cell by interacting with the bead. d) Atomic force microscope. A beaded AFM tip is used to probe cell mechanics.

Micropipette aspiration is a versatile tool that can measure cell elasticity and viscosity. The measurement aided the derivation of several constitutive models that describe the dynamic behavior of cells[13]. Micropipette has been used to measure both soft cells such as leukocytes[4] and red blood cells[14], and stiff cells such as chondrocytes[15] and endothelial cells[16]. A schematic of micropipette aspiration system is shown in Figure 2.2a where P_o is the ambient pressure and P_i is the applied pressure. A suspended cell is partially aspirated into the tip of the micropipette caused by a suction pressure applied at the other end of the micropipette. The micropipette tip is smaller than the cell's diameter which is on the order of 10 to 50 μm. The applied force is typically on the order of 10 – 100 pN[4]. The deformation is measured as the length of the extension of cell body inside the micropipette. Often, the length is normalized with

respect to the radius of the micropipette tip. The deformation of the cell is dependent on time and applied pressure. For example, higher pressure is needed to deform the same amount for a stiff cell than a softer cell. Since cells are viscoelastic, the deformation is time-dependent. For an elastic cell, the cell deforms further into the micropipette until a new equilibrium position is reached. For a viscous cell, the cell flow completely into the micropipette like liquid. The micropipette is an accurate yet simple tool to measure cell biophysical properties but it is not a perfect instrument. There are a few practical issues that limit the use of micropipette. For example, the applied suction pressure is limited by the vapor pressure of water at room temperature. In addition, the evaporation of in the liquid chamber causes a slow drift from the calibration setting.

Optical stretcher uses dual laser beams to deform single cells and is commonly used to study cell elastic and viscoelastic characteristics[17]. When a dielectric object such as a cell is positioned between two opposing but symmetric laser beams, the cell is stretched along the axis of the beams. The exerted force is generated by the momentum transfer from the light to the cell surface induced by the differences in refractive index of the cell surface and the medium. Figure 2.2b shows a cell before and during the optical stretching. The applied force typically ranges from 200 to 500 pN[6] and causes tensile stress on the whole cell. Optical stretcher was used to measure elasticity and viscosity of several different types of cells including the red blood cells[18] and breast epithelial cells[6]. The major benefit of using optical stretcher is that it is a contact-free method which eliminates contact-induced artefacts. However, optical stretcher has several limitations. For instance, the cells must be highly focused during optical visualization and the high intensity of laser light may generate local heating and damage to the cells[19]. In order to prevent damage, the deformation is normally small and in the range of 1% to 10%.

Magnetic tweezers use a controlled magnetic field to deform a single cell that has ferromagnetic beads either residing inside the cell or attached to the surface of the cell. Magnetic beads are internalized by cells through phagocytosis or adhered by conjugate binding of surface proteins. Figure 2.2c shows a schematic of the magnetic tweezers setup which consists of a pair of permanent magnets placed on top of a beaded cell sample. Two magnets produce an external magnetic field that generates a magnetic moment in the bead. The viscoelastic properties of a cell are measured by torsional deformation of a ferromagnetic bead in the cytoplasm or on the cell surface. The applied force ranges from 50 pN to 900 pN[8]. Magnetic tweezers system was used to measure macrophages[8], granulocytes[20], and fibroblast cells[21]. One of the most noticeable benefits of using magnetic tweezers system is that it provides viscoelastic measurement at the interior of the cells. Despite this unique functionality, the use the magnetic tweezers system is limited by several technical issues. For example, the cell sample preparation is not straightforward. Magnetic beads must be either phagocytized or attached on cell surface through functionalization. Furthermore, the torsion applied to cell is localized and on the magnetic bead instead of directly onto the cells.

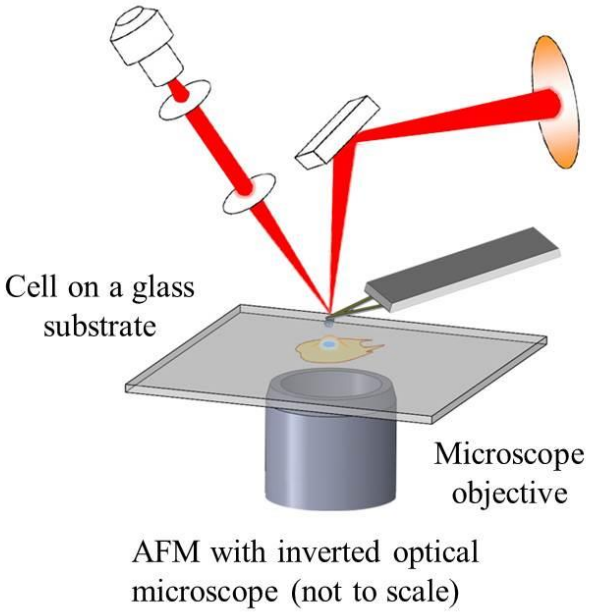

Figure 2.3. Typical AFM cell measurement setup. Cell rests on a glass substrate. A laser beam is used to measure the deflection of cantilever when it indents the cell. An inverted optical microscope is used to observe the indentation process.

The atomic force microscope (AFM) is extremely sensitive which makes it particularly well-suited for measuring biophysical properties of cells. The AFM consists of a cantilever probe, a system for measuring its deflection consisting of a laser diode, and a position-sensitive photodiode, and a method for holding a sample (Figure 2.3). As the cantilever is lowered to indent cell sample, the vertical bending of the cantilever is measured by the deflection of the laser beam which is recorded on a photodiode. The output of the AFM measurement is in terms of force versus indentation distance also known as a force-displacement curve (Figure 2.4a). For cell measurement, instead of a sharp tip, a silica bead is attached to the cantilever tip (Figure 2.4b and 2.5a). During the indentation, the beaded tip allows the AFM probe to measure multiple locations on a cell and avoid damage to the cells (Figure 2.5b).

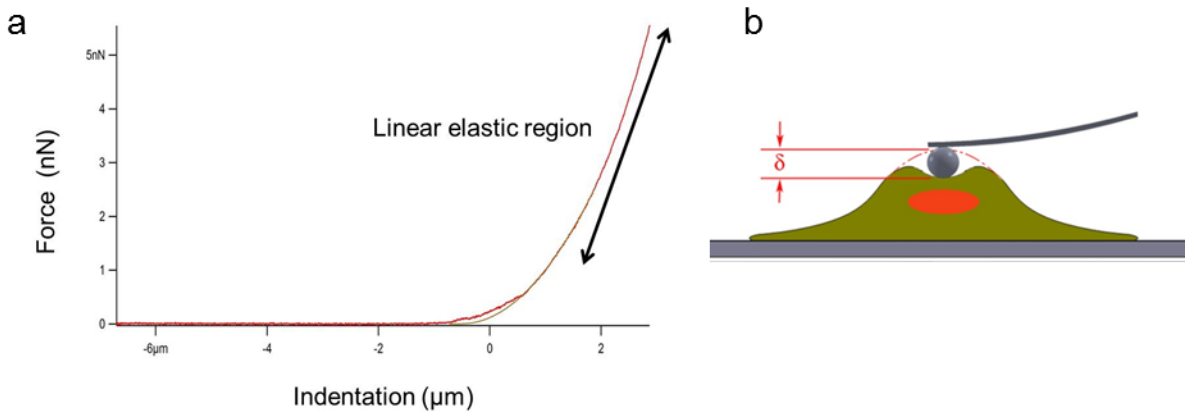

Figure 2.4. AFM force curve and cell deformation. a) Typical force-indentation curve for cells. The linear elastic region is used to compute Young's modulus. b) Indentation (δ) to the cell by the AFM cantilever tip.

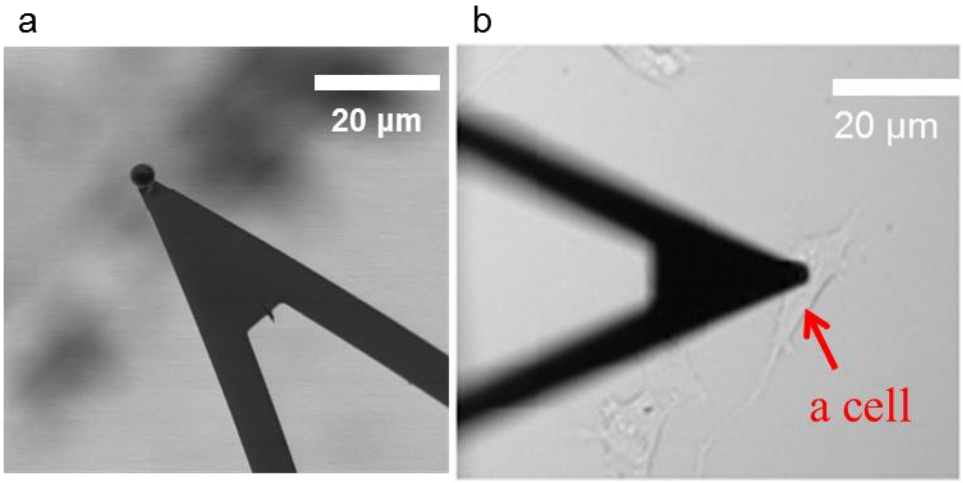

Figure 2.5. AFM measurement of a cell. a) A 4 μm silica bead is attached to the AFM probe tip and visualized by optical microscopy. b) The beaded tip is then used to compress and measure HeyA8 cells, an ovarian cancer cell line, as seen in this bright field microscopy image.

AFM has resolution at sub-nanometer and has the ability to measure cells under near-physiological conditions. Due to these unique advantages, many different cell types have been measured using AFM including blood cells[22], epithelial cells[23], endothelial cells[24], muscle cells[25] and others[26]. However, the prominent limitation of using AFM is the throughput

which is about 20 cells per hour for experienced users. Other limitations of AFM include the nonspecific interactions between the cell and the tip, the effect of the substrate on the cells, and the sources of noise such as thermal vibrations.

In this research project, atomic force microscopy is used for measuring cell biophysical properties including cell elasticity and cell relaxation. There are several reasons for choosing AFM in our studies over other methods. First, AFM is extremely sensitive and can provide accurate measurements and consistent results. Second, the AFM indentation of the cells results in compressive strains that are similar in magnitude and direction (compression) to those experienced during microfluidic compression. The AFM can consistently apply strains over 40% to the cells, which helps in exploring mechanical properties for a range of microfluidic designs that impose large cellular strains.

For cell stiffness measurement, the force-indentation curves are analyzed using Hertzian contact mechanics models (Figure 2.6a) which require the material properties of the cantilever and the loading parameters. The Young's modulus can be obtained by fitting the force-displacement curves to the Hertzian models. For example, to estimate the average Young's modulus as a function of indentation, we apply point-wise Hertzian model where the Young's modulus is determined at corresponding indentation (Figure 2.6b). For viscoelastic measurement, a constant force is applied at the tip and the displacement of the cantilever is recorded. The dynamic response of the cell is captured through force-displacement curves and the corresponding time intervals. After, taking measurement, the cantilever is disengaged and an image of the cell is taken to record cell size.

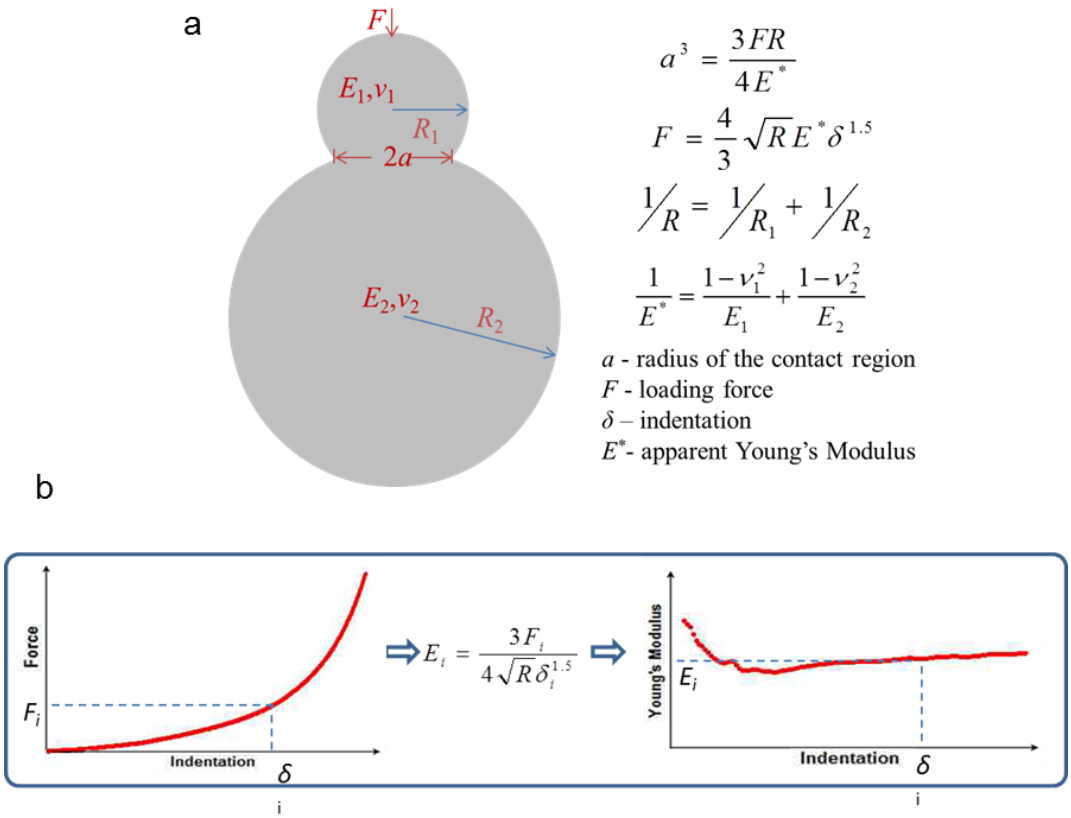

Figure 2.6. Hertzian model for calculating cell Young's modulus. a) Hertzian contact mechanics model for two spheres in contact. b) The elastic region of the force-indentation curve is fitted using point-wise Hertzian model to derive the Young's modulus of the sample such as a cell.

To make the AFM results more relevant and comparable to microfluidic cell sorting, the measured cells are suspended in the medium instead of adhering to the substrate. To avoid cell slipping away during indentation, we applied a monolayer of poly-l-lysine (MW 300k, Sigma Aldrich) to serve as anchors to slightly attach cells to the glass substrate to improve cell stability during AFM measurement. The rounded morphology and suspended state resemble the conditions when cells are streamed through the microfluidic channels. In addition, large indentation is required to apply 30% to 40% strain to cells, since the microfluidic channel would apply similar compressive strain.

Cell stiffness and relaxation time data were measured using an atomic force microscope (MFP-3D, Asylum Research). All cells were measured in suspension so that cell morphology closely resembled to that in the microfluidic channel. The cell stiffness was represented by the average Young's modulus. Beaded silicon nitride cantilevers (spring constant 37.1 pN per nm) were used to indent the center of cells at 1.5 μm per second. The applied force was able to achieve at least 4 μm deformations such that it was in close comparison with our microfluidic compression. We took at least three force-indentation curves for each cell and fitted the curves to a Hertzian model to compute the average Young's modulus (Figure 2.6b). The cell viscosity was measured by the relaxation rate constant. The viscoelastic response can be modelled using the standard linear solid model where one spring is connected to a spring-and-damper in parallel. The relaxation rate constant is the inverse of the time it takes for a cell to relax 60% of its original uncompressed state. Similar to elastic measurement, we indented the cells with a beaded tip but "dwell" the tip by holding the cantilever at fixed position relative to the substrate for 10 seconds so that as the cell relaxes the cantilever deflection can be measured. Cell relaxation was fitted with exponential functions and the relaxation rate constants were calculated.

2.2 Biophysical Property Changes in Diseased Cells

Cell biophysical property changes have been identified in diseases that include solid tumor cancers[27], malaria[28], and sickle cell anemia[29,30]. For instance, the reduction in cell stiffness has been observed both in cancer cell lines[22,23] and samples from patient who are diagnosed with lung, breast and pancreatic cancers[27,31]. The change in cell stiffness is primarily due to the transformation of cell's cytoskeleton as well as the nuclear structure. One

hypothesis for cancer cells to become softer is that the increased flexibility can help cancer cells to invade to other parts of the body[32].

Cancer is a disease that is characterized by the uncontrolled proliferation of cells. Healthy cells are programmed to undergo apoptosis at the end of their lifecycle through activation of caspases. In order to achieve immortality, cancer cells either inhibit or disrupt apoptotic proteins. During this process, cell's internal structure is also transformed. In particular, the cytoskeleton networks which constitute the rigidity and shape of cells are altered. The alteration of the cytoskeleton modifies the motility, migration, and mechanics during deformation. The links between cell structure, property and disease states are introduced through the following examples.

The deformability of normal breast epithelial cell and cancer counterpart was investigated using optical stretcher by Guck *et al* [6]. MCF-10 and MCF-7 cell lines were selected to represent normal and cancer cells and a chemically modified version of MCF-7 with increased metastatic potential is used to represent highly invasive cancer cells. Cells were suspended in a fluid-filled chamber and individually stretched using a dual laser beam system. The results indicate that cell deformability has strong dependence on cell's metastatic potential (Figure 2.7). The reduction in cell elastic rigidity is mainly due to the reduction of F-actin concentration during the malignant transformation. Similar results on the same cell lines using AFM measurements were also reported[23]. In addition, patient biopsy samples also showed that cancer tissues are softer than healthy tissues[33].

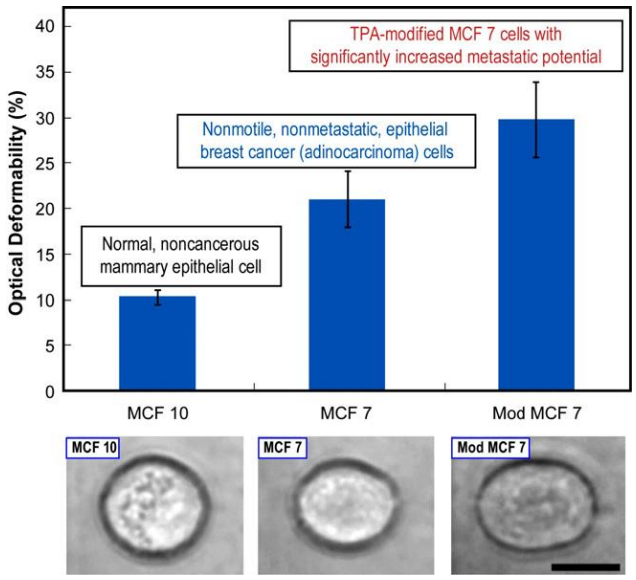

Figure 2.7. Cell deformability increases with increasing metastatic potential. Picture taken from [27].

Ovarian c**a**ncer is one of the most lethal forms of tumor because of the lack of early detection methods and its high metastatic potential to spread. The elastic property of normal and cancer ovarian cell lines were characterized using atomic force microscopy (Figure 2.8). Cells were probed by a beaded cantilever tip which exerted 100 pN to 20 nN force. The applied compressive indentation ranged from 0.5 to 2 µm. Five cell lines were examined by AFM. IOSE is the healthy ovarian epithelial cell. HEY and OVCAR-4 are cancerous ovarian epithelial cells and HEY A8 and OVCAR-3 are the more aggressive cancer forms respectively. Similar to breast cancer, negative correlations between cell rigidity and metastatic potential were found (Figure 2.8a and 2.8b). In particular, cell mobility and the tendency for spreading are correlated with cell elasticity (Figure 2.8b). This shows another example that cancer transformation modifies cell structure which alters cell's functions.

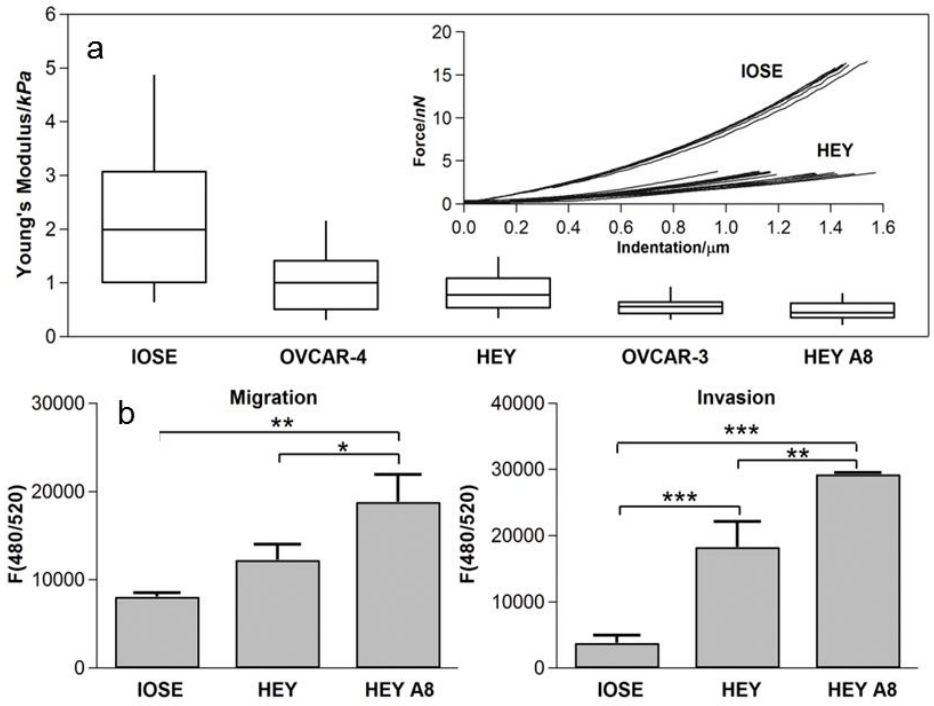

Figure 2.8. Ovarian cell mechanics. a) AFM studies of five ovarian cell lines[34]. The whisker-box plots show the average Young's modulus for healthy ovarian cell line IOSE and cancer ovarian cell lines HEY, HEY A8, OVCAR-4 and OVCAR-3. The box includes 50% of population the whisker include 90% of population and the mean is represented by the bar near the center of the box. b) Cell migration and mobility study reveal cell elasticity is correlated with metastatic potential.

To reveal the changes of internal structure of cells, actin filament structure of healthy and cancer ovarian cell is imaged and compared. The act filaments were labelled with fluorescent staining which showed the declining and disorganization of actin filament with increasing metastatic potential (Figure 2.9). On the other hand, the normal cells had thicker and more directional actin bundles. The morphology of normal and cancer cells are also quite different. When examining cells cultured on a plate, cancer cells have pebble-like shapes due to the random alignment of the actin filament. In contrast, the normal cells are more elongated with clear actin fibers.

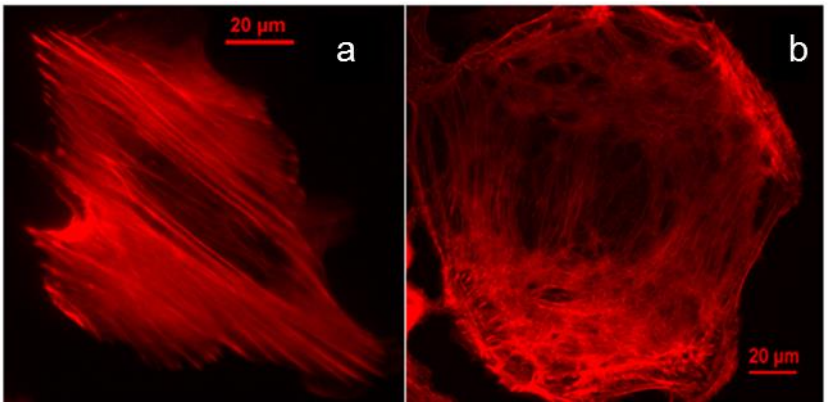

Figure 2.9. Images of actin filaments of healthy and cancer ovarian cells. Fluorescent stain shows a) a healthy ovarian cell (IOSE) has denser and more directional actin filament bundles than b) a cancerous ovarian cell (HEY A8)[34].

The links between cell structure, mechanical properties and disease states have suggested that cell biophysical properties are biomarkers of diseases. Thus far, evidence has shown that reorganization and alteration of cell cytoskeleton is for the most part responsible for changes in cell mechanical properties[35]. Therefore, in the following chapters, it is safe to assume the changes of cytoskeleton will have major impact on cell biophysical properties.

2.3 Biophysical Property Changes in Blood Cells

Since our goal is to demonstrate the microfluidic cell separation using a variety of blood cells, we present a full biophysical characterization of these cells in this section. The changes in cell biophysical properties were observed in leukemia[36-38], which is a type of blood cancer that is characterized by the uncontrolled proliferation of malignant blood cells. It is one of the deadliest blood disorders that causes an estimate of more than 50,000 cases and 50% fatality rate

in 2014 according to the National Cancer Institute. Cell sorting technology can improve leukemia patient outcomes in mainly two ways: early detection and classification of leukemia types. For instance, the detection of pre-leukemic stem cells can potentially stop the onset or relapse of acute myeloid leukemia by allowing early intervention[39]. However the challenge of early detection lies in that the general symptoms such as fatigue and fever are overlapping with other common diseases which make it hard to detect. Therefore, accurate early detection is the key to effectively cure leukemia patients. Furthermore, leukemia is subdivided into acute and chronic which are further divided into lymphoid and myeloid. The treatment for each type of leukemia is different and patient specific. As a result, being able to quickly and accurately identify leukemia types can be tremendously valuable for implementing treatment plans.

To separate leukemia cells, we selected four types of blood cells as our cell models: HL60, Jurkat, K562 and healthy leukocytes. K562 cells (CCL-243), Jurkat cells (CRL-1990) and HL60 cells (CCL-240) were purchased from ATCC. K562 and HL60 cells were cultured and maintained in Iscove's modified Dulbecco's medium (ATCC) with the addition of 10% fetal bovine serum (FBS). Jurkat cells were cultured and maintained in RPMI-1640 medium (Sigma) with the addition of 10% FBS. Cells were stored at 37 degree Celsius with 5% CO_2. Cells were expanded to 0.5×10^6 cells per mL in a culture flask over two days. Whole blood was withdrawn from healthy donors using Georgia Tech IRB approved protocol (H12002). White blood cells were separated from fresh whole blood using Ficoll-Paque (1.077, GE Life Sciences) through centrifugation. The remaining red blood cells were lysed using human red blood cell lysing buffer (Alfa Aesar). The isolated white blood cells were from 1 to 2 million cells per mL of whole blood and were resuspended in DPBS.

To illustrate that cell biophysical properties can be used as biomarkers to distinguish different blood cell types, we characterized these four cell types in terms of cell diameter, cell stiffness and cell relaxation rate constant. Figure 2.10 shows the biophysical properties of three different types of leukemia cells and healthy leukocytes. The cell diameters do not vary as much as cell stiffness and cell relaxation (Table 2.1). The cell diameters for HL60 is 12.4 ± 1.2 μm, for Jurkat is 15.0 ± 2.0 μm, for K562 is 14.4 ± 1.1 μm and for leukocyte is 11.5 ± 2.1 μm (Figure 2.10a). Cell elasticity which is measured by cell Young's modulus, *E*, is significantly different for different blood cells. The Young's modulus for HL60 is 0.86 ± 0.22 kPa, for Jurkat is 0.24 ± 0.089 kPa, for K562 is 0.4 ± 0.22 kPa and for leukocyte is 0.81 ± 0.624 kPa (Figure 2.10b). HL60 has the highest stiffness and Jurkat is the softest cell type. The leukocyte has the largest error bar (standard deviation) because the population includes several different cell types such as monocyte, lymphocyte and neutrophils. Figure 2.10c shows cell viscosity which is measured by cell relaxation rate constant also varies significantly different cell types. The cell relaxation time constant for HL60 is 8.9 ± 4.55 s^{-1}, for K562 is 17.7 ± 13.8 s^{-1}, for leukocyte is 5.47 ± 5.12 s^{-1} and for formaldehyde treated K562 (K562F) is 47.5 ± 27.9 s^{-1}. HL60 are highly viscous cells. Previous micropipette experiments showed the HL60 flows like liquid into the micropipette when the suction pressure is greater than a threshold pressure[40]. To verify our AFM technique, we tested an extreme scenario where 4% formaldehyde was added to K562 cells. After the crosslinking treatment, the cells exhibited highly elastic behavior with three fold increase in the relaxation rate constant.

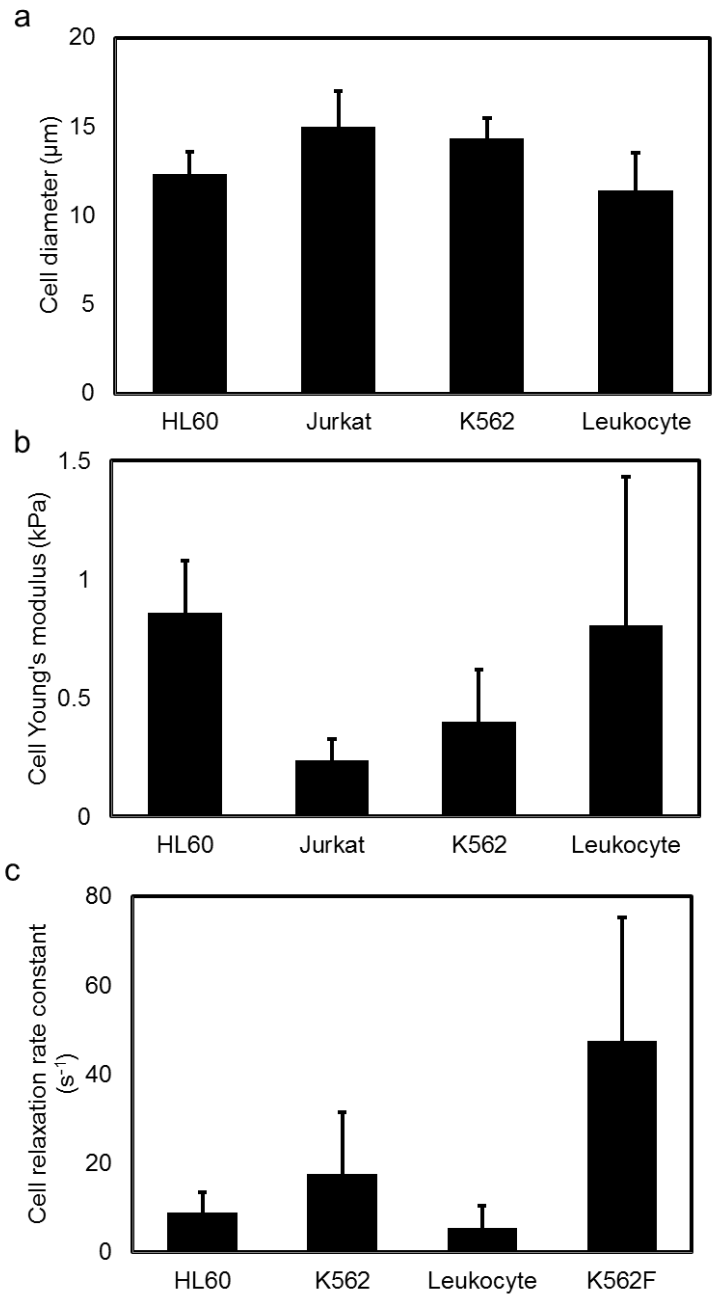

Figure 2.10. Cell biophysical properties. a) Cell diameter for HL60, Jukat, K562 and leukocytes from periphery blood. Error bars are standard deviations. Sample size $n \geq 25$. b) Cell elasticity in terms of cell's Young's modulus. Sample size $n \geq 25$. c) Cell viscosity in terms of cell relaxation time constant. Sample size $n \geq 25$. Error bars are standard deviations.

Table 2.1. Percentage difference among different cell biophysical properties.

Percentage Change	
Biophysical Properties	$\frac{(\text{Max} - \text{Min})}{\text{Max}}$
Size	23.3%
Young's modulus	72.1%
Relaxation	69.1%

Red blood cells (RBCs) are quite different from white blood cells in that RBCs do not have a nucleus and their shape is biconcave instead of spherical. The mechanics of RBCs are also affected by diseases[41] such as malaria. Malaria is an infectious disease that kills half million people each year. 90% of the deaths were in Africa. The high fatality rate is primarily due to the poor sanitation and lack of medical equipment for detection. Thus, an inexpensive yet accurate early detection point-of-care technology such as microfluidics is a suitable solution. Unlike solid tumor cancer cells, the parasite infected red blood cells show increased stiffness[42] and altered shape[43]. The proteins secreted by the parasite stiffen the cell membrane by crosslinking the spectrin network. In addition, the presence of the non-deformable parasite also contributes to the increased stiffness. The loss of flexibility has major adverse consequences. Normal RBCs are highly deformable and squeeze through capillaries that are less than a few microns[41]. However, the stiffening of the parasite-infected RBC can cause obstruction of vasculature and, therefore, failure of oxygen delivery.

In addition to white blood cells, we also characterized red blood cells and chemically modified red blood cells to simulate mechanical variations of diseased cells, resulting in red

blood cell subpopulations that have different elasticity. Three chemical agents were tested: diamide at 38 μM, 4% v/v formaldehyde, and 4% v/v glutaraldehyde. The added chemical agents created red blood cell populations with gradual increasing Young's modulus. The Young's modulus for normal RBCs is 101.7 ± 42.8 Pa, for diamide treated RBCs is 1.87 ± 0.73 kPa, for formaldehyde treated RBCs is 4.27 ±1.61 kPa, and for glutaraldehyde is 18.51 ± 7.76 kPa (Figure 2.11). The difference in stiffness is caused by different degree of cellular structure crosslinking. Diamide affects the cell stiffness by crosslinking spectrin skeletal membrane proteins. Unlike diamide, formaldehyde and glutaraldehyde, which are commonly used as cell fixing agents, crosslink not only the membrane but also cytoskeletons. Therefore, the formaldehyde and glutaraldehyde treated RBCs have higher Young's modulus than diamide treated RBCs.

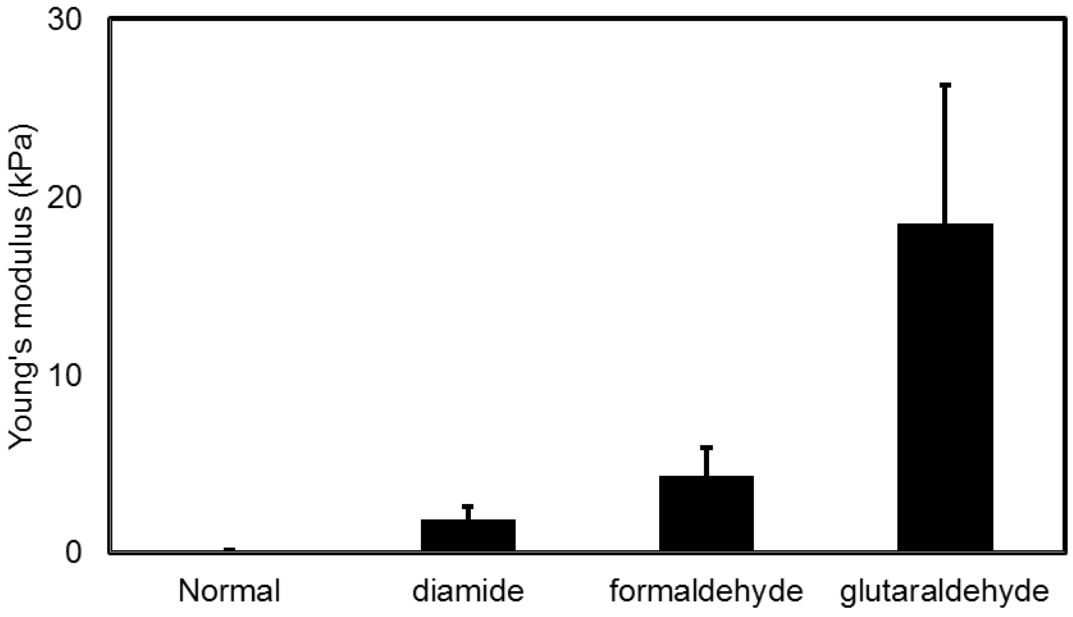

Figure 2.11. Red blood cells and chemically treated red blood cells show differences in cell stiffness. Sample size $n \geq 20$.

To summarize, we characterized four types of white blood cells using their size, stiffness and relaxation and we found biophysical properties can be used as biomarkers to distinguish different cell types. In addition, we can chemically modified cell biophysical properties to create models for our cell separation experiment later.

2.4 References

1. Guilak F, Tedrow JR, Burgkart R (2000) Viscoelastic properties of the cell nucleus. Biochemical and Biophysical Research Communications 269: 781-786.
2. Kasza KE, Rowat AC, Liu JY, Angelini TE, Brangwynne CP, et al. (2007) The cell as a material. Current Opinion in Cell Biology 19: 101-107.
3. Moreno-Flores S, Benitez R, Vivanco MD, Toca-Herrera JL (2010) Stress relaxation and creep on living cells with the atomic force microscope: a means to calculate elastic moduli and viscosities of cell components. Nanotechnology 21: 445101.
4. Hochmuth RM (2000) Micropipette aspiration of living cells. Journal of Biomechanics 33: 15-22.
5. Schmidschonbein GW, Sung KLP, Tozeren H, Skalak R, Chien S (1981) Passive mechanical-properties of human-leukocytes. Biophysical Journal 36: 243-256.
6. Guck J, Schinkinger S, Lincoln B, Wottawah F, Ebert S, et al. (2005) Optical deformability as an inherent cell marker for testing malignant transformation and metastatic competence. Biophysical Journal 88: 3689-3698.
7. Lautenschlaeger F, Paschke S, Schinkinger S, Bruel A, Beil M, et al. (2009) The regulatory role of cell mechanics for migration of differentiating myeloid cells. Proceedings of the National Academy of Sciences of the United States of America 106: 15696-15701.
8. Bausch AR, Moller W, Sackmann E (1999) Measurement of local viscoelasticity and forces in living cells by magnetic tweezers. Biophysical Journal 76: 573-579.
9. Gosse C, Croquette V (2002) Magnetic tweezers: Micromanipulation and force measurement at the molecular level. Biophysical Journal 82: 3314-3329.
10. Radmacher M (2002) Measuring the elastic properties of living cells by the atomic force microscope. Atomic Force Microscopy in Cell Biology 68: 67-90.
11. Costa KD (2003) Single-cell elastography: Probing for disease with the atomic force microscope. Disease Markers 19: 139-154.
12. Darling EM, Zauscher S, Guilak F (2006) Viscoelastic properties of zonal articular chondrocytes measured by atomic force microscopy. Osteoarthritis and Cartilage 14: 571-579.
13. Evans E, Yeung A (1989) Apparent viscosity and cortical tension of blood granulocytes determined by micropipet aspiration. . Biophysical Journal 56: 151-160.
14. Glenister FK, Coppel RL, Cowman AF, Mohandas N, Cooke BM (2002) Contribution of parasite proteins to altered mechanical properties of malaria-infected red blood cells. Blood 99: 1060-1063.
15. Jones WR, Ting-Beall HP, Lee GM, Kelley SS, Hochmuth RM, et al. (1999) Alterations in the Young's modulus and volumetric properties of chondrocytes isolated from normal and osteoarthritic human cartilage. Journal of Biomechanics 32: 119-127.
16. Sato M, Theret DP, Wheeler LT, Ohshima N, Nerem RM (1990) Application of the micropipette technique to the measurement of cultured porcine aortic endothelial-cell viscoelastic properties. . Journal of Biomechanical Engineering-Transactions of the Asme 112: 263-268.
17. Sawetzki T, Eggleton CD, Desai SA, Marr DWM (2013) Viscoelasticity as a Biomarker for High-Throughput Flow Cytometry. Biophysical Journal 105: 2281-2288.
18. Guck J, Ananthakrishnan R, Mahmood H, Moon TJ, Cunningham CC, et al. (2001) The optical stretcher: A novel laser tool to micromanipulate cells. Biophysical Journal 81: 767-784.

19. Neuman KC, Nagy A (2008) Single-molecule force spectroscopy: optical tweezers, magnetic tweezers and atomic force microscopy. Nature Methods 5: 491-505.
20. de Vries AHB, Krenn BE, van Driel R, Kanger JS (2005) Micro magnetic tweezers for nanomanipulation inside live cells. Biophysical Journal 88: 2137-2144.
21. Winkleman A, Gudiksen KL, Ryan D, Whitesides GM, Greenfield D, et al. (2004) A magnetic trap for living cells suspended in a paramagnetic buffer. Applied Physics Letters 85: 2411-2413.
22. Rosenbluth MJ, Lam WA, Fletcher DA (2006) Force microscopy of nonadherent cells: A comparison of leukemia cell deformability. Biophysical Journal 90: 2994-3003.
23. Li QS, Lee GYH, Ong CN, Lim CT (2008) AFM indentation study of breast cancer cells. Biochemical and Biophysical Research Communications 374: 609-613.
24. Mathur AB, Collinsworth AM, Reichert WM, Kraus WE, Truskey GA (2001) Endothelial, cardiac muscle and skeletal muscle exhibit different viscous and elastic properties as determined by atomic force microscopy. Journal of Biomechanics 34: 1545-1553.
25. Liu JW, Sun N, Bruce MA, Wu JC, Butte MJ (2012) Atomic Force Mechanobiology of Pluripotent Stem Cell-Derived Cardiomyocytes. Plos One 7: 5.
26. Kuznetsova TG, Starodubtseva MN, Yegorenkov NI, Chizhik SA, Zhdanov RI (2007) Atomic force microscopy probing of cell elasticity. Micron 38: 824-833.
27. Suresh S (2007) Biomechanics and biophysics of cancer cells. Acta Biomaterialia 3: 413-438.
28. Fedosov DA, Lei H, Caswell B, Suresh S, Karniadakis GE (2011) Multiscale Modeling of Red Blood Cell Mechanics and Blood Flow in Malaria. Plos Computational Biology 7: 12.
29. Evans E, Mohandas N, Leung A (1984) Static and dynamic rigidities of normal and sickle erythrocytes - major influence of cell hemoglobin concentration. . Journal of Clinical Investigation 73: 477-488.
30. Nash GB, Johnson CS, Meiselman HJ (1984) Mechanical-properties of oxygenated red-blood cells insickle-cell (HBSS) disease. . Blood 63: 73-82.
31. Cross SE, Jin YS, Rao J, Gimzewski JK (2007) Nanomechanical analysis of cells from cancer patients. Nature Nanotechnology 2: 780-783.
32. Kumar S, Weaver V (2009) Mechanics, malignancy, and metastasis: The force journey of a tumor cell. Cancer and Metastasis Reviews 28: 113-127.
33. Plodinec M, Loparic M, Monnier CA, Obermann EC, Zanetti-Dallenbach R, et al. (2012) The nanomechanical signature of breast cancer. Nature Nanotechnology 7: 757-765.
34. Xu WW, Mezencev R, Kim B, Wang LJ, McDonald J, et al. (2012) Cell Stiffness Is a Biomarker of the Metastatic Potential of Ovarian Cancer Cells. Plos One 7: 10.
35. Gardel ML, Shin JH, MacKintosh FC, Mahadevan L, Matsudaira P, et al. (2004) Elastic Behavior of cross-linked and bundled actin networks. Science 304: 1301-1305.
36. Lam WA, Rosenbluth MJ, Fletcher DA (2008) Increased leukaemia cell stiffness is associated with symptoms of leucostasis in paediatric acute lymphoblastic leukaemia. British Journal of Haematology 142: 497-501.
37. Skorkina MY, Fedorova MZ, Muravyov AV, Sladkova EA (2012) The Use of Nanomechanic Sensor for Studies of Morphofunctional Properties of Lymphocytes from Healthy Donors and Patients with Chronic Lymphoblastic Leukemia. Bulletin of Experimental Biology and Medicine 154: 163-166.

38. Zhou ZL, Hui TH, Tang B, Ngan AHW (2014) Accurate measurement of stiffness of leukemia cells and leukocytes using an optical trap by a rate-jump method. Rsc Advances 4: 8453-8460.
39. Shlush LI, Zandi S, Mitchell A, Chen WC, Brandwein JM, et al. (2014) Identification of pre-leukaemic haematopoietic stem cells in acute leukaemia. Nature 506: 328-+.
40. Tsai MA, Waugh RE, Keng PC (1996) Cell cycle-dependence of HL-60 cell deformability. Biophysical Journal 70: 2023-2029.
41. Diez-Silva M, Dao M, Han JY, Lim CT, Suresh S (2010) Shape and Biomechanical Characteristics of Human Red Blood Cells in Health and Disease. Mrs Bulletin 35: 382-388.
42. Dondorp AM, Kager PA, Vreeken J, White NJ (2000) Abnormal blood flow and red blood cell deformability in severe malaria. Parasitology Today 16: 228-232.
43. Suresh S (2006) Mechanical response of human red blood cells in health and disease: Some structure-property-function relationships. Journal of Materials Research 21: 1871-1877.

CHAPTER 3

CELL SEPARATION MECHANISMS

In section 3.1, we review the current microfluidic cell sorting methods. For each method, we describe the cell separation mechanism and discuss the advantages and weaknesses. In section 3.2, we introduce the concept of cell separation based on stiffness and explain our cell sorting mechanisms. We reveal the correlations between cell biophysical properties and cell trajectory. In section 3.3, we illustrate an example which shows cell trajectory is a function of cell stiffness.

3.1 A Review of Existing Microfluidic Cell Separation Methods

Microfluidic cell sorters can be roughly classified into two groups: active sorting and passive sorting. Active sorting mechanisms employ external fields for actuation which controls the cell trajectory and sorting process in addition to a flow field that carries the cells. A variety of different physical mechanisms have been used to separate cells, including magnetic fields[1,2], electric fields[3,4], optical forces[5,6], and acoustic fields[7,8]. Active sorting methods generally offer higher specificity and sensitivity. The externally applied fields interact with cell labelling agents, which tag cells through biochemical reactions to actively "seek out and capture" target cells. This not only allows active methods to specifically select only the target cells (specificity) but also enable them to capture rare cells when the signal-to-noise ratio of the cell sample is high (sensitivity). However, the applied external field adds to the complexity of cell sorting process and increases the cost. For example, labeling of cells through specific binding of fluorescent

antibodies such as FACS[9] and MACS is expensive, requires highly-trained personnel, and hampers the downstream analysis of separated cells. Additionally, the separation executed by these techniques occurs only after individual readout of the labeling differentiation which limits the throughput. In the follow paragraphs, we will review the some of the active cell sorting methods and discuss their advantages and weaknesses.

Cells can be sorted by immunomagnetic tagging and applying an external magnetic field to extract target cells from cell mixture (Figure 3.1). Cells are labelled by magnetic beads that are either coated with antibodies which specifically bind to cell surface proteins[10] or introduced into the cells through phagocytosis and bind specifically to organelles[2]. The externally applied magnetic field can be generated either by permanent magnets[2] or by electromagnets[11]. Cells flow through a microchannel which provides the cell focusing. The laminar flow carries the non-labelled cells to designated outlet while the magnetic gradient over the microchannel pushes the labelled cells to migrate laterally across the flow axis and to be collected at a different outlet. The cell sorting depends on the strength of the magnetic field gradient, the size of the cells, the applied flow rate, and the density of the magnetic particles tagged to the cells. The major advantage of magnetic cell sorting is that it offers high specificity and sensitivity. High purity of target cells can be collected at the outlet because of the use of biochemical cell labeling markers. In addition, magnetic cell sorting is particularly useful isolating rare cells. For example, circulating tumor cells are mixed with blood cells at about 1 in 10^9 [12], which makes it technically challenging for other cell sorting methods. However, magnetic cell sorting has some limitations. The cell labelling process is time-consuming and expensive. The uptake and adherence of the magnetic particles to the cells is sensitive to incubation condition and other

factors such as cell culture condition. The target cells may also be lost due to inefficient labelling.

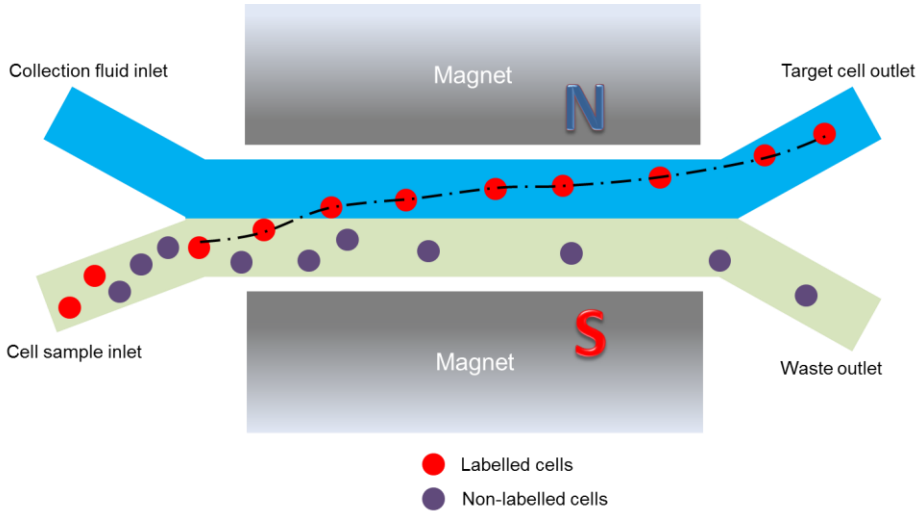

Figure 3.1. Microfluidic continuous magnetic cell sorting[2].

Cells can also be sorted using electric fields in a process called dielectrophoresis (DEP)[13,14]. Unlike electrophoresis where the movement of the sample depends on the intrinsic electrical charge carried by the sample itself, dielectrophoresis causes the charge-neutral sample to move by the magnitude and polarity of the charges which are induced by the applied ac electric field. When a non-uniform ac electric field is applied to the cells, the force generated on each side of the cell is different depending on cell dielectric property and the ac frequency. Cells can either move toward the electrodes (positive DEP) or away from electrodes (negative DEP) depending on the relative polarity of the cell with respect to the carrying medium (Figure 3.2). Generally, a negative DEP is preferred because cells remain in the "low" electric field region to avoid damage[15]. Similar to magnetic cell sorting, cell mixtures are carried in laminar flows into a microfluidic channel. The target cells migrate away toward designate outlet and are

collected continuously[16]. Alternatively instead of relying on cell's intrinsic dielectrophoretic response, polymeric beads can be used to label target cells through immuno-binding[4]. The specific biomarker binding improves cell sorting specificity and sensitivity. The cell migration trajectory depends on the frequency of the ac electric field, the cell dielectric property and the flow rate.

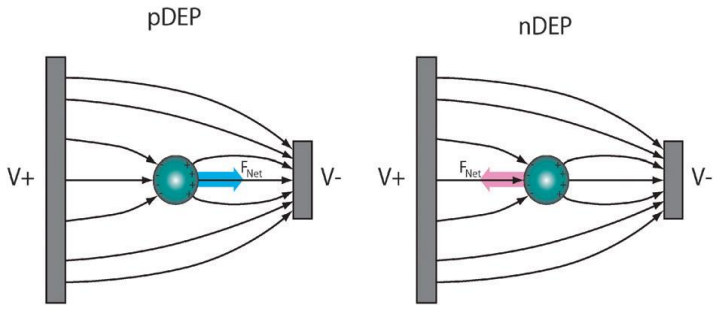

Figure 3.2. Dielectrophoresis. A dipole of cell is induced by the applied ac electric field. The movement of cell (pDEP vs. nDEP) depends on the relative polarity of the cell and carrying medium. Picture is taken from[17].

Dielectrophoresis has a number of weaknesses. The overlap of dielectrophoretic response between different cell populations limits effective separation of these cells. The cell-cell interaction forms cell aggregate that can produce dipoles that are different as individual cells. The influence of neighboring cells and nearby channel walls can change cell migration. In addition, the fabrication and integration of electrodes and microfluidic channel is not straightforward. Moreover, the choice of location and geometry of electrodes significantly affects cell sorting. Also the corrosion of the electrodes can lead to failure of the device and local heating can damage the cells.

In addition to electric and magnetic field, acoustic field can also be applied to sort cells. Cells having differences in volume, density and compressibility can be separated by the acoustic

standing waves. The acoustic standing wave induces axial acoustic primary radiation force which sorts the cells into different equilibrium lateral positions (Figure 3.3). The continuous cell sorting fractionation is achieved by combining the acoustic force and laminar flow which split a mixture of cells into multiple outlets[18]. Cell lateral displacement is mainly controlled by acoustic pressure amplitude, wavelength of the standing wave and the flow rate. The essential step to form the equilibrium lateral positions for cell subpopulations is to find the balance between flow rate, acoustic force and the cell properties. The major benefit of using acoustic cell sorting is that it is label-free. However, compared to electric and magnetic cell sorting, acoustic cell sorting is less sensitive and specific, since it relies on only three general cell biophysical properties namely: volume, density and compressibility. Many types of cells have significant overlaps between these properties. Other factors may also reduce cell sorting performance such as the density of medium and the initial cell focusing which controls the cell lateral dispersion.

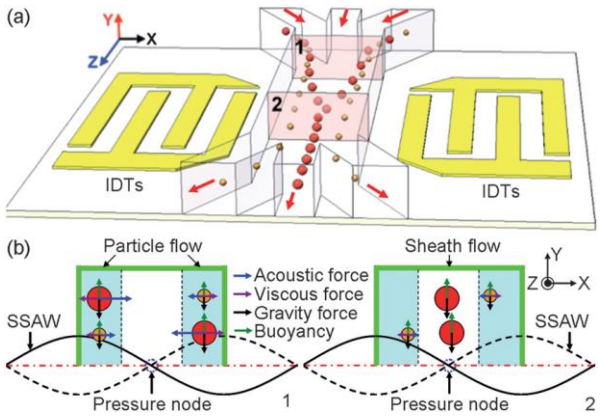

Figure 3.3. Acoustic standing waves induce acoustic radiation forces which align cells into different equilibrium lateral positions. Picture taken from[19]

Another active microfluidic cell sorting method uses optical force[6]. Cells having differences in size and refractive index can be sorted by optical lattices created by interferometric patterns of light. Similar to acoustic forces, the optical forces align cells in different equilibrium

lateral positions, and the cell mixture can be continuously fractionated in a laminar flow provided by a microfluidic channel[5]. Cells do not necessarily require labelling[6]; however, the application of this method is fairly limited since cell size and refractive index are not specific cell markers and large overlaps exist between common cell types. Alternatively, optical forces are used as actuation mechanism in conjunction with fluorescence-activated cell sorter (FACS). Cells are labelled with fluorescence and detected by the FACS and deflected into different flow path by optical forces[5,20] (Figure 3.4). The integration of microfluidics, FACS and optical forces creates a system that requires only a small fraction of cell sample needed compared to conventional FACS. This is particularly suited for applications where sample cells are scarce. Optical cell sorting suffers from several drawbacks. The construction of the interferometric pattern is extremely complex and requires delicate control of laser beams. When optical force is integrated with FACS, the throughput is bottlenecked by the detection mechanism of the FACS, since cell sorting execution takes place only after fluorescent readout. In addition, the sensitivity and specificity are both dependent on the fluorescence labelling which is time-consuming and expensive.

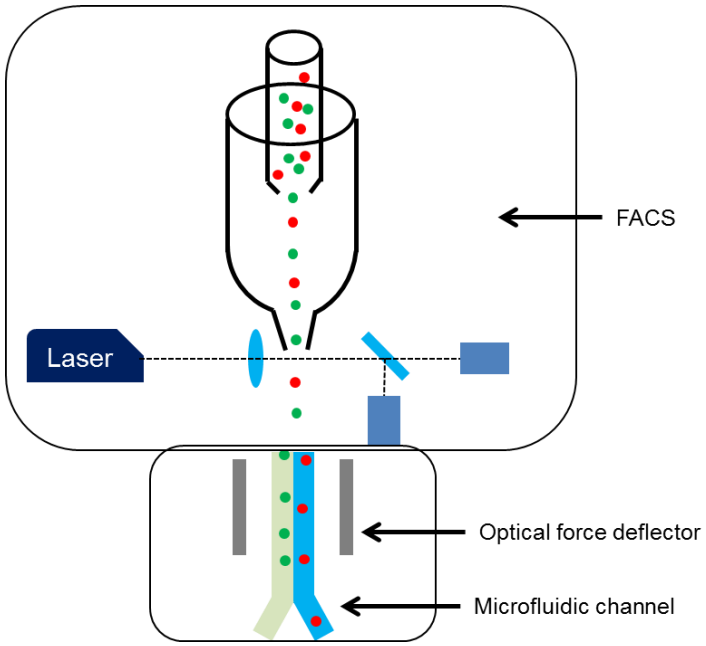

Figure 3.4. Optical force deflectors integrated with microfluidic channel and FACS.

Compared to active sorting methods, passive microfluidic cell sorting methods do not require an externally supplied force to actuate cell and generally do not require cell labelling to initiate actuation. The cell sorting process primarily relies on the hydrodynamics of the flow shaped by the microfluidic geometric features and intrinsic cell biophysical properties. Therefore, most passive methods are label-free. Some of the well-known passive cell sorting methods include: deterministic flow[21,22], constrictive filtration[23], hydrodynamic filtration[24,25] and inertia flow[26]. The major advantages of passive methods are label-free, simple to operate and high throughput. However, the specificity and sensitivity can not surpass the active methods[23,27]. In the follow paragraphs, we will review the some of the passive cell sorting methods and identify their advantages and weaknesses.

One approach to sort cells by their sizes is called deterministic flow[22,28]. In deterministic flow, cells migrate in different paths through asymmetric bifurcation of laminar

flow created by obstacles[21]. The obstacles are comprised of an array of micro-posts with each row slightly offsets from the neighboring rows (Figure 3.5). Cells carried by laminar flows follow distinct streams determined by whether they are bigger or smaller than a critical size[29]. The cell sorting depends on the spacing, arrangement and geometry of micro-posts as well as the applied flow rates. The advantages of deterministic flow cell sorting include label-free, high-throughput, ease of operation as well as continuous fractionation. However, the design of the microposts is an intricate task. Since the design of microposts sets the "critical size" to separate cells, different designs are needed to accommodate a wide range of size differences. Also, deterministic cell sorting only exploits cell size differences which have limited applications.

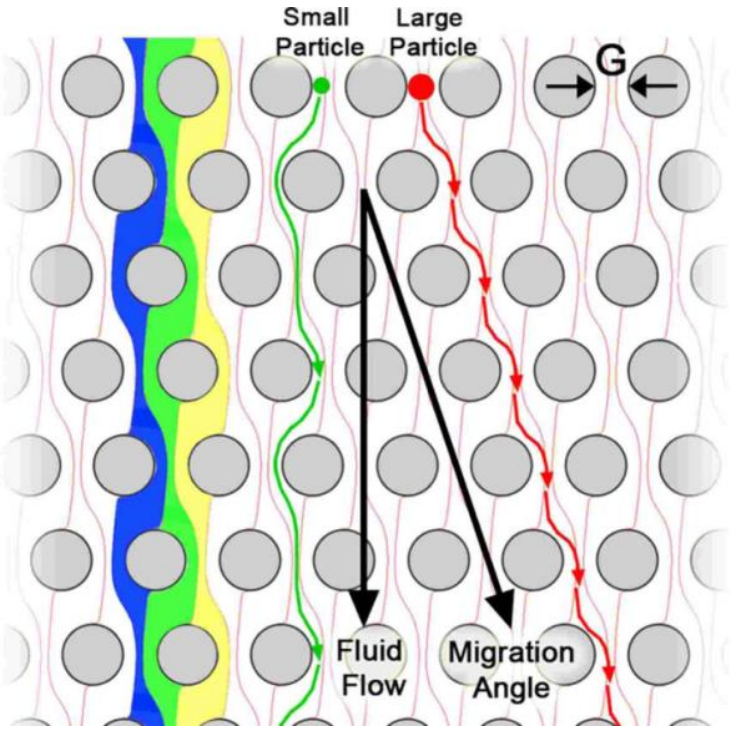

Figure 3.5. Deterministic flow. Particles having different sizes follow distinct flow streams. Picture is taken from[22].

Constrictive filtration is another passive microfluidic cell sorting method. Cells having differences in size and deformability can be sorted this way. Microfluidic channels have an array of microposts or ratchets[30] that form constriction gaps to "trap" stiff and large cells while letting soft and small cells to pass through (Figure 3.6). To increase throughput, massive parallel channels can be integrated into one chip to operate simultaneously[23]. The constriction gaps can also be designed such that the gap sizes gradually decrease to improve cell sorting sensitivity and to avoid severe clogging[31,32]. Constrictive filtration microfluidic channels are simple to fabricate and scale up and the cells can be sorted without labels. The shortcomings include low throughput (less than 10,000 cells per channel[30]) and clogging caused by the captured cells. Since the constrictions arrest cells moving in the flow direction, the passage becomes blocked as the cells occlude the gaps. Clogging not only changes flow patterns but also obstructs cell passages, which increases flow resistance and limits the throughput. As a result, the hydrodynamic pressure is increased as cells gradually occlude the flow passages.

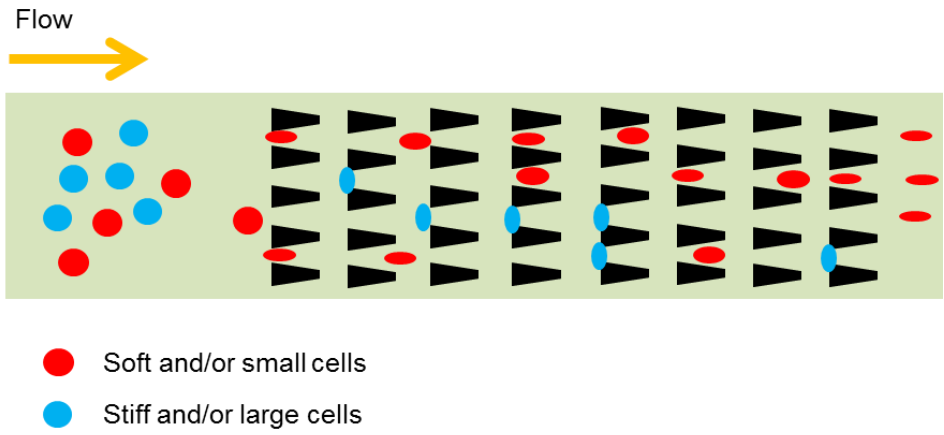

Figure 3.6. Constrictive filtration microfluidic channel. Large and/or stiff cells are stuck in between the constriction gaps while small and/or soft cells pass through and are collected.

Hydrodynamic filtration is a term describing a group of microfluidic channel designs that manipulate fluid streams to impart cell separation in a contactless manner. The four general techniques include: margination (Fahrus and Lindqvist effect)[33], field flow fractionation[24], flow pinching[34], and ridge induced circulation[25]. However, there are many design variations for each technique. Figure 3.7 shows four designs representing each technique. Margination utilizes the parabolic profile of laminar flow and cell collisions to sort cells by size and deformability. The larger and/or stiffer cells are displaced to a location near the channel wall while smaller and/or softer cells remain to concentrate toward the central axis of the channel in the crowded environment(Figure 3.7a). Field flow fractionation sort cells by splitting the channel flow into multiple streams. The laminar flow profile and the relative flow rates of the separated streams control the cell separation. Due to difference in drag forces acting on cells, smaller cells are removed from the bigger cells by splitting the channel flow into low velocity streams while larger cells remain in higher velocity stream (Figure 3.7b). Pinched flow designs force the cell mixture into a narrow section of channel with the use of a focusing stream. Cells are aligned in a narrow file and travel to an expansion section of the channel. Due to the different flow rates between the cell-carrying stream and the focusing stream and the channel expansion, cells having different sizes migrate to different lateral position (Figure 3.7c). Larger particles experience greater drag force and remain closer to the channel axis while small particles migrate near the channel walls. Slanted ridge design was derived from micro-mixers where the ridges generate secondary flows in the form of circulations. In micro-mixers, the circulations aid the diffusion of chemical molecules. For cell separation, the circulation creates different cell trajectories depending on cell size and shape because the difference in drag forces acted on cells. Cells are pushed along the ridges in the transverse direction while flowing through the channel. Smaller

cells move along the ridges while the bigger cells move perpendicular to the ridges (Figure 3.7d). Hydrodynamic filtration can sort cells by size[35], mass[36], deformability[37] and shape[25]. Individual cells can also be encapsulated in single droplet to decrease heterogeneities and improve sorting efficiency[38,39].

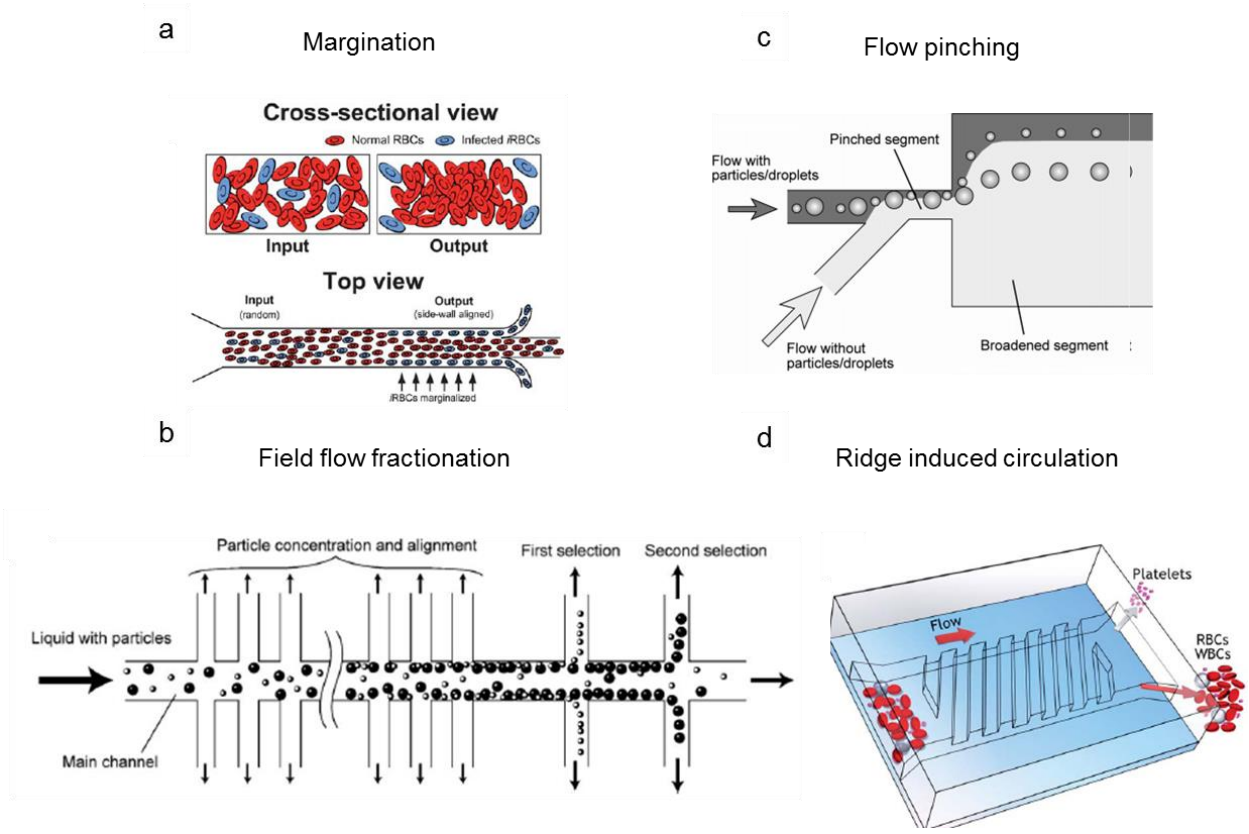

Figure 3.7. Hydrodynamic filtration microfluidics. a) Margination (Fahrus and Lindqvist effect). Size and deformability based cell sorting. Small and/or soft cells concentrate near the center of the channel while large and/or stiff cells move closer to the channel walls. Picture is taken from[37]. b) Field flow fractionation. Cells are sorted by size. The main channel flow is spitted into several streams with slower velocity. Smaller cells are gradually siphoned into the slow-velocity streams. Picture is taken from[24]. c) Flow pinching. The expansion of the channel force cells of difference sizes flow in different lateral positions. Picture is taken from[39]. d) Ridge inducted circulation. The diagonal ridges generate circulations which sort cells by size, and shape. Picture is taken from[40].

Hydrodynamic filtration offers several unique advantages over other methods. The throughput of hydrodynamic filtration can be as high as millions of cells per second[40]. Like other passive cell sorting methods, cells do not need to be labelled. Since the sorting process is contactless, cells are not strongly affected by the sorting process. The operation and fabrication of the microfluidic device are straightforward and the fabrication can be scaled up to include multiple parallel channels. The major disadvantage of hydrodynamic filtration is the inability to decouple the convoluted cell biophysical properties. For example, in the margination method, if the small cells are stiff and the larger cells are soft, the influence of each of these properties counteracts the other and can not be effectively distinguished. As a result, the hydrodynamic filtration is best suited when the cell populations have only one dominating biophysical property difference. In addition, because hydrodynamic filtration is a passive method, it lacks high specificity and sensitivity compared to the active sorting methods[17].

The recent discovery of inertial force in microfluidics spurred strong interests in exploiting this phenomenon for cell sorting[41]. Traditionally, the inertial effect was largely neglected in light of the favor of the low Reynolds number Stokes flow conditions in most microfluidic channels. Although Stokes flow is laminar, the converse is not necessarily true. For instance, long and curved spiral channels create secondary flows due to mismatch of velocity in the downstream direction between fluid near the center axis and near the walls[42]. The result is a two-symmetrical circulation which is commonly known as the Dean flow (Figure 3.8a). The magnitude of the circulations depends on the ratio of the channel dimensions to the radius of the curvature (Figure 3.8b). The cells flowing in a long and curved microfluidic channel will experience both inertial lift force and drag force from Dean flow. The two opposing forces set the equilibrium lateral positions of cells that depend on both the cell size and deformability.

Another microfluidic channel design that exploits the inertial effect is the serpentine channel[43] (Figure 3.8c). Similar to the long and curved channels, the particle equilibrium lateral position is determined by the net effect of drag force from Dean flow and inertial lift force. The shear-gradient induced inertial lift force act on particles and push them closer to the wall while the drag force counter-act inertial lift force in the opposite direction. In addition to cell sorting, inertial microfluidics can also order and focus cells[44]. Thus, the sheath flows which are commonly used for cell focusing are no longer needed[45]. Inertial microfluidics shares many of the advantages of hydrodynamic filtration. Additionally, inertial microfluidics can be integrated into other cell sorting microfluidic designs to provide cell ordering and focusing (Figure 3.8d). However, inertial microfluidics also bears the same disadvantages of hydrodynamic filtrations. In particular, inertial microfluidics is prone to failure when cell size and shape are rival properties[46]. In addition, the relative displacement induced by inertial effects is minor, consisting of a fraction of a cell diameter. Therefore noise within the separation process may be more impactful.

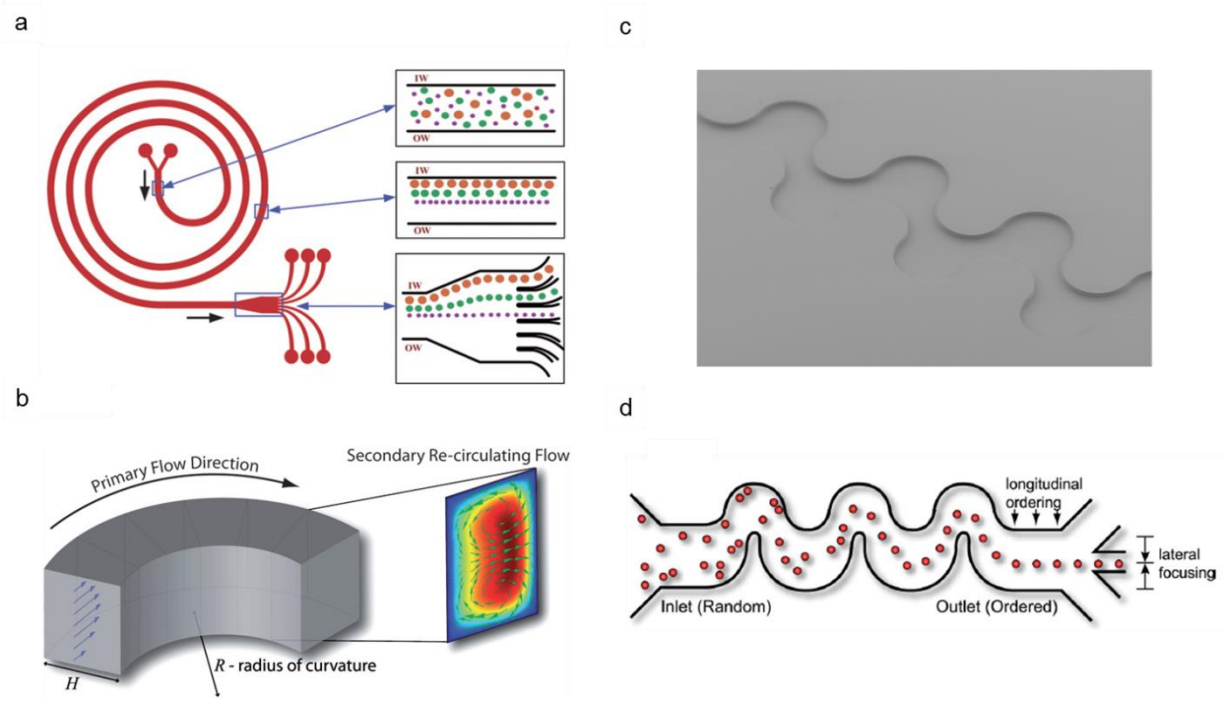

Figure 3.8. Inertia microfluidics used in cell sorting. a) A long and curved spiral microfluidic channel. Picture is taken from[42]. b) Dean flow in the form of two symmetric vertices generated by the microfluidic channel. Picture is taken from[26]. c) A SEM image of a serpentine-shaped microfluidic channel. d) Cells can be ordered and focused in a serpentine microfluidic channel. Picture is taken from[43].

Cell sorting has many practical applications in disease diagnostics, tissue engineering, and cell biology. The research effort should focus on three competing performance measures: sensitivity, specificity and throughput. Active sorting methods have higher sensitivity and specificity but may lack throughput while passive methods have higher throughput but lower sensitivity and specificity. The logical action is to combine the active sorting methods and the passive sorting methods into an integrated microfluidic cell sorting platform. Several research groups have attempted this by integrating two or more passive and/or active cell sorting

mechanisms into one microfluidic chip[47-50]. Although still at early stage, the experiment has shown some promising results.

Thus far, we have seen there is vast interest in developing microfluidic cell-sorting platforms. Our goal is to develop a new label-free, continuous method that can quickly sort cells using cell biophysical properties. In the next section, we explain our cell sorting mechanism.

3.2 Stiffness Dependent Cell Separation Principle

Cell sorting by biophysical properties is an emerging field of research. Although a variety of techniques demonstrate separation by physical parameters such as size[51], mass[52], and adhesion [53], a straightforward method to separate cells by mechanical stiffness and viscosity would also benefit biomedical capabilities.

We use a microfluidic channel decorated by periodic diagonal ridges that compress the flowing cells in rapid succession (Figure 3.9a and 3.9b). The compression in combination with secondary flows in the ridged microfluidic channel translates each cell perpendicular to the channel axis in proportion to its stiffness. To investigate the physical principle that results in cells of different stiffness values to separate within the microfluidic channel, we performed numerical simulations of deformable fluid-filled capsules flowing in a ridged microfluidic channel. Figure 3.9c shows the simulated spatial trajectories of centers of mass of stiff and soft capsules overlayed with the experimentally observed trajectories of a stiff and soft cell respectively. The simulation shows that compliant capsules having difference in stiffness exhibit diverging trajectories that are in agreement with cell trajectories observed in the experiments.

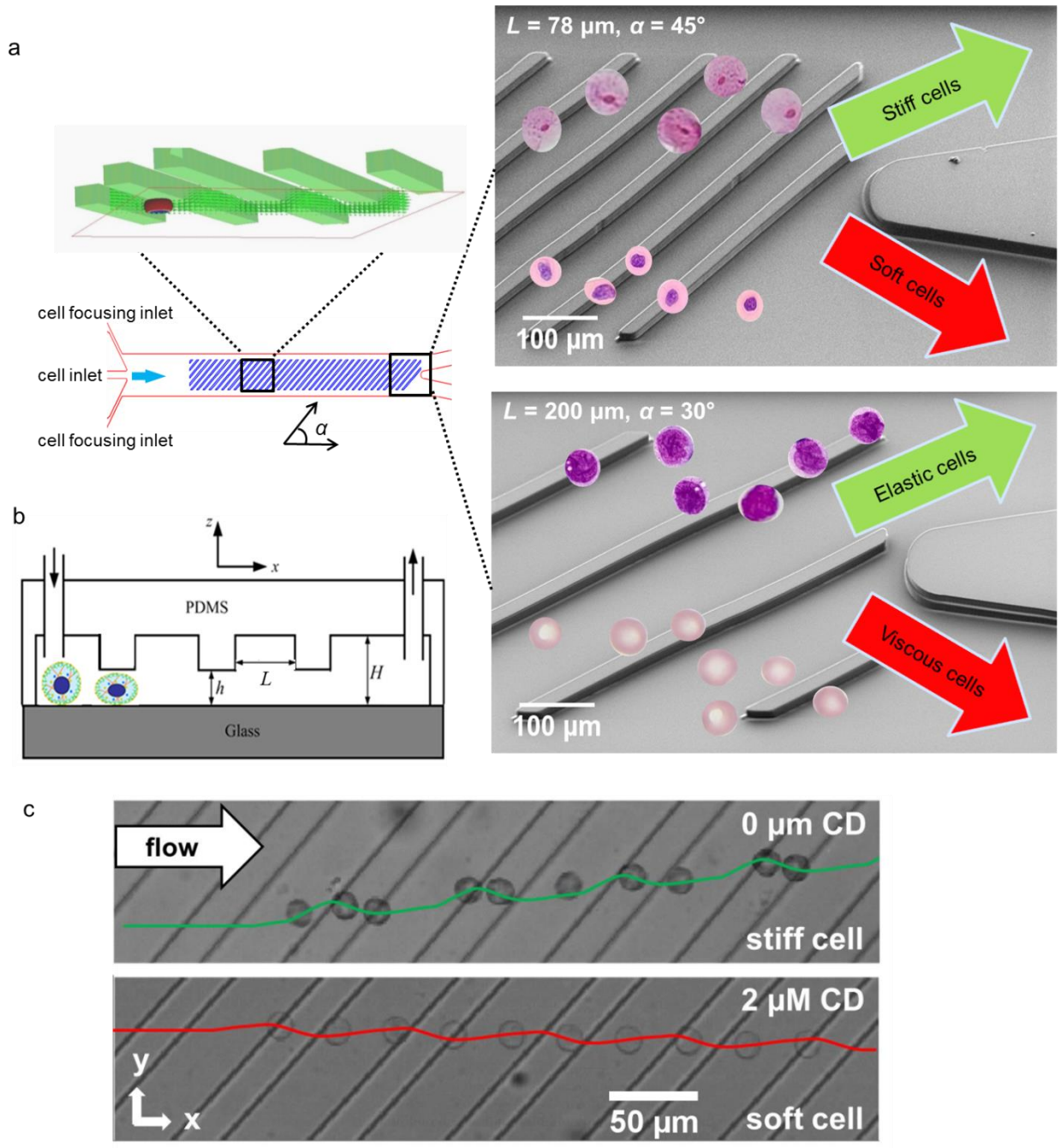

Figure 3.9. Microfluidic cell separation channel. a) Cell mixtures are infused into the microfluidic channel using a syringe pumps which control the flow rates. Cells are focused by two sheath flows and subsequently compressed in rapid succession by diagonal ridges which alter cell trajectories depending on cell biophysical properties. b) The channel design parameters in our optimization process included the following: channel gap size, *h*, ridge spacing, *L*, ridge angle, *α*, and the number of compressions from inlet to outlet that cells experience. c) Overlay of still frames from a video of an untreated and 2 μM CytoD softened K562 cells flowing in a channel. Each micrograph is an overlay of 10 still frames at equal 10 ms time intervals from a

video taken at 1200 fps. Green and red solid lines represent numerical simulations of the flow trajectory stiff and soft capsules.

Cells propelled by fluid flow experience a hydrodynamic (drag) force due to the viscous fluid F_D and an elastic force F_R when they confront periodic ridges in a microfluidic channel (Figure 3.10a). This transversal force arises due to cell deformation and, therefore, is proportional to the cell stiffness. Thus, cells with different stiffness experience different elastic forces as they pass through periodical constrictions. Thermodynamically, this elastic force is associated with the gradient of system free elastic energy due to cell elastic deformation (see Figure 3.10b for the free elastic energy of capsule compression for 3 representative stiffness values) and, therefore, is in the direction perpendicular to the ridge. Since the ridges are oriented with an angle relative to the bulk fluid flow, this force is not aligned with the flow direction, but rather has a component that displaces cells normal to the flow (Figure 3.10a). The elastic force has different magnitude when a cell enters and leaves a constriction. However, diagonal ridges create an asymmetry in cell trajectory that results in a net transversal displacement. Stiffer cells experience a larger elastic force and, thus, greater transversal displacement in the positive transverse direction.

When cells are soft, the elastic force is weak and cells move with fluid flow streamlines. Diagonal ridges create a flow circulation in the microchannel, in which the fluid near the channel bottom flows in the negative transverse direction (Figure 3.10c). Since cells in the stream are located near the bottom channel wall, soft cells are transported by the circulating flow in the negative transverse direction. As a result, soft and stiff cells migrate to opposite sides of the ridged microfluidic channel, thereby separating according to their mechanical stiffness.

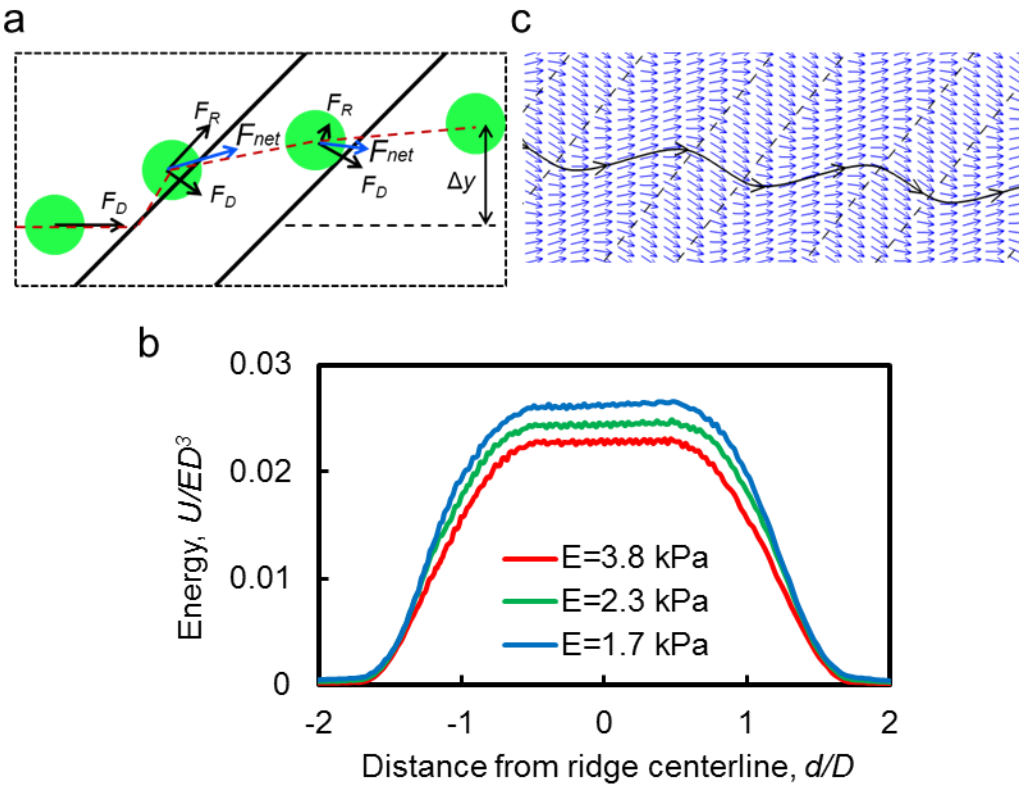

Figure 3.10. Stiffness-based microfluidic cell separation principle. a) Cells experience both a hydrodynamic force, F_D, and an elastic force, F_R, as the cells are deformed by the ridges. The elastic force varies with cell stiffness. The net transverse displacement is a result of interplay between the hydrodynamic force and stiffness-dependent elastic force. b) The free elastic energy associated with cell compression, U, increases to a maximum as the cell passes through the ridge and varies as a function of cell Young's modulus. The difference in the gradient of free energy of soft and stiff cells gives rise to different transverse forces that deflect cell trajectories in the microfluidic channel perpendicular to the ridge and dependent on cell mechanical stiffness. c) Simulation of velocity field and the resulting streamlines. The diagonal ridges create secondary flows (blue arrows represent velocity vector of the flow) that circulate underneath the ridges which propels soft cells in the negative transverse direction. The trajectory of soft cells follows closely to the streamline due to the minimal elastic force.

Of course, cells are not perfectly elastic but rather viscoelastic materials. Cell dynamic mechanical response to compression can be divided into two components characterized by a storage modulus (elastic, G') and a loss modulus (viscous, G''). Since the channel ridges compress all cells to the same size, differences in cell size result in different amounts of

deformation. To account for differences in cell size, we can derive a single parameter called cell deformation energy to group the cell elasticity and cell size into one variable. In this manner, we normalize the cell elasticity with respect to cell size. We employ a time-independent Young's modulus and cell diameter to represent elastic modulus and cell size respectively. To determine the deformation energy, we apply the Hertzian contact mechanics model in which the equivalent elastic modulus E^* is

$$\frac{1}{E^*} = \frac{1-\upsilon_{\text{cell}}^2}{E_{\text{cell}}} + \frac{1-\upsilon_{\text{channel}}^2}{E_{\text{channel}}} \qquad (1)$$

where υ is the Poisson's ratio and E is the Young's modulus. We assumed the cells have a Poisson's ratio to be 0.33. When we model the deformed cell as an elastic sphere, the deformation energy is derived by integrating the compression force, F, over the cell deformation S.

$$U = \int F \cdot dS = \int \frac{4}{3} E^* \left(\frac{d}{2}\right)^{0.5} (S)^{1.5} \cdot dS \qquad (2)$$

where S is the amount of deformation which is the difference between cell diameter, d, and ridge gap h. As a result the deformation energy accounts for both cell elasticity and cell size.

Our model describing the cell trajectory in the microfluidic channel depends on three factors: the size-adjusted elasticity represented by the deformation energy, the cell viscosity, and the strength of the secondary flow. The size-adjusted elasticity and viscosity are cell biophysical properties but the strength of the secondary flow is controlled by the channel geometry and experimental flow rate. A variety of studies of slanted diagonal ridges used in micro-mixer applications show that a 45 degree angle of ridges induces maximal secondary flow[54]. Cell

trajectory at the ridge mainly depends on the cell biophysical properties while cell trajectory in between ridges is controlled by the strength of the circulation.

Since the cells are viscoelastic materials, their dynamic response after compression is time-dependent. Cell relaxation depends not only on a short time scale which occur between sequential ridge compressions but also on a longer time scale due to repeated compressions[55]. The extended number of repeated compressions causes changes in the cellular structures such as the cell nucleus and cytoskeleton[55]. Therefore, the cell lateral displacement in the channel may vary as cellular relaxation occurs over the course of cell sorting.

3.3 Cell Trajectory is a Function of Cell Stiffness

A model using chemically softened K562 cells was created to validate the stiffness dependent cell separation hypothesis. In Chapter 2, it is shown that cell stiffness is primarily contributed by the structure of cytoskeleton networks. Thus, modification of the cytoskeleton is expected to have profound effect on cell stiffness. Cytochalasin D is a cell-permeable and potent actin polymerization inhibitor drug. CytoD destabilizes the cytoskeleton by binding the F-actin polymer and stops it polymerization. The cell stiffness can be modified with different concentration of CytoD (Figure 3.11c). CytoD was used to chemically soften the K562 cells to create cell subpopulations that only differ by their mechanical stiffness. Figure 3.11a shows a collection of high-speed video micrograph still frames of a single cell with increasing CytoD concentrations flowing through the microfluidic device are overlayed at equal time intervals. The video microscopy revealed that the stiffer cells have a tendency to move in the direction parallel to the ridge, resulting in a net positive transverse displacement (positive y-direction)

perpendicular to flow direction. As the stiffness of K562 cell decreases with increasing CytoD concentration, the positive transverse displacement was reduced and became negative. Thus, cells exposed to lower CytoD concentration (1 µM and lower) exhibit a net positive transverse displacement, whereas cells treated with higher CytoD concentration (1.5 µM and higher) resulted in a net negative transverse displacement. The averaged transverse displacement per ridge of K562 cells is shown in a box-and-whisker plot (n = 110 for each CytoD concentration, Figure 3.11b).

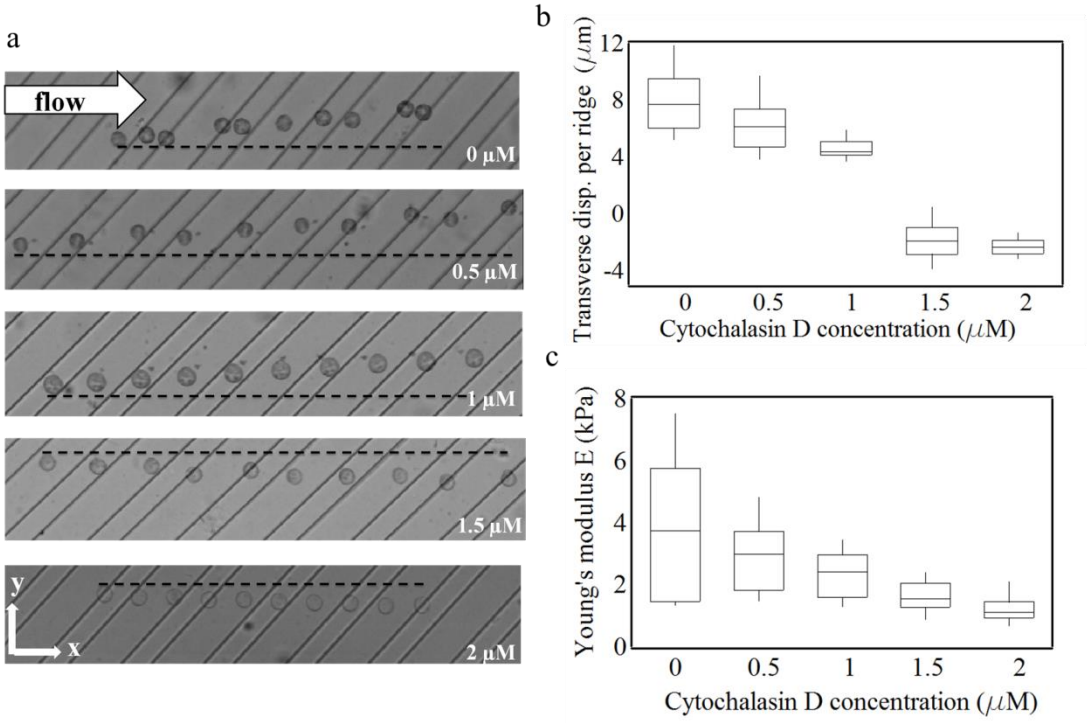

Figure 3.11. Cell trajectory is a function of cell stiffness. a) Micrographs showing the trajectories of single K562 cells softened with different amounts of cytochalasin D. Each micrograph is an overlay of 10 still frames at equal time interval from a video taken at 3000 fps. b) and c) show variations of K562 cell transverse displacement (n = 110 for each CytoD concentration) and Young's modulus ($n \geq 20$ for each CytoD concentration) with increasing CytoD concentration, respectively. Here, the center line represents the mean value, the top and lower boxes represent 50 percentile, and the whiskers represent the remaining data.

To verify that the CytoD treated K562 cells were indeed mechanically softened, AFM measurements were conducted on identical cell populations and showed a decrease in Young's modulus with increasing CytoD concentrations (Figure 3.11c). Therefore, the transverse displacement of cells flowing through the device increases with increasing average Young's modulus, supporting the heypotheisi described by Figure 3.10a. The AFM measurements were conducted on K562 cells ($n \geq 20$ for each CytoD concentration) incubated with an increasing concentration of CytoD. The CytoD has effectively decreased the Young's modulus of K562 cells by 70%, which is in agreement with previous studies [56,57]. For CytoD concentrations greater than 2 μM, additional softening was negligible.

3.4 References

1. Miltenyi S, Muller W, Weichel W, Radbruch A (1990) High-gradient magnetic cell-separation with MACS. Cytometry 11: 231-238.
2. Pamme N, Wilhelm C (2006) Continuous sorting of magnetic cells via on-chip free-flow magnetophoresis. Lab on a Chip 6: 974-980.
3. Becker FF, Wang XB, Huang Y, Pethig R, Vykoukal J, et al. (1995) Separation of human breast-cancer cells from blood by differential dielectric affinity. Proceedings of the National Academy of Sciences of the United States of America 92: 860-864.
4. Hu XY, Bessette PH, Qian JR, Meinhart CD, Daugherty PS, et al. (2005) Marker-specific sorting of rare cells using dielectrophoresis. Proceedings of the National Academy of Sciences of the United States of America 102: 15757-15761.
5. Wang MM, Tu E, Raymond DE, Yang JM, Zhang HC, et al. (2005) Microfluidic sorting of mammalian cells by optical force switching. Nature Biotechnology 23: 83-87.
6. MacDonald MP, Spalding GC, Dholakia K (2003) Microfluidic sorting in an optical lattice. Nature 426: 421-424.
7. Ding X, Lin S-CS, Lapsley MI, Li S, Guo X, et al. (2012) Standing surface acoustic wave (SSAW) based multichannel cell sorting. Lab on a Chip 12: 4228-4231.
8. Yang AHJ, Soh HT (2012) Acoustophoretic Sorting of Viable Mammalian Cells in a Microfluidic Device. Analytical Chemistry 84: 10756-10762.
9. Fu AY, Spence C, Scherer A, Arnold FH, Quake SR (1999) A microfabricated fluorescence-activated cell sorter. Nature Biotechnology 17: 1109-1111.
10. Xia N, Hunt TP, Mayers BT, Alsberg E, Whitesides GM, et al. (2006) Combined microfluidic-micromagnetic separation of living cells in continuous flow. Biomedical Microdevices 8: 299-308.
11. Lee H, Purdon AM, Westervelt RM (2004) Manipulation of biological cells using a microelectromagnet matrix. Applied Physics Letters 85: 1063-1065.
12. Yu M, Stott S, Toner M, Maheswaran S, Haber DA (2011) Circulating tumor cells: approaches to isolation and characterization. Journal of Cell Biology 192: 373-382.
13. Pethig R (2010) Review Article-Dielectrophoresis: Status of the theory, technology, and applications. Biomicrofluidics 4: 2.
14. Pethig R, Markx GH (1997) Applications of dielectrophoresis in biotechnology. Trends in Biotechnology 15: 426-432.
15. Fiedler S, Shirley SG, Schnelle T, Fuhr G (1998) Dielectrophoretic sorting of particles and cells in a microsystem. Analytical Chemistry 70: 1909-1915.
16. Vahey MD, Voldman J (2008) An equilibrium method for continuous-flow cell sorting using dielectrophoresis. Analytical Chemistry 80: 3135-3143.
17. Lenshof A, Laurell T (2010) Continuous separation of cells and particles in microfluidic systems. Chemical Society Reviews 39: 1203-1217.
18. Petersson F, Aberg L, Sward-Nilsson AM, Laurell T (2007) Free flow acoustophoresis: Microfluidic-based mode of particle and cell separation. Analytical Chemistry 79: 5117-5123.
19. Shi JJ, Huang H, Stratton Z, Huang YP, Huang TJ (2009) Continuous particle separation in a microfluidic channel via standing surface acoustic waves (SSAW). Lab on a Chip 9: 3354-3359.

20. Perroud TD, Kaiser JN, Sy JC, Lane TW, Branda CS, et al. (2008) Microfluidic-based cell sorting of Francisella tularensis infected macrophages using optical forces. Analytical Chemistry 80: 6365-6372.
21. Huang LR, Cox EC, Austin RH, Sturm JC (2004) Continuous particle separation through deterministic lateral displacement. Science 304: 987-990.
22. Inglis DW (2009) Efficient microfluidic particle separation arrays. Applied Physics Letters 94: 1.
23. Zhang WJ, Kai K, Choi DS, Iwamoto T, Nguyen YH, et al. (2012) Microfluidics separation reveals the stem-cell-like deformability of tumor-initiating cells. Proceedings of the National Academy of Sciences of the United States of America 109: 18707-18712.
24. Yamada M, Seki M (2005) Hydrodynamic filtration for on-chip particle concentration and classification utilizing microfluidics. Lab on a Chip 5: 1233-1239.
25. Choi S, Song S, Choi C, Park J-K (2007) Continuous blood cell separation by hydrophoretic filtration. Lab on a Chip 7: 1532-1538.
26. Di Carlo D (2009) Inertial microfluidics. Lab on a Chip 9: 3038-3046.
27. Didar TF, Tabrizian M (2010) Adhesion based detection, sorting and enrichment of cells in microfluidic Lab-on-Chip devices. Lab on a Chip 10: 3043-3053.
28. Green JV, Radisic M, Murthy SK (2009) Deterministic Lateral Displacement as a Means to Enrich Large Cells for Tissue Engineering. Analytical Chemistry 81: 9178-9182.
29. Holm SH, Beech JP, Barrett MP, Tegenfeldt JO (2011) Separation of parasites from human blood using deterministic lateral displacement. Lab on a Chip 11: 1326-1332.
30. Bow H, Pivkin IV, Diez-Silva M, Goldfless SJ, Dao M, et al. (2011) A microfabricated deformability-based flow cytometer with application to malaria. Lab on a Chip 11: 1065-1073.
31. Mohamed H, Murray M, Turner JN, Caggana M (2009) Isolation of tumor cells using size and deformation. Journal of Chromatography A 1216: 8289-8295.
32. McFaul SM, Lin BK, Ma HS (2012) Cell separation based on size and deformability using microfluidic funnel ratchets. Lab on a Chip 12: 2369-2376.
33. Shevkoplyas SS, Yoshida T, Munn LL, Bitensky MW (2005) Biomimetic autoseparation of leukocytes from whole blood in a microfluidic device. Analytical Chemistry 77: 933-937.
34. Yamada M, Nakashima M, Seki M (2004) Pinched flow fractionation: Continuous size separation of particles utilizing a laminar flow profile in a pinched microchannel. Analytical Chemistry 76: 5465-5471.
35. Yamada M, Kano K, Tsuda Y, Kobayashi J, Yamato M, et al. (2007) Microfluidic devices for size-dependent separation of liver cells. Biomedical Microdevices 9: 637-645.
36. Huh D, Bahng JH, Ling YB, Wei HH, Kripfgans OD, et al. (2007) Gravity-driven microfluidic particle sorting device with hydrodynamic separation amplification. Analytical Chemistry 79: 1369-1376.
37. Hou HW, Bhagat AAS, Chong AGL, Mao P, Tan KSW, et al. (2010) Deformability based cell margination-A simple microfluidic design for malaria-infected erythrocyte separation. Lab on a Chip 10: 2605-2613.
38. Chabert M, Viovy JL (2008) Microfluidic high-throughput encapsulation and hydrodynamic self-sorting of single cells. Proceedings of the National Academy of Sciences of the United States of America 105: 3191-3196.

39. Maenaka H, Yamada M, Yasuda M, Seki M (2008) Continuous and size-dependent sorting of emulsion droplets using hydrodynamics in pinched microchannels. Langmuir 24: 4405-4410.
40. Choi S, Ku T, Song S, Choi C, Park JK (2011) Hydrophoretic high-throughput selection of platelets in physiological shear-stress range. Lab on a Chip 11: 413-418.
41. Hur SC, Henderson-MacLennan NK, McCabe ERB, Di Carlo D (2011) Deformability-based cell classification and enrichment using inertial microfluidics. Lab on a Chip 11: 912-920.
42. Kuntaegowdanahalli SS, Bhagat AAS, Kumar G, Papautsky I (2009) Inertial microfluidics for continuous particle separation in spiral microchannels. Lab on a Chip 9: 2973-2980.
43. Di Carlo D, Irimia D, Tompkins RG, Toner M (2007) Continuous inertial focusing, ordering, and separation of particles in microchannels. Proceedings of the National Academy of Sciences of the United States of America 104: 18892-18897.
44. Di Carlo D, Edd JF, Irimia D, Tompkins RG, Toner M (2008) Equilibrium separation and filtration of particles using differential inertial focusing. Analytical Chemistry 80: 2204-2211.
45. Bhagat AAS, Kuntaegowdanahalli SS, Kaval N, Seliskar CJ, Papautsky I (2010) Inertial microfluidics for sheath-less high-throughput flow cytometry. Biomedical Microdevices 12: 187-195.
46. Masaeli M, Sollier E, Amini H, Mao W, Camacho K, et al. (2012) Continuous Inertial Focusing and Separation of Particles by Shape. Physical Review X 2: 3.
47. Moon HS, Kwon K, Kim SI, Han H, Sohn J, et al. (2011) Continuous separation of breast cancer cells from blood samples using multi-orifice flow fractionation (MOFF) and dielectrophoresis (DEP). Lab on a Chip 11: 1118-1125.
48. Kim U, Soh HT (2009) Simultaneous sorting of multiple bacterial targets using integrated Dielectrophoretic-Magnetic Activated Cell Sorter. Lab on a Chip 9: 2313-2318.
49. Yao B, Luo GA, Feng X, Wang W, Chen LX, et al. (2004) A microfluidic device based on gravity and electric force driving for flow cytometry and fluorescence activated cell sorting. Lab on a Chip 4: 603-607.
50. Cho SH, Chen CH, Tsai FS, Godin JM, Lo YH (2010) Human mammalian cell sorting using a highly integrated micro-fabricated fluorescence-activated cell sorter (mu FACS). Lab on a Chip 10: 1567-1573.
51. Gawad S, Schild L, Renaud P (2001) Micromachined impedance spectroscopy flow cytometer for cell analysis and particle sizing. Lab on a Chip 1: 76-82.
52. Godin M, Delgado FF, Son SM, Grover WH, Bryan AK, et al. (2010) Using buoyant mass to measure the growth of single cells. Nature Methods 7: 387-U370.
53. Singh A, Suri S, Lee T, Chilton JM, Cooke MT, et al. (2013) Adhesion strength-based, label-free isolation of human pluripotent stem cells. Nature Methods 10: 438-+.
54. Lynn NS, Dandy DS (2007) Geometrical optimization of helical flow in grooved micromixers. Lab on a Chip 7: 580-587.
55. Mak M, Erickson D (2013) A serial micropipette microfluidic device with applications to cancer cell repeated deformation studies. Integrative Biology 5: 1374-1384.
56. Wakatsuki T, Schwab B, Thompson NC, Elson EL (2001) Effects of cytochalasin D and latrunculin B on mechanical properties of cells. Journal of Cell Science 114: 1025-1036.

57. Schulze C, Muller K, Kas JA, Gerdelmann JC (2009) Compaction of Cell Shape Occurs Before Decrease of Elasticity in CHO-K1 Cells Treated With Actin Cytoskeleton Disrupting Drug Cytochalasin D. Cell Motility and the Cytoskeleton 66: 193-201.

CHAPTER 4

MICROFLUIDIC CHANNEL DESIGN, FABRICATION AND OPTIMIZATION FOR CELL SORTING

In section 4.1, we review two fabrication techniques: photolithography and soft lithography which are used to make the microfluidic cell sorters. We also describe in detail the design and fabrication of the microfluidic cell sorters and the cell sorting experiment. In section 4.2, we discuss the important factors that affect cell sorting such as channel geometry. In section 4.3, we consider the effect of flow rates.

4.1 Microfluidic Channel Fabrication and Characterization

The micro-fabrication techniques based on pattern transfer were originally demonstrated in the semiconductor industry. We choose photolithography and soft lithography because of their simplicity, cost-effectiveness, and potential for high-volume and high-speed manufacturing.

Photolithography is a process that prints pre-formed 2-D patterns onto a thin film layer on a substrate[1]. The process requires the deposition of photo-sensitive polymer (photoresists, PR) on the substrate (commonly silicon wafer) and UV exposure through a mask that permits only defined regions to be exposed (Figure 4.1). The photo-masks are made using electron-beam lithography which uses an electron beam to etch chromium deposited on a quartz glass substrate. The UV source typically emits either 365 nm or 405 nm wavelength of UV which either cures (negative PR) or removes the photoresists (positive PR). The amount of exposure measured by

dose (UV intensity multiplied by exposure time) depends on the feature aspect ratios and the PR deposited.

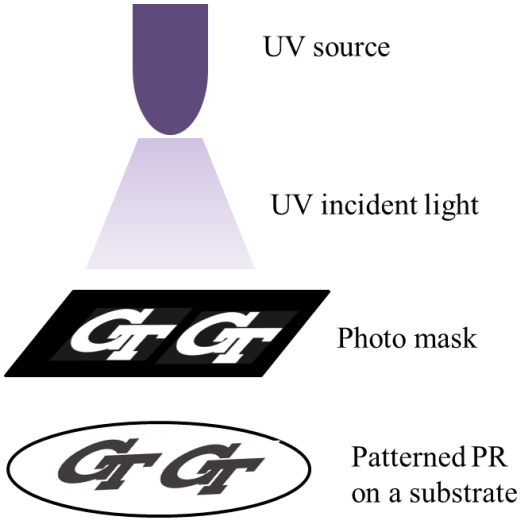

Figure 4.1. Photolithography. Photolithography process uses a UV source to emit UV (either 365 or 405 nm wavelength) which passes through the photo-masks at defined regions. The patterns of the photomasks are formed by photoresists on a substrate either through crosslinking (negative PR) or dissolving (positive PR).

Soft lithography is a non-traditional micro-fabrication process that is particularly suited for biomedical micro-electromechanical system BioMEMs devices[2]. Some of the advantages include biocompatible, chemically modifiable, soft and flexible, and optically transparent. A particular type of soft lithography is called replica molding where uncured polymer such as Polydimethylsiloxane (PDMS)[3] and Poly(methyl methacrylate) (PMMA)[4] are poured onto a permanent mold. After baking and curing, the polymer conforms to the shape of the mold and contains the features that are replicas of the mold (Figure 4.2). Compared to traditional injection molded parts the replica molded parts have higher fidelity, resolution, and yield per mold[5].

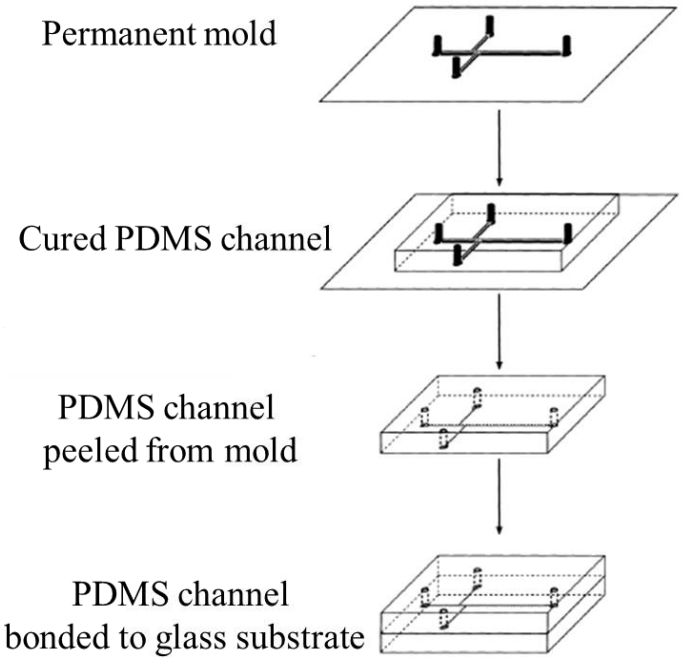

Figure 4.2. Soft lithography. Soft lithography uses a permanent mold which contains the replica of the geometric features. The PDMS or other polymer precursors are poured onto the mold and cured through incubation. The cured PDMS has a reciprocal replicate of the features on the mold. The microfluidic channels are formed by bonding the PDMS to a glass substrate.

Photolithography and soft lithography were selected to fabricate the microfluidic cell sorters for several reasons. The process is simple and repeatable and the molded cell sorters are highly reproducible. More importantly, they allow the use of PDMS, a biocompatible and optically transparent polymer which permits oxygen permeation and chemical modification. Furthermore, the material cost per chip is less than fifty cents. In addition, multiple designs of cell sorters can be molded on a single run. This is particularly helpful when testing different geometric parameters of the cell sorters.

The photolithographic masks were designed using SolidWorks and AutoCAD. Solid lines are jointed to construct closed contours of geometric features. These features are subsequently

flashed using CleWin4, a commercially available mask generating software to create solid patterns. The photo-masks were made at the Georgia Tech clean room mask shop. Chromium is deposited onto a five inch by five inch quartz glass using photolithography. Then, electron beam lithography is used to remove the chromium which leaves the desired solid patterns. An example of the photo mask is shown in Figure 4.3. Bright field masks are used instead of dark field masks for several technical reasons. First, bright field masks are easier to detach from the wafer after "hard contact". The negative photoresists, SU-8, used to construct the mold is an epoxy-based polymer which is highly "sticky". In addition, the mask features are made of chromium which is typically applied as adhesion layer for thin film deposition process. Therefore, to avoid unwanted "sticking" of the wafer to the mask during alignment and exposure, bright field mask is a better choice. Another reason for using bright field mask is that it helps in aligning sequential layers by enhancing the contrast between alignment marks on the masks and photoresists deposited on the substrate.

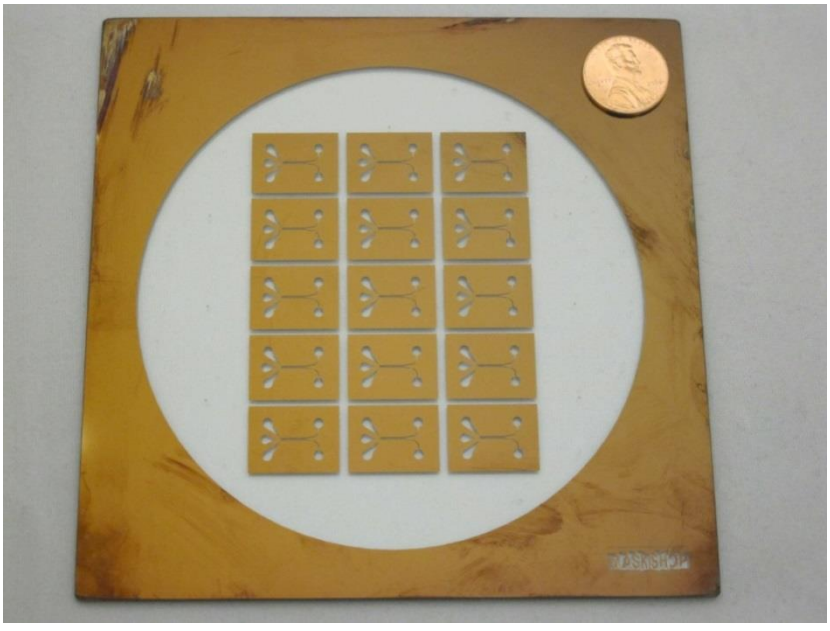

Figure 4.3. A picture of a 5 inch by 5 inch bright field photo-mask. The patterns are created by electron beam lithography of chromium on a quartz glass substrate.

To create gap space formed by the ridge and the substrate, at least two layers of SU-8 polymers are needed to build the channel mold. For gap sizes less than 10 µm, two layers are used and for gap sizes above 10 µm three or more layers are used. However, only two masks are needed: one for the channel side walls and the other one for the ridges (Figure 4.4). The aligned stacking of multiple layers of negative photoresists forms the microfluidic channel. SU-8, a negative photoresist is used to make the molds because it offers superior geometric fidelity, high aspect ratio, and mechanical stability which are particularly suitable for making reusable molds.

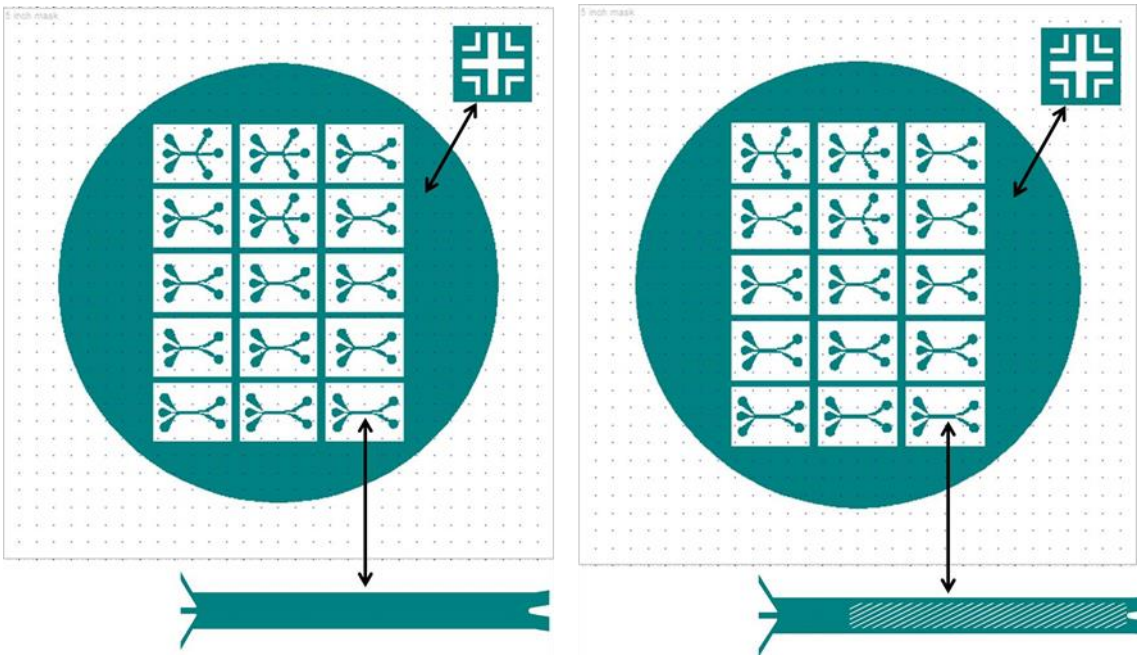

Figure 4.4. Two photolithographic mask designs are used to make multi-layered structures on a silicon wafer. The mask design on the left forms side wall and gap size of the microfluidic cell sorter and the design on the right form the ridges inside the microfluidic cell sorter. The alignment marks are made on both sides of the features so that multiple layers of photoresist can be aligned and exposed using a mask aligner.

The process flow for fabrication of microfluidic cell sorter is shown in Figure 4.5a. The microfluidic channels were made by replica molding PDMS (Sylgard 184 Dow Corning Corp)

on the permanent mold. PDMS is a clear polymer that is biocompatible and permeable to oxygen which makes it a great candidate to construct microfluidic devices for handling biological cells. Uncured PDMS was mixed in a 10:1 ratio of elastomer to curing agent, then poured onto the SU-8 mold to a thickness of 0.5 cm and cured in an oven at 60 degree Celsius for 6 hours. SEM images of the molded PDMS cell sorter are shown in Figure 4.5b.

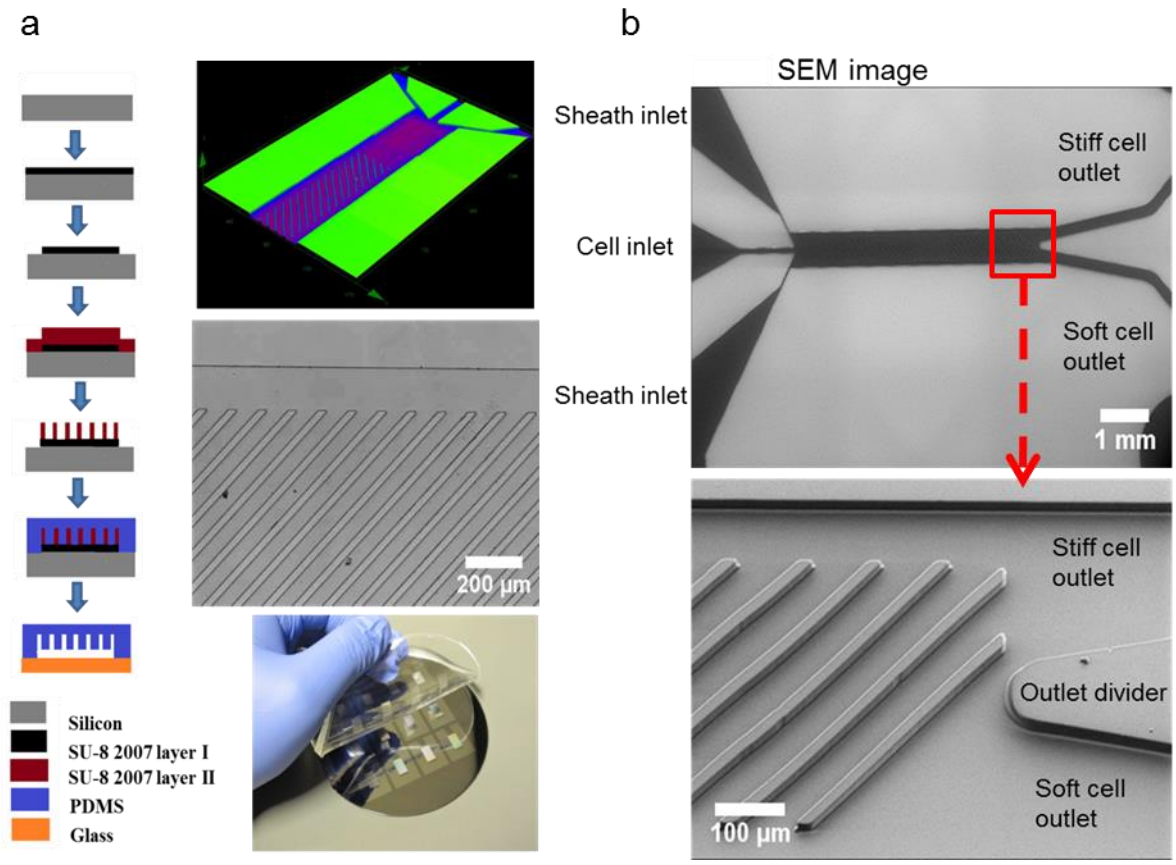

Figure 4.5. Microfluidic cell sorter fabrication. a) Process flow showing the fabrication of the microfluidic cell sorters. A confocal image of 3D laser scan of the microfluidic cell sorter. An optical microscopy image showing the slanted ridges. Cured PDMS device is peeled off a permanent mold. b) Scanning electron microscopy (SEM) images of the mold and PDMS microfluidic cell sorter.

The dimension of the gap layer is critical because it determines the compressive strain imposed on cells. Therefore, the gap layer thickness of the mold has to be checked by profilometry to ensure the accuracy. Further, other geometric dimensions of the microfluidic channel also need to be verified with a laser confocal microscope (Olympus LEXT) to guarantee the accuracy (Figure 4.6).

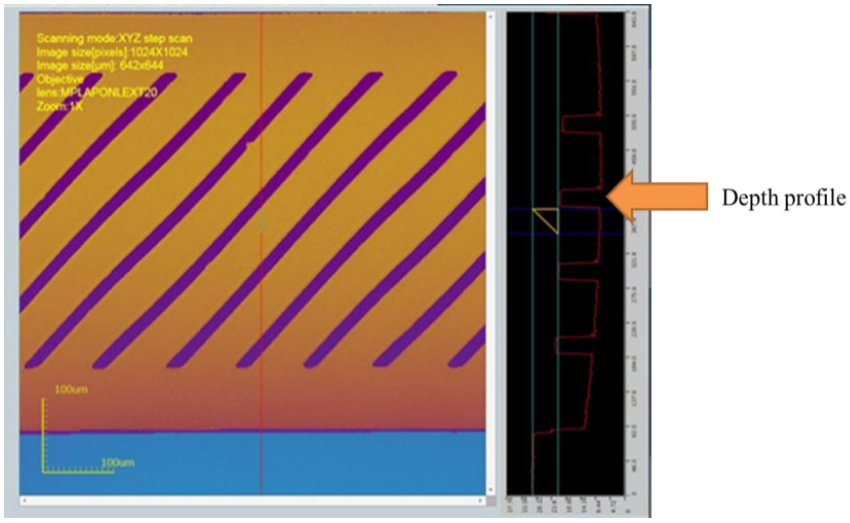

Figure 4.6. Measurement of the cross-section of the microfluidic cell sorter using profilometry. The ridge profile is generated by a 3D laser confocal microscope (Olympus LEXT 3D). The ridge height, gap size and channel dimension can be measured.

After the cured PDMS layer is peeled off the mold and inlet and outlet holes are punched with 1 mm biopsy punch. The PDMS channel is treated with oxygen plasma (Harrick plasma cleaner PDS 32G) for 2 minutes then bond to a glass slide. The plasma oxidizes the surface of PDMS temporarily so that it can be bonded to glass substrate forming leak-tight microfluidic channels. An example of a finished microfluidic cell sorter is shown in Figure 4.7.

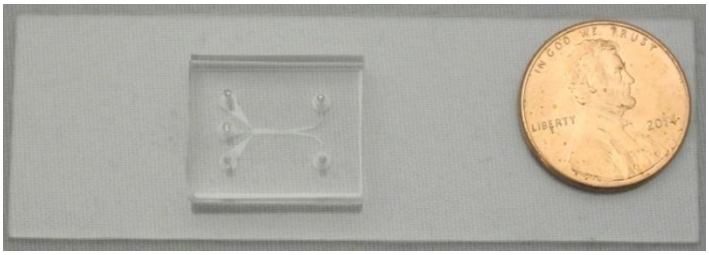

Figure 4.7. An image of the microfluidic cell sorter.

The interconnects are used to transport cells by connecting the microfluidic channel to the syringes containing cells and focusing fluids. The key performance measure is the ability to withstand applied pressure. A flat-head metal pin is pressure fitted into the inlet hole on the PDMS channel and the other end is boned to a polystyrene tube by epoxy. A luer-lock flat-head needle is attached the other end of the polystyrene tube. The use of luer-lock needle helps to connect syringes to the polystyrene tube and provide stability during fluid infusion. The metal pins offer stability and consistent performance by locking onto the cell sorter through pressure fitting.

The essential equipment to operate, record and analyze cell sorting includes the microfluidic cell sorter, syringe pumps, an inverted microscope, a high-speed camera and a computer (Figure 4.8). Syringe pumps (PHD 2000 Harvard Apparatus) are used to control the flow rates for the experiment. Cells inside the cell media are contained in a syringe and infused into the microfluidic device through polyethylene tubes. The cells flowing inside the microfluidic device are visualized with an inverted optical microscope (Nikon Eclipse Ti) and the high-speed videos are recorded using a high-speed camera (Phantom v7.3 Vision Research). In order to accurately capture the cell trajectories, we operate the high-speed camera at a

minimum of 2000 frames per second with a minimum resolution of 640 by 480 pixels for all videos and images. Sorted cells are continuously collected at the outlets.

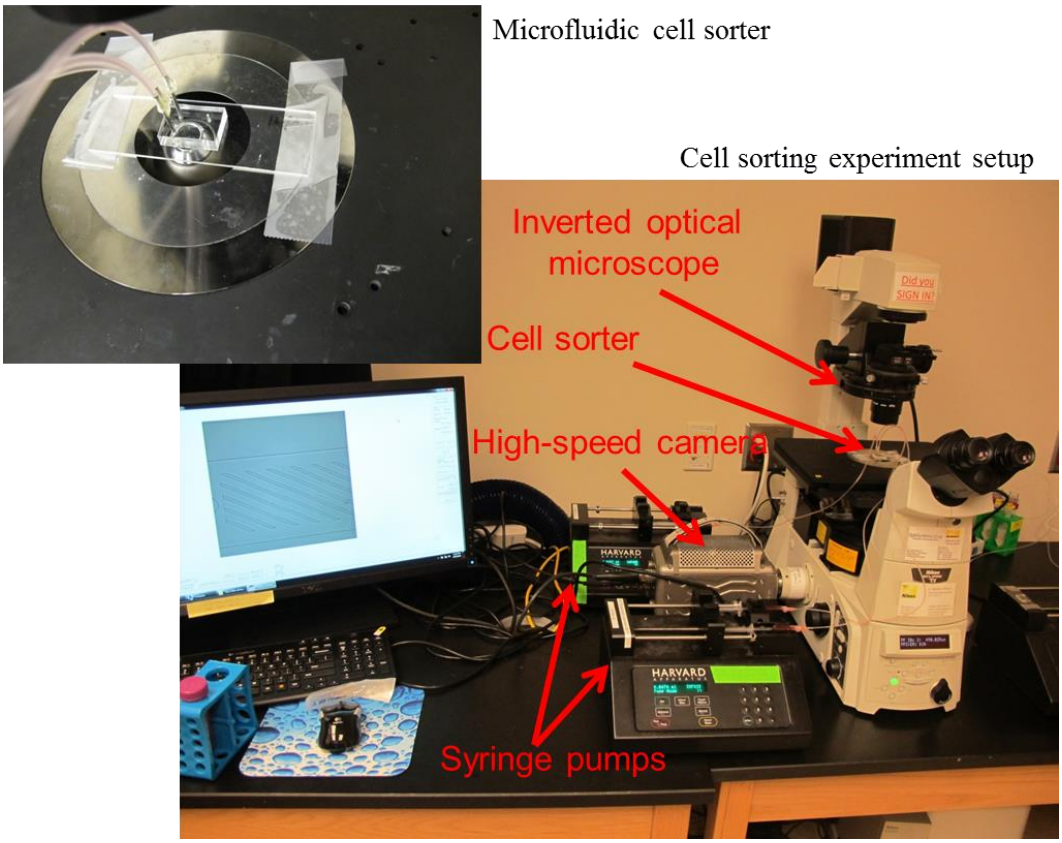

Figure 4.8. Cell sorting experiment setup. The microfluidic cell sorter is mounted on an inverted microscope. The cell mixture is infused into the sorter via capillary tubes. The pumping of fluid is done by syringe pumps which control the flow rate and applied pressure. A high-speed camera is used to record cell sorting process in real-time.

Cell surface proteins can cause undesired adhesion to the channel side walls and ridges. Nonspecific adhesions can lead to disruption of cell trajectory and channel clogging. To prevent cell adhesion, bovine serum albumin (BSA) is dissolved in DPBS at concentration of 10 mg/mL and the solution is infused into the channel and the treated channel is stored at 4 degree Celsius overnight (Figure 4.9). The BSA is a protein that effectively prevents nonspecific adhesion by protein adsorption[6,7]. Most of the primary cells and stem cells are highly “sticky”, not only do

they tend to adhere to the channel, but also to each other. In addition to BSA treatment, 0.01% Tween (a surfactant) can be added to cell solution and focusing fluid to further reduce adhesion.

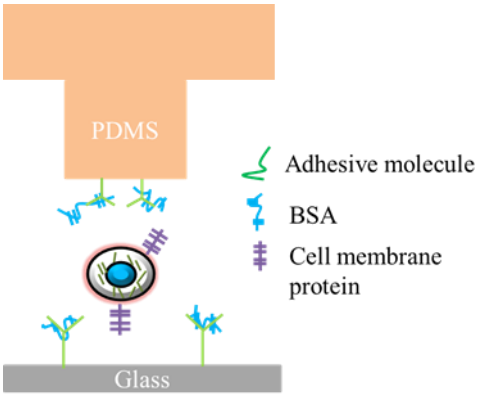

Figure 4.9. Chemical treatment of microfluidic channel surface. The microfluidic channel surface is coated with bovine serum albumin to prevent non-specific cell adhesion to the ridge and channel walls.

4.2 Effect of Channel Geometric and Flow Parameters

The design of the microfluidic cell sorters is an iterative process that employs computational fluid dynamics simulations as guide. To accurately engineer the fluidic dynamics within the microfluidic channels and save time and costs, numerical simulations are used to optimize the channel geometry prior to the fabrication of the microfluidic cell sorter. The purpose of the simulation is to ensure cell focusing and avoid sudden velocity changes which can lead to cell stagnation and channel clogging. Ansys Fluent, a commercially available fluid dynamics simulation software package, is used to conduct flow simulations.

The cell sorter has three inlets and two outlets. The cell sample fluid stream enters the cell sorter at the center inlet which is pinched by two focusing streams on each side. Sheath focusing is frequently employed in the microfluidic devices. The focusing is achieved through

two sheath flows that pinch sample flow in the middle. When the applied pressure is fixed, the angles, β, formed by the principal axes of the inlets and channel, the width of the inlets and the width of the channel control the focusing (Figure 4.10). The cell focusing is essential in cell sorting because cells should converge into a thin stream to begin the sorting procedure at the same starting point. Otherwise, the variable initial conditions will reduce the cell separation performance since some cells will have to travel "extra" distances to their designated outlets and in some cases may end in the "wrong" outlet.

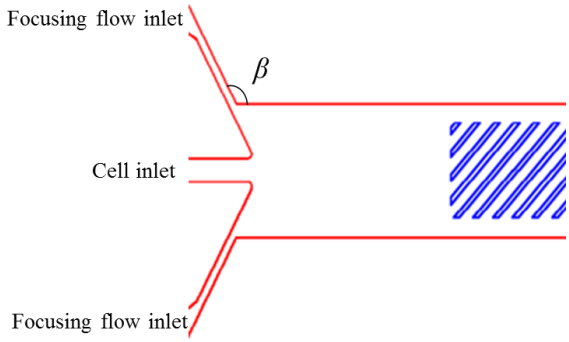

Figure 4.10. Channel inlet design parameters. The microfluidic cell sorter uses three inlets. The channel flow rate is the sum of all three input streams. Cells enter the device through the center inlet and are focused by two focusing streams from both sides. The angle, β, of the focusing stream to the cell inlet stream partially determines the performance of focusing.

The width of the sheath flow inlets was determined through iterations of hydrodynamic modeling (Figure 4.11). Although the narrow sheath flow inlets achieved better focusing and eliminated sudden velocity changes near the cell inlet, the sheath flow inlets should not be smaller than 50 μm, because it may incur clogging. The angles, β, formed between the principal axes of the inlets and channel were also determined through iterative modeling (Figure 4.11a). The angle was varied from 90 degrees to 150 degrees. At 90 degrees, the T-junction could not provide enough focusing for cells to reach the first ridge and the streamlines quickly dispersed. As the angles gradually increased the focusing effect lasted longer but stagnation and back

circulation started to emerge near the cell inlet (Figure 4.11a). The solution was to remove straight edges of the inlet stream dividers and replace them with rounded fillets. Figure 4.11b shows an example of simulated fluid flow in terms of vector velocity and pathlines. Clearly, the focusing is long lasting while the undesired stagnation and back circulation are avoided.

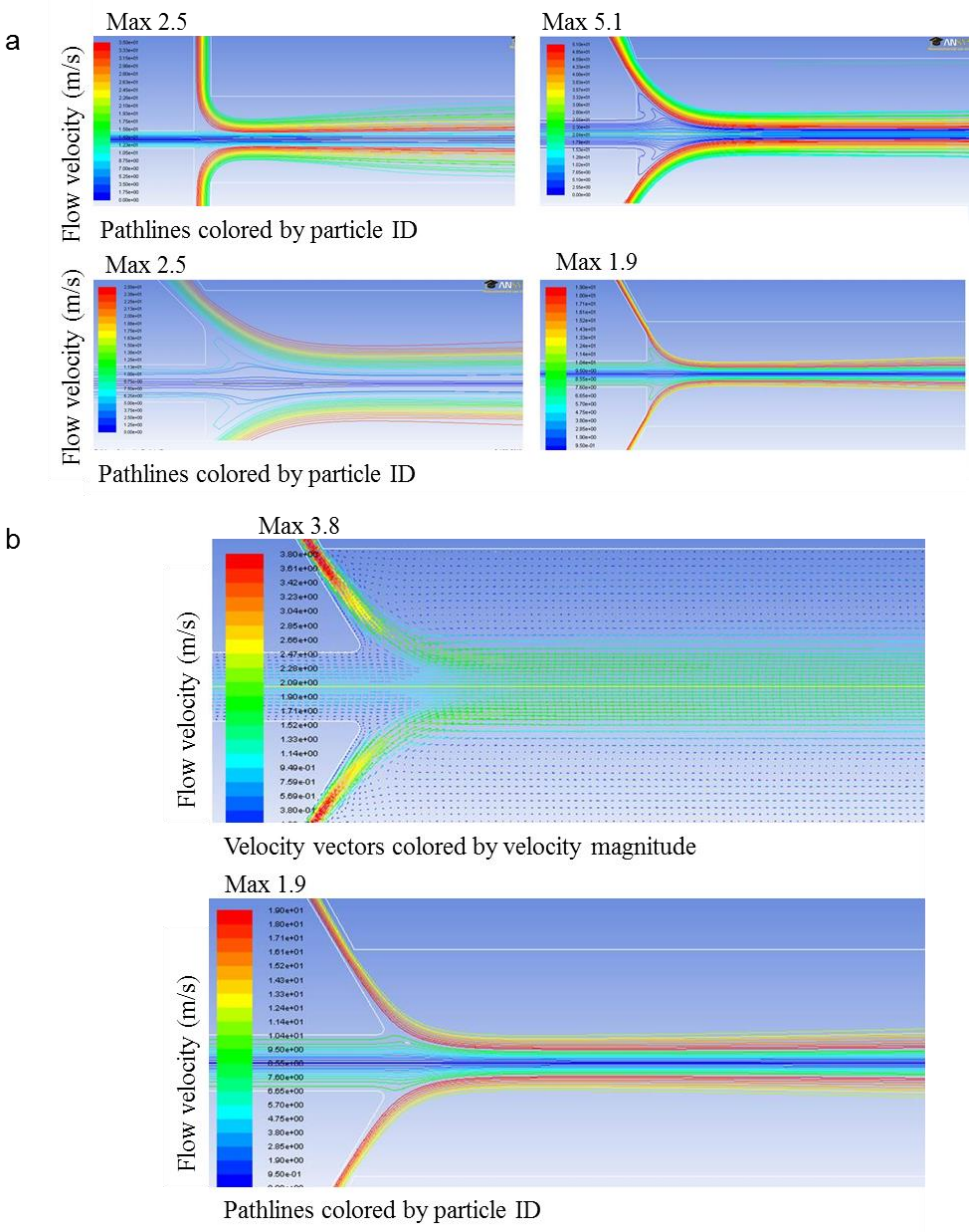

Figure 4.11. Computational fluid dynamics simulations of microfluidic channel hydrodynamics. a) Numerical fluid dynamic simulations showing inlet fluid stream pathlines for different channel

designs and input pressures. b) The optimized channel designs were found through iterations shown in a).

As previously stated, the design of microfluidic cell sorter is an iterative process based both on the results from numerical simulation as well as data collected from cell sorting experiment. As a result, several different designs have been tested. Figure 4.12 shows four different microfluidic cell sorter designs. The channel length, width, hydraulic diameter and pressure difference between inlet and outlet are also listed for each design. In particular, the 4th design in Figure 4.12 has several variants in the ridge dimension, spacing, channel length and outlet shapes (Figure 4.13). These geometric parameters constitute important design considerations due to the substantial impact on cell trajectory. For instance, the spacing between adjacent ridges controls the cell relaxation time interval and the ridge angle affects the hydrodynamics of the flow.

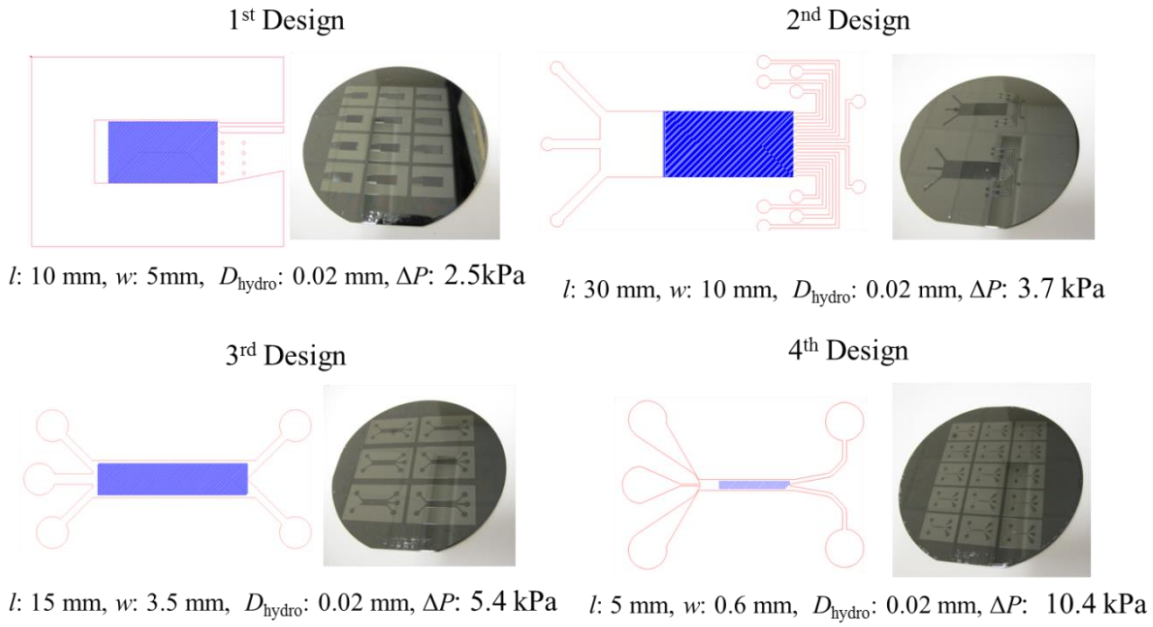

Figure 4.12. Four Different designs or microfluidic cell sorters. For each design, an AutoCAD draft is shown on the left and a wafer mold is shown on the right. The channel dimensions and pressure difference between inlet and outlet are given below each design.

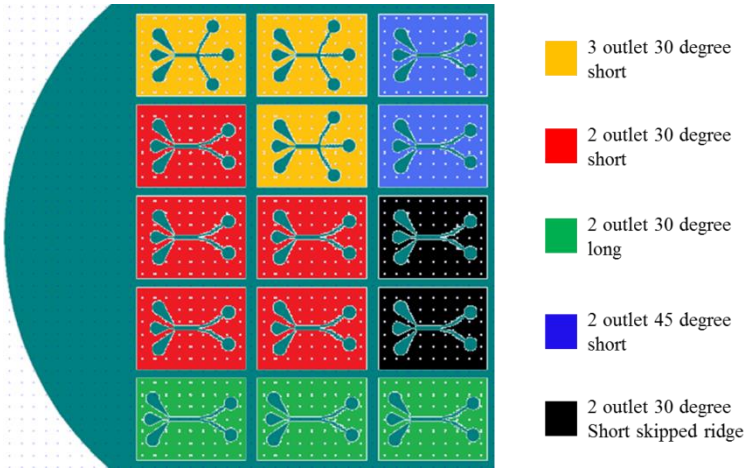

Figure 4.13. The 4th design of the microfluidic cell sorters have five variants. The effects of different geometric parameters such as ridge angle, and ridge spacing on cell sorting are investigated through these channels.

The sorted cells are continuously collected at the outlets. To prevent the biasing of liquid volume output between two outlets, the outlet length is elongated through iterations to increase hydrodynamic resistance. In addition, a serpentine configuration is used to further improve hydrodynamic resistance (Figure 4.14). This design feature ensured that the both outlets have equal amount of liquid exiting, therefore it eliminates flow biasing at the outlet.

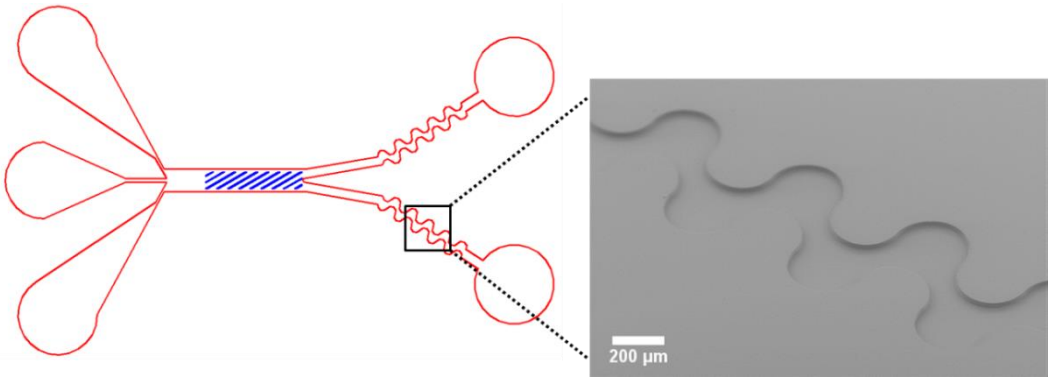

Figure 4.14. Serpentine outlets are used to prevent channel flow biasing by increasing the flow resistance between the inlet and outlet of the channel.

The ridge dimensions have the most profound impact on the hydrodynamics of the channel and cell separation outcome. Cell trajectory depends on the interactions between the cell and the slanted ridges. The ridges apply periodic compressions that probe the cell biophysical properties. The ridge dimensions that are examined in detail include: gap height, ridge spacing, ridge angle as well as the number of ridges.

The gap distance, *h*, (Figure 4.15) between the ridge and bottom substrate surface controls the magnitude of compressive strain applied to the cells. The trajectory of cells in the microfluidic device is strongly affected by the size of the gap. The selection of the gap size depends on biophysical properties of the cells to be separated. For instance, the microfluidic channel with a large gap does not impose sufficient constriction, which leads to small divergent lateral displacement per ridge. On the other hand, if the gap is too small, it can cause cell clogging, resulting in lysing, trapping, and eventual channel occlusion. In this case, the cells either roll along the ridges or become trapped underneath the ridges.

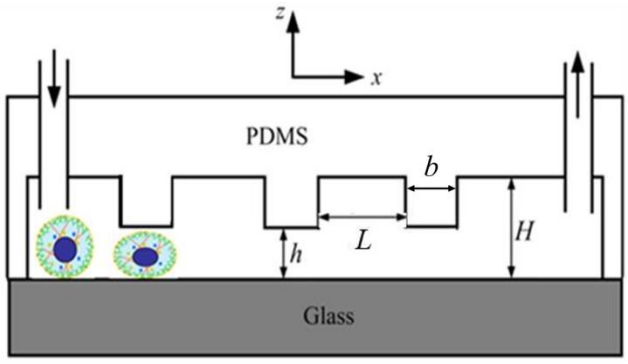

Figure 4.15. Side view sketch of the microfluidic cell sorter. The gap size, *h*, is formed between PDMS ridge and glass substrate. The right spacing. *L*, is the distance between sequential ridges. *L* is uniform throughout the channel. The ridge width is *b* and channel height is *H*.

To illustrate the impact of gap size on the cell trajectory, K562 cells were used to test five different gap sizes (Figure 4.16). Cell trajectories were recorded using high-speed microscopy.

At 6 μm gap size, K562 cells were seen undergoing large positive displacement in the direction parallel to the ridges. Significant cell lysing and cell trapping were observed. Cells trajectories were strongly affected because cells need to go around the obstacles. This created large spread for the cell trajectory. The broken cell membrane and the intercellular organelles released from cell lysing acted like glues that disrupted the paths of other migrating cells. The buildup of the trapped cells eventually led to channel occlusion. As the gap gradually relaxed, the positive displacement was reduced and cells could pass through the channel without any lysing or trapping. The spread in the cell trajectory was also lowered. When the gap size was comparable to the average diameter of the cell population cells, the lateral displacement was slightly positive.

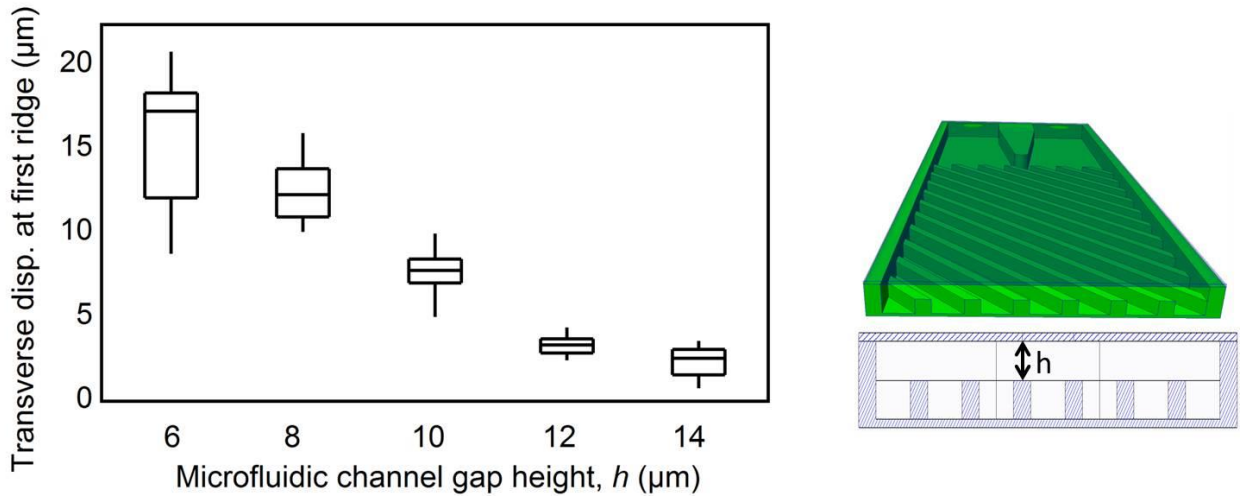

Figure 4.16. Effect of gap size, *h*, on cell lateral displacement. K562 cell lateral displacement at the first ridge. The lateral displacement decrease as the gap size, *h*, is enlarged.

Ridge spacing, *L*, and ridge width, *b*, affect the cell trajectory (Figure 4.17a) as well as the magnitude of the secondary flow (Figure 4.17b). The ridge width is selected to be 20 μm which is slightly larger compared to the diameters of most of the cell types that are separated. The comparable size allows the cells to be completely compressed instead of locally. Lynn *et al.* summarized the effect of ridge width and spacing in Figure 4.17b[8]. The strongest circulation is

approximately at L = 50 μm. Therefore the initial design of the ridge spacing is selected to be 50 μm. However, later in the study, the ridge spacing is increased, because the ridge spacing has profound effect on cell relaxation which is the key to separation of cells based on viscoelasticity.

The ridge angle, α, also plays an important role in cell separation. However, from the simulation result, the effect is negligible when cell elastic modulus is below 1 kPa which include the majority of the cells that are separated (Figure 4.17a). As a result, the initial design of the ridge is 45 degrees. However, in cell separation by viscosity experiment, it is clear that ridge angle at 45 degrees does yield best separation. For example, when the ridge angle is more aligned with the channel axis (smaller α), it is easier for the less viscous cells to "roll" on the ridges at the leading edge.

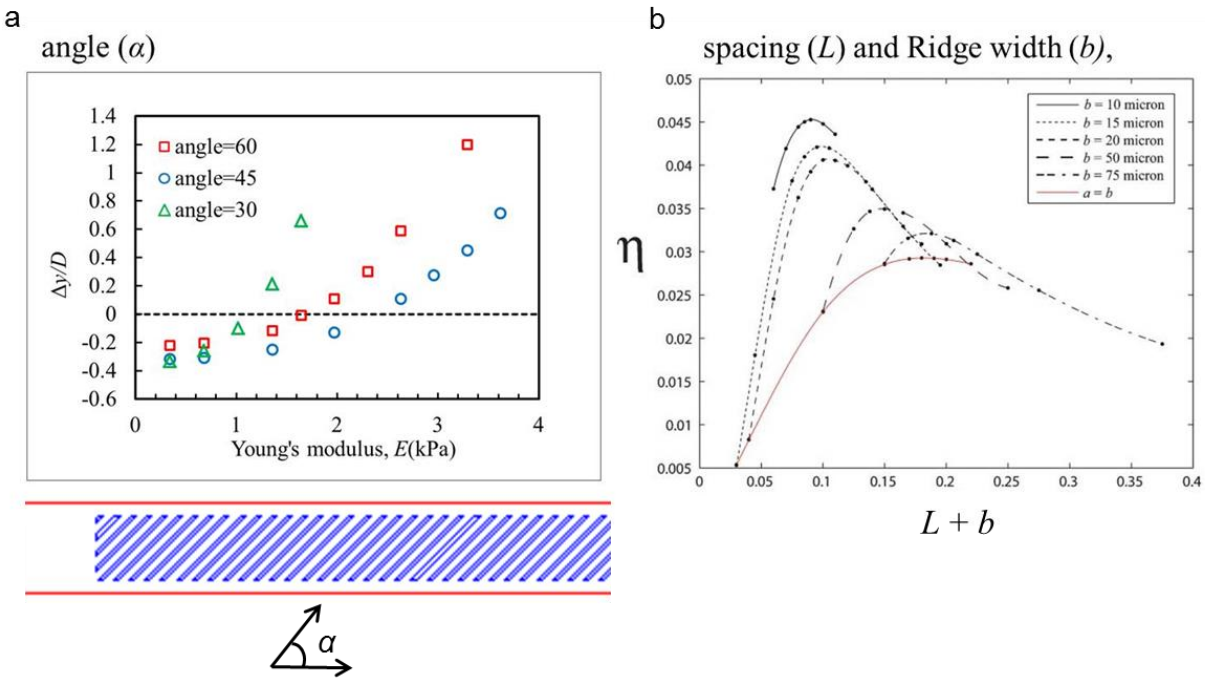

Figure 4.17. Effect of ridge angle, ridge spacing and ridge width in cell trajectory. a) Numerical simulation of cell lateral displacement as a function of cell Young's modulus for 3 different ridge angles. b) Numerical simulation of strength of circulation as a function of ridge spacing, L, and ridge width, b. Graph adapted from reference[8]

Ridge spacing, *L*, is important in cell sorting by viscosity. Increasing the ridge spacing resulted in increased relaxation of elastic cells, which we can utilize to separate cells viscoelastically. We measured the cell relaxation by recording the apparent diameter of the compressed cells between first ridge and second ridge in a 9 μm gap channel (h = 9 μm, L=100 μm and 200 μm) for both weakly viscous K562 and highly viscous HL60 cells. The cell relaxation intervals and trajectories are schematically shown in Figure 4.18a and 4.18b. In both cases, the weakly viscous K562 cells relaxed more quickly than HL60 cells (Figure 4.18c and 4.18d). In addition, the increased ridge spacing allowed both cell types longer durations to relax between compressions (Figure 4.18d), which amplified the difference in relaxation between the K562 and HL60 cells (Fig. 4.18e). The additional relaxation resulted from changing the ridge spacing from L = 100 μm to 200 μm is schematically shown for K562 cells in Figure 4.18e. Also, we observed that the additional relaxation increased K562 cell lateral displacement but less significant for HL60 cells (Fig. 4.18e). Therefore the increased ridge spacing did not result in appreciable cell relaxation of the highly viscous HL60 cells. As a result, the increased ridge spacing enhanced the divergence of lateral displacement between K562 and HL60 cells.

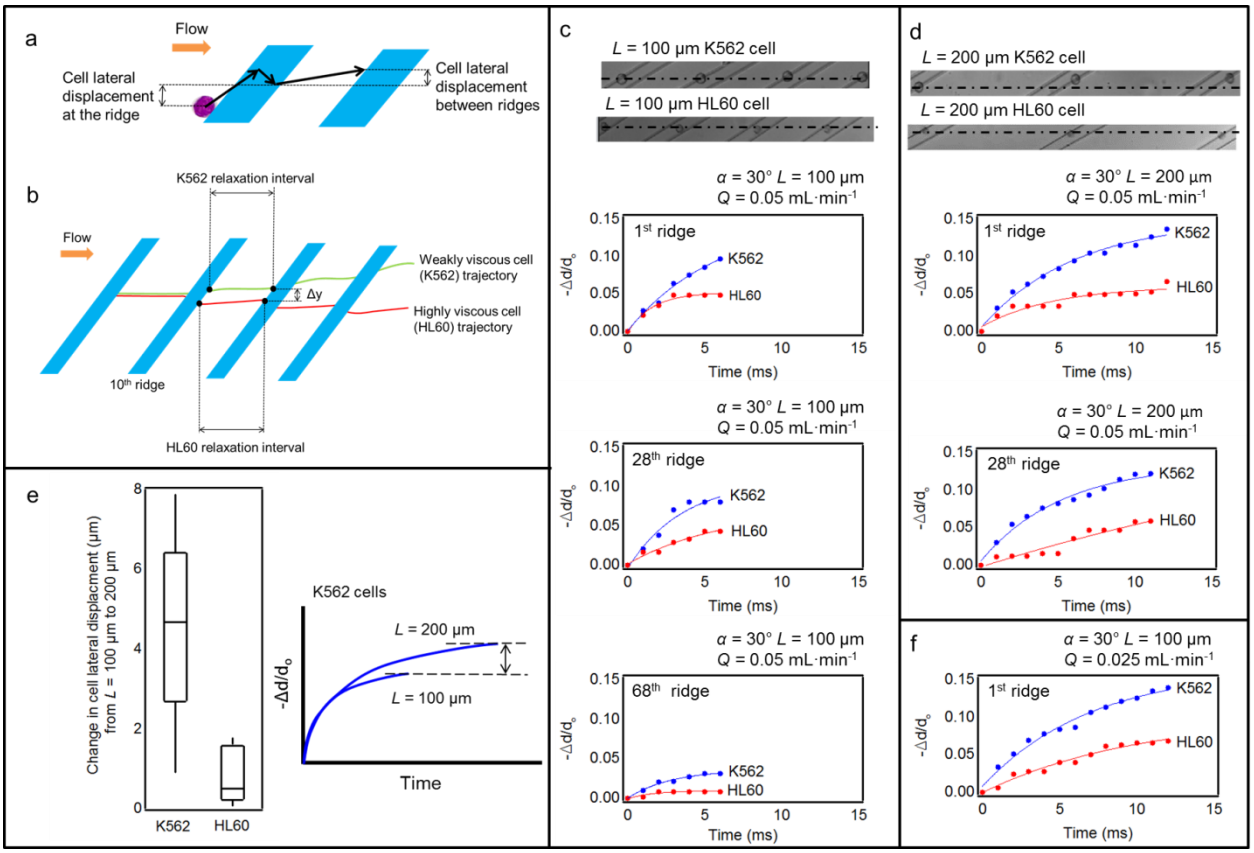

Figure 4.18. Cell separation based on different rates of relaxation. a) Cell trajectory is composed of two segments: lateral displacement at the ridge and lateral displacement between the ridges. Cell biophysical properties control the displacement at the ridge. For example, big, elastic and stiff cells move along the leading edge of the ridge and small soft and viscous cells move perpendicular to the ridge. In between the ridges, cell displacement is controlled by the strength of flow circulation induced by the ridges. The lateral displacement is always positive. b) K562 is bigger and more elastic than HL60 cells. Therefore, K562 cells have positive lateral displacement at the first ridge and HL60 cells have negative lateral displacement. Cell relaxation was measured immediately after cells completely exit the first ridge and before touching the second ridge. c) Cells relaxation show different size recovery after leaving the first ridge and before reaching the second ridge. The y-axis represents the change in cell diameter due to relaxation after initial compression at the first ridge. The data points were fitted with exponential trend lines. The cell diameter recovery due to relaxation was recoded different locations of each channel. In all channel designs, K562 cells relaxed faster than HL60 between ridge compressions. d) and e) The larger spacing between ridges (L = 200 μm) allowed K562 cells to relax more than HL60. However, after prolonged compressions (68th ridge) both K562 and HL60 significantly lost their ability to recover. f) When channel flow rate was reduced by half to Q = 0.025 mL·min^{-1}, cell relaxation in the smaller ridge spacing channel (L = 100 μm) was similar to

larger ridge spacing channel (L = 200 μm) at Q = 0.050 mL·min^{-1}. d) The enlarged ridge spacing allowed K562 cells to recover more but less significantly for highly viscous HL60 cells.

We initially anticipated that the number of ridges would correlate with increased differential cell separation by amplifying the pairwise separation. We observed this strategy faced limitations due to the dynamic and viscoelastic behavior of cells. For both K562 and HL60 cells, we observed repeated compressions resulted in negative lateral displacement after approximately 10 ridges (Table 4.1). We hypothesize that after repeated compression, the cellular components respond to become more viscous[9]. The viscoelastic response can be modelled using the standard linear solid model where one spring is connected to a spring-and-damper in parallel. We observe cell viscous properties to be different after repeated compressions. For example, in Table 1, the cell lateral displacement at first compression is different compared to at the 10th compression which is also different at the 68th compression. Therefore, we can describe cell relaxation as a time-dependent dynamic response to the periodic compressions.

Table 4.1. Lateral displacement for K562 cells, HL60 cells and 7.5 μm particles are listed for different channel designs. Unlike particles, cell trajectories change at different locations of the microfluidic channel.

K562 Cell Lateral Displacement Per Ridge (μm)					
Channel Design	1st ridge	10th ridge	28th ridge	68th ridge	between ridge
30 Degree Ridge (*L* =100 μm)	0.89±0.23	-6.04±2.80	-6.08±2.86	-7.95±2.58	7.42±1.36
45 Degree Ridge (*L* =78μm)	0.31±0.067	-5.88±2.74	-5.94±2.60	N/A	7.08±1.29
30 Degree Ridge (*L* =200 μm)	0.91±0.34	-3.56±2.31	-5.61±2.41	N/A	10.1±0.9
HL60 Cell Lateral Displacement Per Ridge (μm)					
Channel Design	1st ridge	10th ridge	28th ridge	68th ridge	between ridge
30 Degree Ridge (*L* =100 μm)	-4.03±0.94	-11.1±2.44	-11.4±1.83	-12.1±1.58	7.87±0.62
45 Degree Ridge (*L* =78μm)	-4.08±0.68	-10.82±1.63	-11.2±1.48	N/A	7.52±0.54
30 Degree Ridge (*L* =200 μm)	-4.11±1.75	--11.2±2.91	-11.6±2.01	N/A	11.1±0.51

7.5 μm Particle Lateral Displacement Per Ridge (μm)		
Channel Design	ridge	between ridge
30 Degree Ridge (*L* =100 μm)	-12.0±0.79	10.4±1.05
45 Degree Ridge (*L* =78μm)	-13.3±1.15	12.4±1.82
30 Degree Ridge (*L* =200 μm)	-14.7±1.61	14.1±2.52

The effects of ridge angle, ridge spacing and number of ridges on cell lateral displacements for HL60 and K562 are summarized in Table 1. In addition the lateral displacement of micro-particles having diameter of 7.5 μm is also displayed. It is evident that in sorting weakly viscous cells from highly viscous cells, ridge spacing played a vital role.

In summary, the design of microfluidic channel geometry depends on the biophysical properties of the pair of cells to be separated. Figure 4.19 shows a cell trajectory model for different cell types in a gap size h = 9 μm microfluidic cell sorter. From the cell trajectory model, we can predict cell separation results. For example, if we want to separate HL60 cell from HeyA8 cells we know it is likely to succeed because the majority of the HL60 cells have negative lateral displacement while HeyA8 cells have positive lateral displacement. On the other

hand, we can predict that it is unlikely to separate Hey from HeyA8 cells in the h = 9 μm device because both cells have positive lateral displacement.

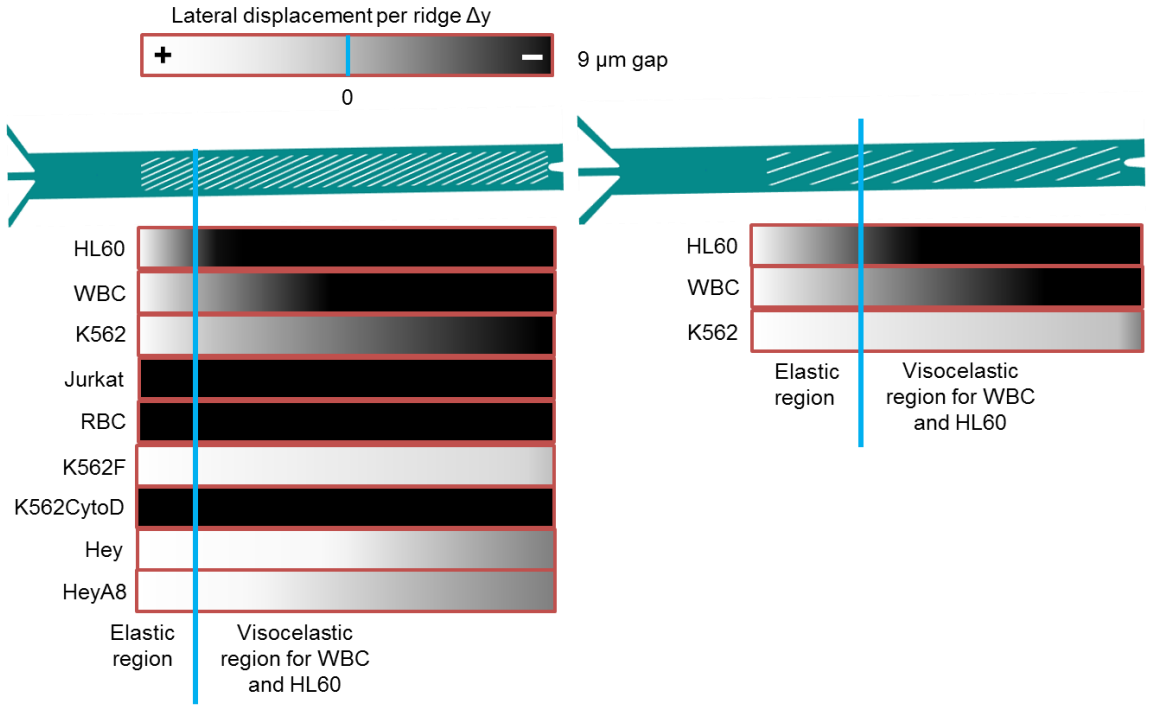

Figure 4.19. Cell trajectory model. The lateral displacement per ridge is positive in the white region and negative in the black region. K562, WBC and HL60 cell trajectory changes during the course of repeated compressions.

4.3 Effect of Flow Rate, Focusing, and Biasing

The flow rate influences cell separation through the strength of secondary flow and length of time interval that cells travel between ridges. The channel flow rate is the sum of three streams: two sheath streams and one cell sample stream. The rise in channel flow rate increases the hydrodynamic (viscous drag) force which is a product of secondary flow induced by the ridges. In chapter three, it is explained that cell trajectory is a function of the net force between the elastic force and hydrodynamic force. A numerically simulated soft cell trajectory is shown

in Figure 4.20 (marked as black arrow). Therefore, cells undergoing high flow rates tend to migrate in the direction perpendicular to the ridges.

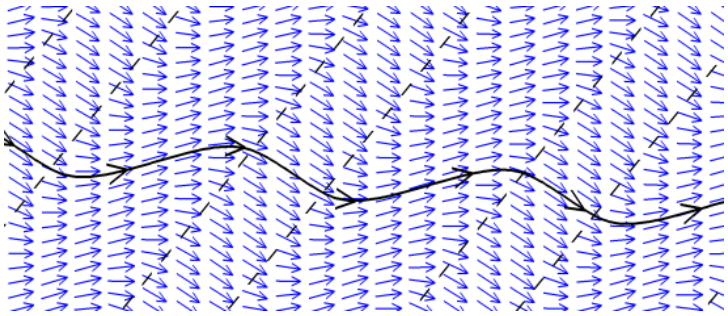

Figure 4.20. Simulation of fluid dynamics inside a microfluidic channel. The fluid velocity vectors are marked by blue arrow and soft cell trajectory is marked by a black arrow. The simulation is for flow at the middle of the channel and the cell trajectory is seen after the cell reaches the steady state.

The ratio of the sheath flow rates to the sample flow rates also has significant effect on cell separation. First, the strength of focusing depends on the ratios of sheath flow to the cell sample flow. The higher multiple of sheath to sample flow provides better cell focusing. However, when increasing sheath flow to sample flow ratio, the channel flow rate also changes since it is the sum of all three streams. Through numerical simulation, we determine that the optimal focusing is achieved when sheath flow is twice of that sample flow (Figure 4.11b).

The use of sheath focusing not only allows cells to be focused onto a single point to begin separation, but also gives the flexibility to choose that initial point in the lateral direction. The biasing caused by the two sheath flows also dictates the location of initial compression. For cell types that have similar biophysical properties the choice of starting point is crucial to achieve the separation. For instance, cell A is only slightly stiffer than cell B such that both cell types tend to be more affected by the hydrodynamic force. Then, the starting point can be set closer to the stiff

cell outlet such that cell A would need less “travelling” to reach the designated outlet. In this example, the biasing is achieved by raising the sheath flow rate on the soft outlet side and lowering the stiff outlet side (Figure 4.21). As a result, the cell sample stream is off-centered and the cell probing begins closer to the stiff cell outlet side. This arrangement was successfully applied in several cell separation experiments, particularly when the two cell types were soft.

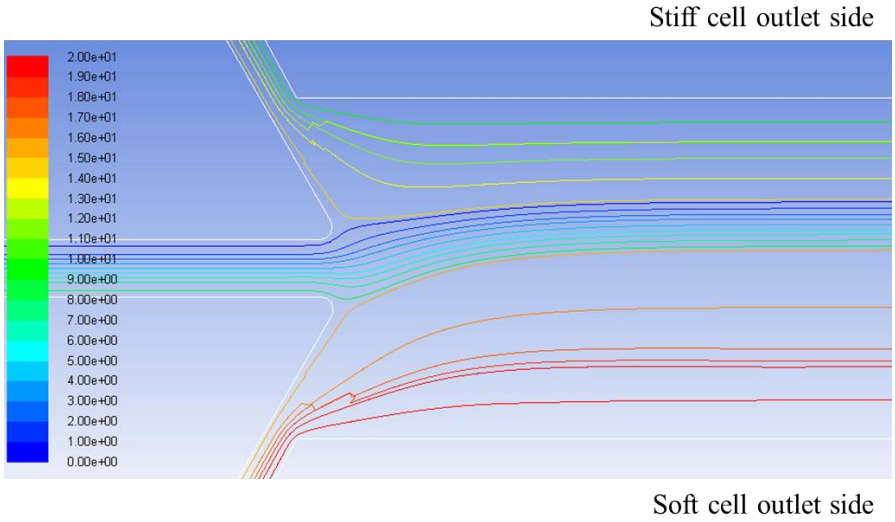

Figure 4.21. Numerical simulations showing asymmetric pathlines at the channel inlets due to focusing stream biasing.

To summarize, the use of sheath focusing provide the cell focusing and fine-tuning of the initial condition. For cells that have overlapping biophysical properties, biasing can help to improve cell separation without the use of a different microfluidic channel design. The flow rate also contributes to the throughput of the analysis. The maximum flow rate is limited by the balance between the magnitude of secondary flow, the time between sequential compression and the biophysical properties of the cells.

4.4 References

1. Duffy DC, McDonald JC, Schueller OJA, Whitesides GM (1998) Rapid prototyping of microfluidic systems in poly(dimethylsiloxane). Analytical Chemistry 70: 4974-4984.
2. Xia YN, Whitesides GM (1998) Soft lithography. Annual Review of Materials Science 28: 153-184.
3. McDonald JC, Duffy DC, Anderson JR, Chiu DT, Wu HK, et al. (2000) Fabrication of microfluidic systems in poly(dimethylsiloxane). Electrophoresis 21: 27-40.
4. Muck A, Wang J, Jacobs M, Chen G, Chatrathi MP, et al. (2004) Fabrication of poly(methyl methacrylate) microfluidic chips by atmospheric molding. Analytical Chemistry 76: 2290-2297.
5. Whitesides GM, Ostuni E, Takayama S, Jiang XY, Ingber DE (2001) Soft lithography in biology and biochemistry. Annual Review of Biomedical Engineering 3: 335-373.
6. Wong I, Ho CM (2009) Surface molecular property modifications for poly(dimethylsiloxane) (PDMS) based microfluidic devices. Microfluidics and Nanofluidics 7: 291-306.
7. Fan DH, Yuan SW, Shen YM (2010) Surface modification with BSA blocking based on in situ synthesized gold nanoparticles in poly(dimethylsiloxane) microchip. Colloids and Surfaces B-Biointerfaces 75: 608-611.
8. Lynn NS, Dandy DS (2007) Geometrical optimization of helical flow in grooved micromixers. Lab on a Chip 7: 580-587.
9. Mak M, Erickson D (2013) A serial micropipette microfluidic device with applications to cancer cell repeated deformation studies. Integrative Biology 5: 1374-1384.

CHAPTER 5

MICROFLUIDIC CELL SEPARATION USING SIZE, STIFFNESS AND VISCOSITY

In chapter 5, we show the results of cell sorting using the microfluidic cell sorters. The chapter is divided into three sections, each demonstrates cell sorting by cell stiffness, cell size and cell viscosity respectively. In addition, we discuss the limitations of the cell sorters through an example where the cell stiffness overlaps significantly with the difference in average Young's modulus less than 100 Pa. Furthermore, we discuss other important cell sorting considerations such as cell viability, and throughput.

5.1 Separation of Cells Based on Cell Stiffness

In this section, we demonstrate separation of cell populations which are of similar biophysical properties but of different stiffness. HeyA8 and Hey cell lines were chosen to simulate the presence of epithelial cancer cells mixed with similarly sized white blood cells (Jurkat and K562). The successful separations for these cell mixtures point to the potential for the device to be used in metastatic ovarian cancer cell enrichment for screening and monitoring.

In Chapter 3, K562 cells were treated with different concentrations of CytoD, an actin-depolymerizing drug, to create subpopulations that only differed in cell stiffness (Figure 5.1c). It was found that cell trajectory was a function of cell stiffness (Figure 5.1a and 5.1b). Therefore, we hypothesized that due to the differences in cell stiffness we could separate and sort cells. To

validate the hypothesis, K562 cells and 2 μM CytoD treated K562 cells were mixed and separated in a 8 μm gap cell sorter.

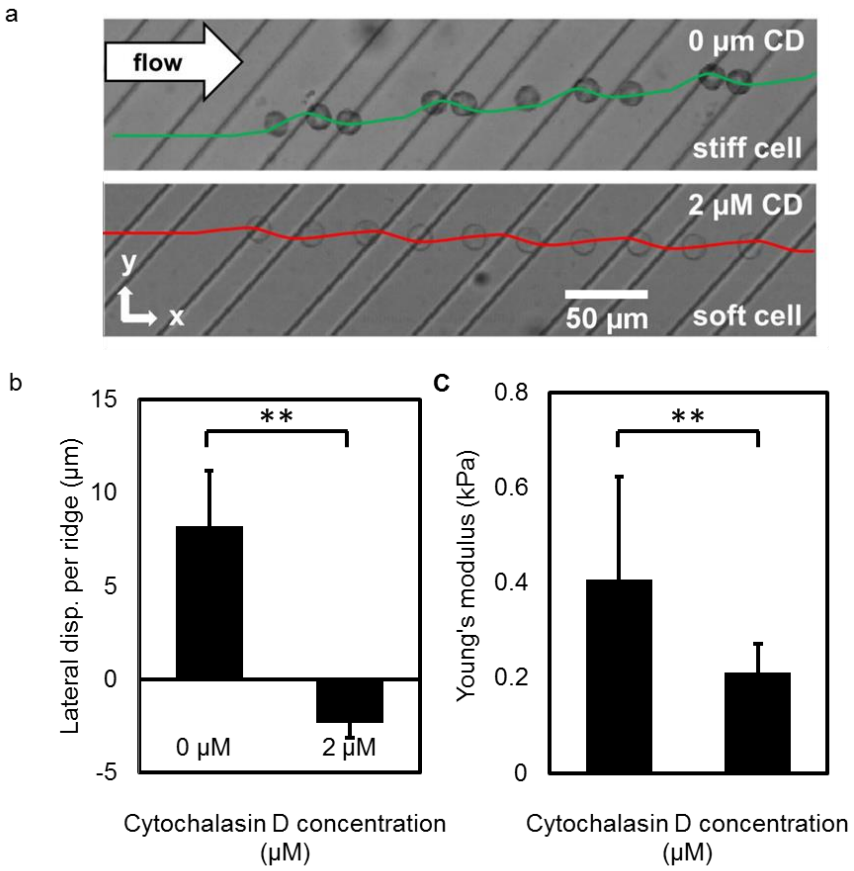

Figure 5.1. Cell trajectory and stiffness for K562 and 2 μM CytoD treated K562 cells. a) Overlay of still frames from a video of an untreated and 2 μM CytoD softened K562 cells flowing in a channel. Each micrograph is an overlay of 10 still frames at equal 10 ms time intervals from a video taken at 1200 fps. Green and red solid lines represent numerical simulations of the flow trajectory stiff and soft capsules. b) Cell lateral displacement per ridge (n = 100 for each cell population) for untreated K562 cells and 2 μM CytoD softened K562 cells are 8.20 ± 2.99 μm and -2.34 ± 0.76 μm respectively. c) Young's modulus (n = 37 for each cell population) for untreated K562 cells and 2 μM CytoD treated K562 cells are 0.40 ± 0.22 kPa and 0.21 ± 0.061 kPa respectively. The error bars represent the standard deviation. Nonparametric Wilcoxon signed-rank tests were used to test statistical significance between the two cell populations, with ** indicating a $p < 0.0001$.

To accurately measure and verify cell sorting specificity and throughput, cells were labelled with different colors of fluorescent lipid membrane stains. The cell mixtures at the inlet and outlets were analyzed with flow cytometric analysis (Figure 5.2). The proportions of two cell types at the inlet and outlets are represented by the percentages. To quantify cell enrichment at the outlets, we derive the cell enrichment factor (*c.e.f.*) which normalizes the separated cell populations with the initial cell mixture to obtain enrichment. As an example, the enrichment of K562 cells is computed as follows:

$$c.e.f._{K562} = \frac{(K562/CytoD\ K562)_{K562\ outlet}}{(K562/CytoD\ K562)_{initial\ mixture\ inlet}}$$

The enrichment factors for K562 cells and CytoD treated K562 cells are 3 and 1.8 fold respectively (Figure 5.2). Therefore, the three-fold enrichment of K562 cells at the outlet indicates the desired cell percentage is tripled at the output relative to the input.

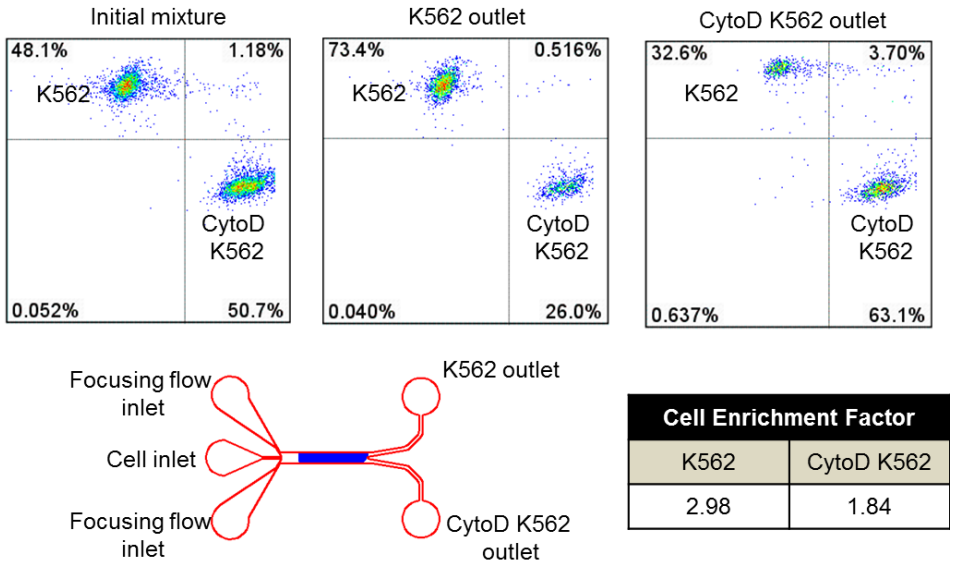

Cell Enrichment Factor	
K562	CytoD K562
2.98	1.84

Figure 5.2. Flow cytometric analysis of K562/CytoD K562 cell sorting. The quadrant gates segregate K562 and CytoD treated K562 cell populations in the second and fourth quadrants

respectively. Cell mixture before separation and sorted cells collected at the outlets were analyzed. The cell enrichment factors for K562 and CytoD treated K562 cells are 2.98 and 1.84 respectively.

To simulate a scenario of sorting metastatic cancer cells from blood cells, we selected HeyA8 and Jurkat as our cell models. HeyA8 is an epithelial-origin ovarian cancer cell line where as Jurkat is a lymphoblast leukemia cell line. Jurkat (E = 0.290 ± 0.11 kPa) and HeyA8 (E = 0.71 ± 0.53 kPa) cells were labeled fluorescently, mixed and streamed through the microfluidic cell sorter. Separated cells were collected at the outlets. The separation result was verified with flow cytometry analysis (Figure 5.3a). Cell enrichment was observed at both the stiff and soft outlets: 6.4-fold enrichment for HeyA8 cells and 2.6-fold enrichment for Jurkat cells. The cell stiffness, which was characterized by Young's modulus, of HeyA8 cells and Jurkat cells before the flow experiment were significantly different (Figure 5.3b) while being of similar size (Figure 5.3c). Due to the large natural variation of stiffness within the cell population, only partial collection of the stiff cells at the stiff outlet was observed. To confirm that the mixed cells were separated according to stiffness, additional flow experiments were performed with the mixed HeyA8 and Jurkat cells without any fluorescent labeling. Cells collected at the outlets were immediately measured with AFM and found to have significantly different stiffness values (Figure 5.3d). This result showed that similar sized cells from different cell lines can be separated into stiff and soft subpopulations.

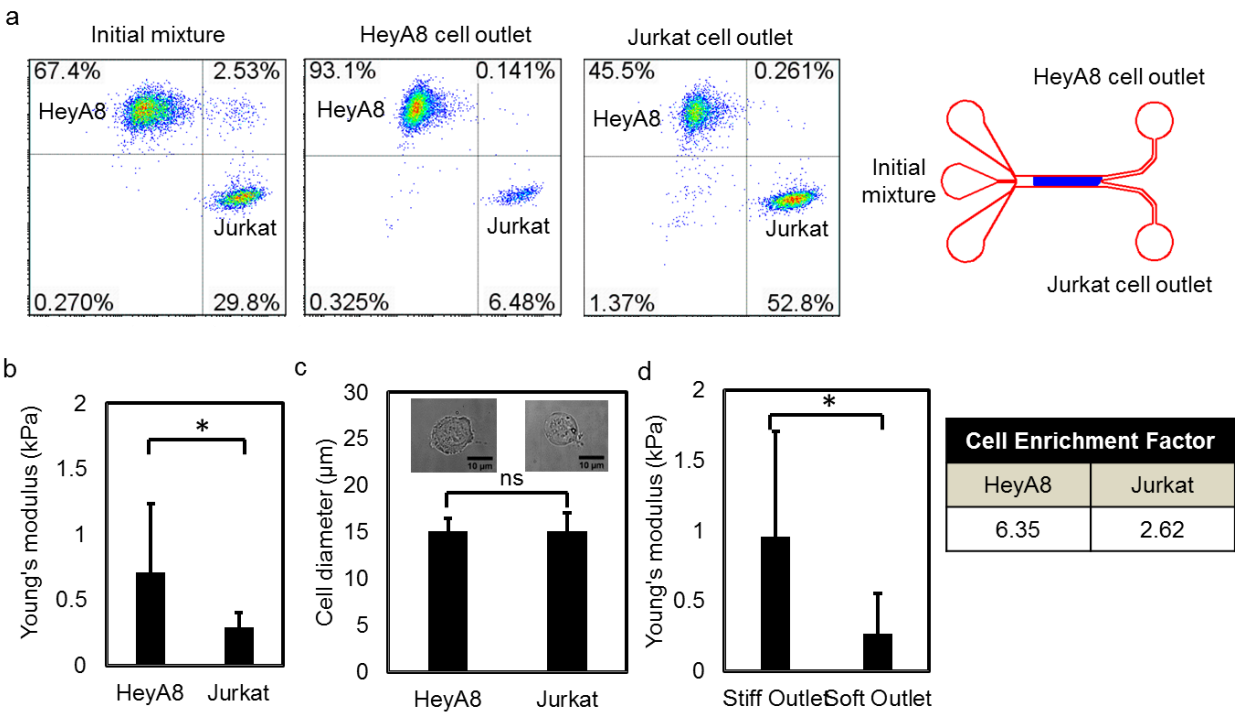

Cell Enrichment Factor	
HeyA8	Jurkat
6.35	2.62

Figure 5.3. Cell sorting of HeyA8 and Jurkat cells. a) Flow cytometry analyses of the initial mixture of cells and the cells collected at the stiff and soft outlets show the enrichment for HeyA8 cells ($E = 0.71 \pm 0.53$ kPa) was 6.35-fold and for Jurkat cells ($E = 0.290 \pm 0.11$ kPa) was 2.62-fold. HeyA8 cells were fluorescently labeled green for these studies and Jurkat cells were labeled red. a) AFM measurement of Young's modulus of Jurkat cells and HeyA8 cells initially, before mixing and flowing, show that HeyA8 cells and Jurkat cells differ greatly in Young's modulus (n = 27 for each cell type). c) HeyA8 cells and Jurkat cells are similar in cell diameter when suspended (n = 22, n = 43 respectively). c) Separated cells at outlets were measured by AFM (n = 30 for each cell type). Nonparametric Wilcoxon signed-rank tests were used to test statistical significance, with * indicating a $p < 0.001$ and ns indicating no significance.

To further demonstrate cell separation by cell stiffness, another pair of cells: Hey and K562 was tested. Similar to HeyA8, Hey is also an ovarian cancer cell line but has less metastatic potential. Like Jurkat cells, K562 is also a lymphoblast leukemia cell line. The mixture of Hey cells (E = 0.78 ± 0.53 kPa) and K562 cells (E = 0.40 ± 0.22 kPa) were streamed using the same flow conditions as HeyA8/Jurkat separation. Compared to HeyA8/Jurkat cell pair, the stiffness difference of Hey/K562 pair was less than 400 Pa with increased overlap

between the two cell types (Figure 5.4b). Hey and K562 have similar cell diameters (Figure 5.4c). The separation results were evaluated by flow cytometry (Figure 5.4a) and enrichment for Hey cells was 5.5-fold at the stiff outlet and for K562 cells was 1.9-fold at the soft outlet. The enrichment of K562 and Hey cells again demonstrated that cells of similar in size but different in stiffness can be separated.

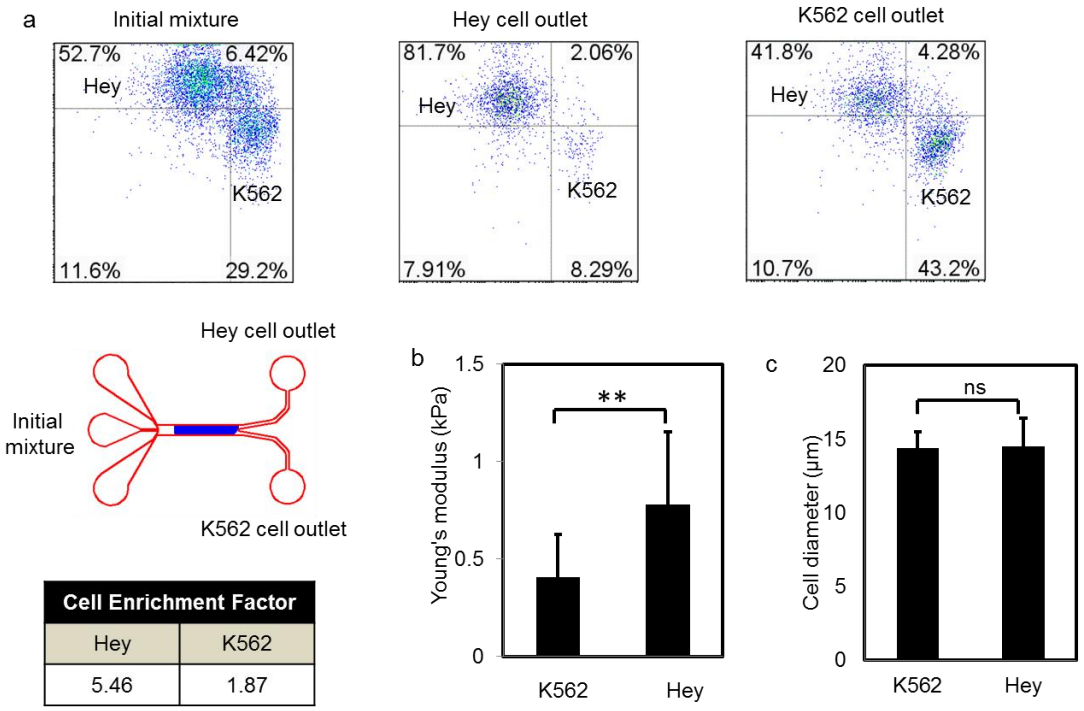

Cell Enrichment Factor	
Hey	K562
5.46	1.87

Figure 5.4. Cell sorting of Hey and K562 cells. a) Flow cytometry analyses of the initial mixture of cells and the cells collected at the stiff and soft outlets show an enrichment for Hey cells (E = 0.78 ± 0.53 kPa) of 5.5-fold and for K562 cells (E = 0.4 ± 0.22 kPa) of 1.9-fold. b) Cell stiffness was measured with AFM (n = 27 for each cell type) and quantified in terms of Young's modulus. c) K562 and Hey cells are similar in cell size: 14.4 ± 1.1 for K562 and 14.5 ± 1.9 for Hey (n = 30 for each cell type). A nonparametric Wilcoxon signed-rank test was used to test statistical significance, with ** indicating a $p < 0.0001$, and ns indicating not significant.

To examine the enrichment of cells with large differences in stiffness, a mixture of K562 cells (E = 0.40 ± 0.22 kPa) and 4% formaldehyde treated K562 cells (K562F, E = 23 ± 13 kPa)

were flowed and the results were analyzed with flow cytometry (Figure 5.5a). The formaldehyde fixation process caused substantial cross-linking of cellular structures which produced cells with high stiffness, as measured by AFM (Figure 5.5b). The enrichment for formaldehyde treated K562 cells was 6.7-fold and for untreated K562 cells was 2.3-fold. This result demonstrated that the ridged channel can be used to separate cells with large differences in stiffness.

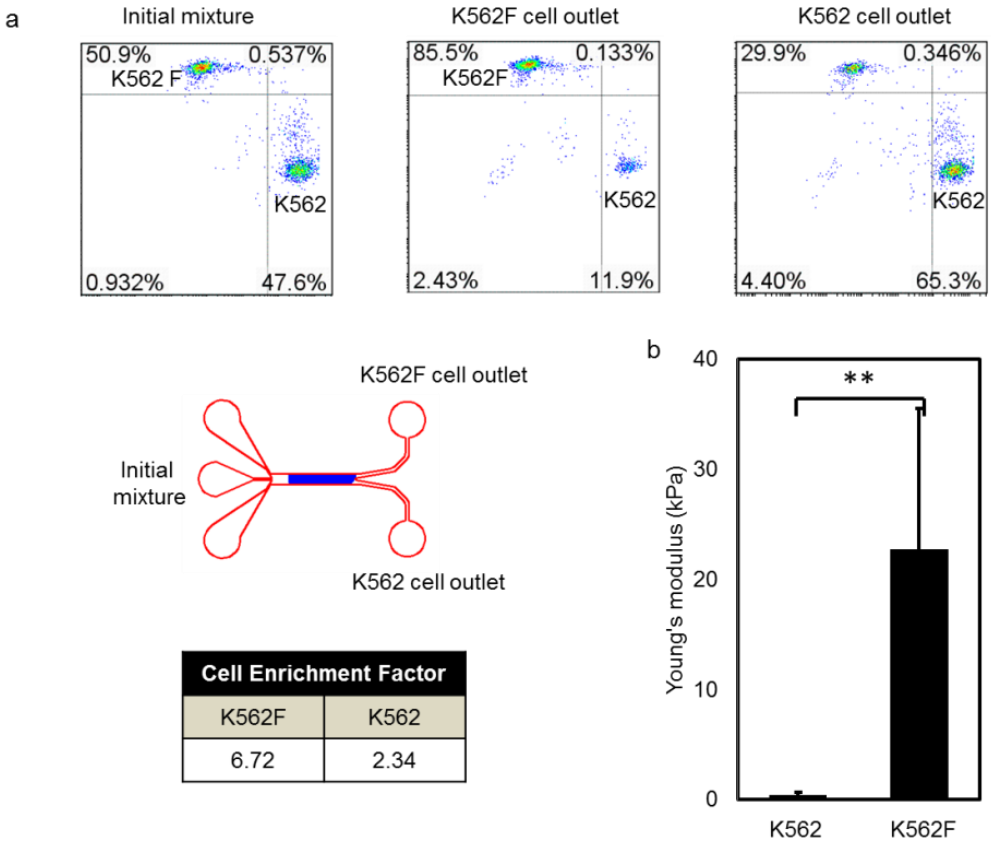

Cell Enrichment Factor	
K562F	K562
6.72	2.34

Figure 5.5. Cell sorting of K562 and 4% formaldehyde treated K562 cells. a) Flow cytometry analyses of the initial mixture of cells and the cells collected at the stiff and soft outlets show an enrichment of both cell types at the stiff and soft outlet respectively. 4% formaldehyde treated K562 cells (E = 23 ± 13 kPa) were enriched 6.7-fold at the stiff outlet and untreated K562 cells (E = 0.40 ± 0.22 kPa) were enriched 2.3-fold at the soft outlet. b) Cell stiffness was measured with AFM and quantified in terms of Young's modulus. n = 25 for each cell type. A nonparametric Wilcoxon signed-rank test was used to test statistical significance, with ** indicating a $p < 0.0001$.

To probe the lower resolution limitation of the microfluidic cell sorting by stiffness, a mixture of Hey cells (E = 0.78 ± 0.53 kPa) and HeyA8 cells (E = 0.71 ± 0.53 kPa) which had significant overlap in stiffness were flowed into the microfluidic cell sorter. The average Young's modulus difference was less than 100 Pa. Under the conditions tested, no appreciable separation between these two cell lines was achieved (Figure 5.6).

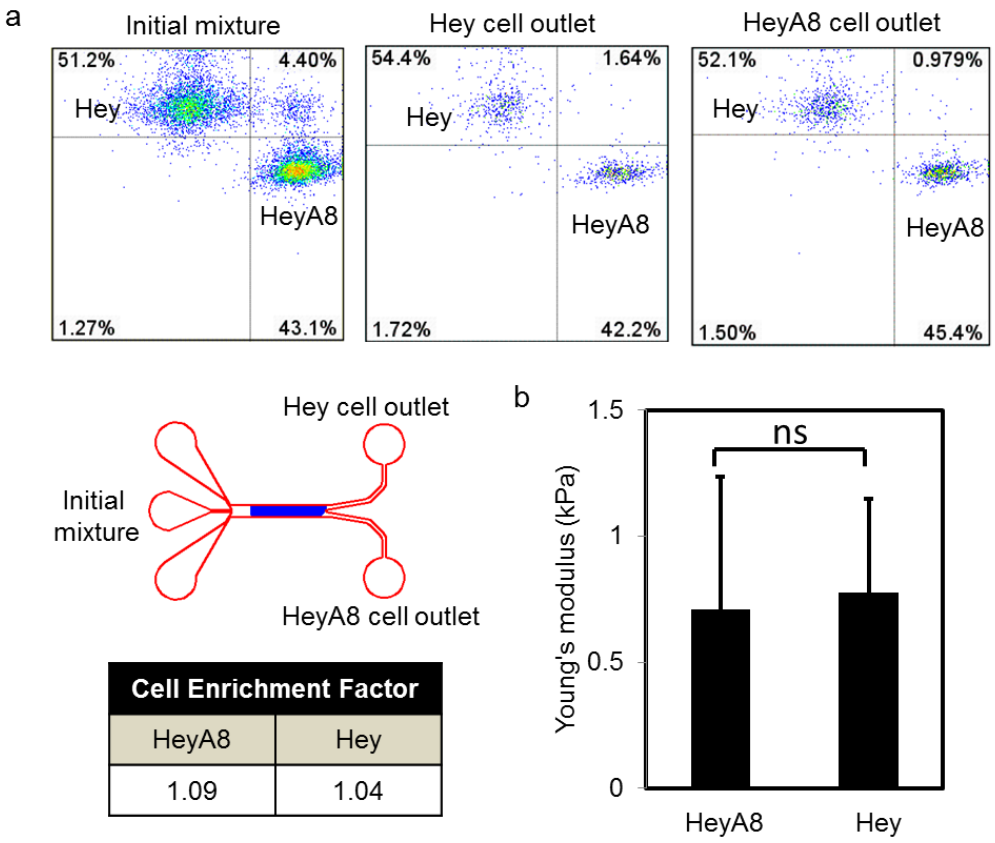

Cell Enrichment Factor	
HeyA8	Hey
1.09	1.04

Figure 5.6. Cell sorting of Hey and HeyA8 cells. a) Flow cytometry analyses of the initial mixture of cells and the cells collected at the stiff and soft outlets show no significant cell enrichment of Hey and HeyA8 cells. b) AFM measurement of Hey and HeyA8 cell stiffness show the Hey (E = 0.78 ± 0.53 kPa) and HeyA8 (E = 0.71 ± 0.53 kPa) Young's modulus do not differ significantly (n = 25 for each cell type).

To verify the viability of cells after flowing through the device, we cultured untreated K562 cells that were collected from the device outlets. The cells were cultured for six days and

compared with a control population which did not undergo separation. We observed no significant difference in viable cell numbers and concluded that the majority of cells survived the transit and repeated compression through the device (Figure 5.7). Separated cells can therefore be used for downstream analysis.

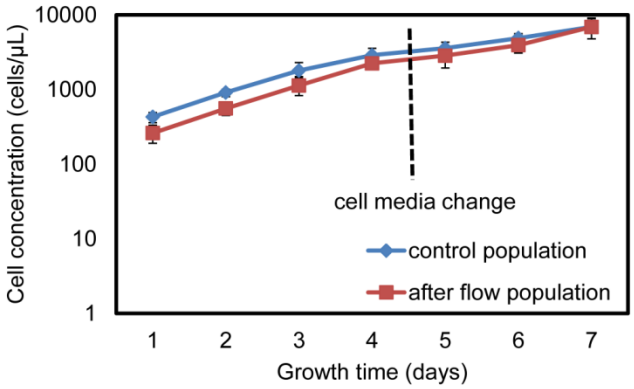

Figure 5.7. K562 cell growth monitored for cells collected after flow experiment. Cell concentrations were measured using a hemocytometer and recorded for seven days. The doubling time for entire seven-day observation was 1.5 days for control and for 1.3 days for cells after flow experiment. Therefore, the growth rate (ln(2)/doubling time) is 0.46 ± 0.071 day^{-1} for the control (blue diamonds) and 0.53 ± 0.097 day^{-1} for the cells after flow experiment (red squares). The error bars represent standard deviations.

The cell solution temperature is not a contributing factor to the cell sorting process. We conducted cell separation at 4°C, room temperature (~25°C) and physiological temperature (~37°C) for HeyA8/Jurkat cell separation and did not observe noticeable difference in cell enrichment.

In chapter 4, it is shown that flow rate affects the cell trajectory. Therefore, the flow rate is also a key parameter in cell separation since it defines the hydrodynamic force imposed on cells. The channel flow is formed by three inlet streams including two sheath streams which provide hydrodynamic focusing and a cell sample stream which contains the cells. We

investigated flow rate effect with Jurkat cells and HeyA8 cell sorting. We observed that for high channel flow rate (greater than 5 mL/min) where hydrodynamic force was dominant, most of the cells migrated to the soft outlet and weak separation took place. On the other hand, a slow channel flow rate (less than 0.005 mL/min) resulted in cells occluding the channel. The most efficient separation of Jurkat cells and HeyA8 cells occurred when the channel flow rate was about 0.05 mL/min (Table 5.1).

Table 5.1. Effect of channel flow rate on Jurkat and HeyA8 cell separation. At fast flow rate, the hydrodynamic force was dominant and pushed stiff cells migrated to soft outlet which resulted in the lowest enrichment. At slow flow rate, cells were stuck to the ridges and occluded the channel which resulted in the lowest throughput. We determined channel flow rate at 0.05 mL/min provided the best separation result. The cell retention is defined by calculating the ratio of cells collected at the outlet and total number of cells injected in the inlet. For example, the stiff outlet retention is $\frac{(\text{HeyA8})_{\text{stiff outlet}}}{(\text{HeyA8+ Jurkat})_{\text{inlet}}}$. The total retention is the sum of cells collected at the two outlets.

	Enrichment			**Cell Retention**		
Channel Flow Rate	**HeyA8 Outlet**	**Jurkat Outlet**	**Throughput**	**HeyA8 Outlet**	**Jurkat Outlet**	**Total**
0.025 mL/min	3.4-fold	2.1-fold	83 cells/sec	26%	26%	52%
0.05 mL/min	6.3-fold	3-fold	250 cells/sec	41%	41%	82%
0.25 mL/min	2.8-fold	1.1-fold	833 cells/sec	12%	72%	84%

The separation throughput depends on both the cell concentration and the flow rate. For cell lines used, we tested cell concentrations up to 4×10^6 cells per mL at which point the delayed transit times of stiffer cells at the leading edge of the ridge blocked the flow of subsequent cells, eventually leading to channel occlusion. Moreover, the flow rate will ultimately be limited by the decreased sensitivity to variations in stiffness due to the dominance of hydrodynamic force. For the results presented, a flow rate of 0.05 mL/min and cell concentration at 10^6 cells per mL

yielded a throughput of 250 cells per second. To further increase the throughput, multiple channels can be implemented and operate simultaneously.

Other parameters that influence cell separation include ridge width, b, ridge angles, α, and ridge pitch, L. The ridge width should be comparable to cell diameter. If the ridge width is too small, the cells would only be deformed partially which results in a weak elastic force. On the other hand, if the ridge is too wide, the cell will have difficulty to pass through which leads to channel occlusion. Furthermore, the device should include a sufficient ridge pitch to allow the cells to mechanically relax. The larger the pitch, the more relaxation occurs and the transverse force/displacement should increase, though at a cost of increased channel length. The cell separation will also depend on the angle of ridges relative to the channel axis. The separation takes place due to simultaneous action of two opposing effects: compression of cells by ridges leading to the deflection of stiffer cells in the positive transverse direction, and circulatory secondary flows that transport softer cells in the negative transverse direction. The magnitude of the secondary flows is at maximum when the ridges are oriented 45 degrees with respect to the channel axis.

5.1.1 Materials and Methods

The K562 cells (CCL-243) and Jurkat cells (CRL-1990) were purchased from ATCC. HeyA8 and Hey cell lines were provided by Dr. G. Mills (MD Anderson Cancer Center, Houston, TX). Red blood cells were withdrawn from healthy donors using protocols (H12002) approved by the Georgia Institute of Technology Institute Review Board. This research involving human participants was approved by the Georgia Institute of Technology Institute

Review Board. We have received written consent from the donors of the RBCs used in this study. K562 cells were cultured and maintained in Iscove's modified Dulbecco's medium (ATCC) with the addition of 10% fetal bovine serum (FBS). Jurkat, Hey and HeyA8 cells were cultured and maintained in RPMI-1640 medium (Sigma) with the addition of 10% FBS. All cells were incubated at 37°C with 5% CO_2. Cells were expanded to 80% confluency in a culture flask over two days. CytoD was added to K562 cells and incubated for 2 hours and washed twice. To avoid the reversible effect of the CytoD treatment, the cells treated with CytoD were immediately used for the flow experiment and the AFM measurement. 4% formaldehyde was added to K562 cells and incubated at room temperature for 30 minutes and wished twice. RBCs were isolated from whole blood through centrifugation and 10% v/v sodium citrate anticoagulant was added and cell solution was diluted in DPBS buffer. Four different cell labeling agents were used. Except for RBC experiment, we used lipid stains: Vybrant DiO (Life Technologies) and Vybrant DiD (Life Technologies) at 5 μL/mL. Accuri C6 (BD) flowcytometer was used to measure cell enrichment. Cells at the inlet and cells collected at the outlets were analyzed using flowcytometry.

We utilized atomic force microscopy to accurately verify the stiffness of the cells. All cells were measured in suspended states with only slight attachment to the surface. To measure cells in suspended state, a monolayer of poly-l-lysine (MW 300,000 Sigma Aldrich) was grafted onto the glass slide substrate. This operation provided anchorage of the cell to the glass substrate while maintaining roundedness of morphology for cells and improved the cell stability during the AFM measurements. We carried out our AFM experiment immediately after the washing step and poly-l-lysine cell attachment treatment and all measurements were finished within 2 hours. We did not observe a change in measured stiffness during the course of these measurements.

Measurements were conducted using a MFP-3D AFM (Asylum Research) attached to an inverted optical microscope (Nikon Eclipse Ti*).* A silicon nitride cantilever with a spring constant equal to 37.1 pN/nm and a pyramidal tip was positioned above the center of a single cell and indented the cell. *P*rior work showed that the Young's modulus is a function of loading force and loading rate[1]. We utilized the same values for these parameters for all AFM measurements. The magnitude of indentation force used in all AFM measurements is 5 nN and the rate of indentation is 1.5 μm/s. The applied force was sufficient to indent cells approximately 4 μm. These values for the AFM parameters were selected to serve the purpose of comparing results with previous studies [1-4]. The force-indentation curve was obtained for each measurement and then analyzed with a Hertzian model for a pyramidal tip (Wavemetrics, IgorPro software routines) from which the Young's modulus values were calculated.

5.2 Separation of Cells Based on Cell Size

In addition to cell stiffness, variations in cell size can also be utilized to separate cells. For instance, rare cells such as circulating tumor cells (CTC) are much larger than red blood cells. However, the CTCs are extremely rare. It is estimated that only one CTC is in one billion normal cells in the blood circulation of patients with advanced cancer[5]. This makes the detection of cancer by means of CTC very challenging. The current designs of microfluidic channels could not offer the sensitivity required for isolation of CTCs. Nonetheless, the channel can enrich CTCs from red blood cells. The enrichment serves as a preparation for subsequent CTC capturing using more sensitive techniques such as immunomagnetic cell sorting in the

FDA-approved CellSearch system. The blood sample preparation can improve the sensitivity and specificity of the downstream CTC isolation.

HeyA8, an aggressive metastatic ovarian cancer cell line was mixed with red blood cells (RBCs). The HeyA8 had an average cell diameter of 16.8 ± 2.6 μm which was twice the size of a red blood cell whose average diameter was 7.8 ± 1.1 μm (Figure 5.8b). The cell enrichment factor at the HeyA8 outlet was 7.2 fold and 7.4 fold at the RBC outlet (Figure 5.8a). The high enrichment factors of both cell types were primarily due to the pronounced size difference. Although HeyA8 cells was a lot stiffer compared to RBCs (Figure 5.8c), the cell stiffness difference played a minor role because RBCs were not compressed by the ridges. The gap size used was 8 μm which was comparable to the RBC diameter. Therefore, cell separation was primarily a result of difference in cell size.

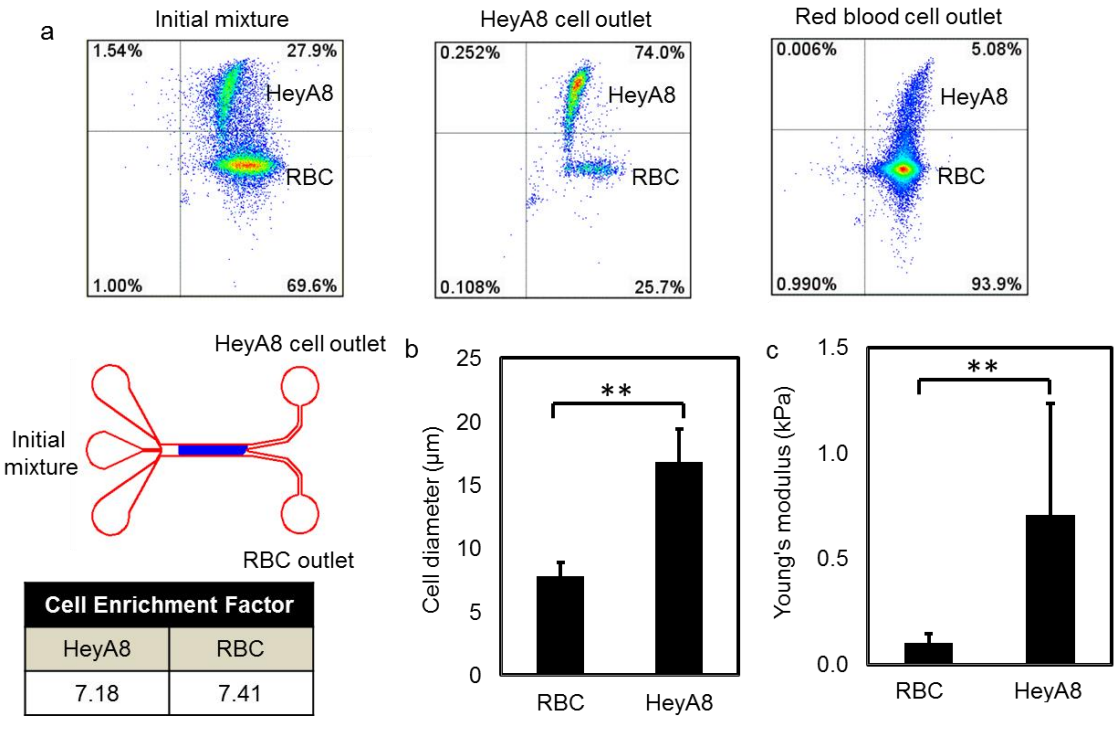

Cell Enrichment Factor	
HeyA8	RBC
7.18	7.41

Figure 5.8. Cell sorting of HeyA8 and red blood cells. a) Flow cytometry analyses of cell mixture at inlet and cells collected at the outlets. The cell enrichment factors for HeyA8 and red

blood cells are 7.18 and 7.41 respectively. HeyA8 and RBC differ significantly in size and stiffness. b) The cell diameters for RBC and HeyA8 are 7.8 ± 1.1 μm and 16.8 ± 2.6 μm respectively (n = 35 for each cell type). c) The Young's modulus for RBC and HeyA8 are 0.11 ± 0.043 kPa and 0.71 ± 0.53 kPa respectively (n = 25 for each cell type).

To demonstrate another application of cell separation by size and also to examine cells with less size difference, mouse embryonic stem cells (mESCs) and mouse embryonic fibroblast cells (mEFs) were separated (Figure 5.9a). Many tissue engineering applications require high purity stem cell population. However, pure stem cells populations do not exist naturally in any parts of the body. Stem cells have to be harvested from a pool of differentiated cells. For example, mEFs are fibroblast cells that serve as a feeder layer that provides nutrients to mESCs when cultured *in vitro*. Although mESCs and mEFs have very similar stiffness (Figure 5.9b), their cell size is quite different (Figure 5.9c). The average Young's modulus for mESCs and mEFs were 0.29 ± 0.098 kPa and 0.23 ± 0.27 kPa respectively. The average cell diameters for mESCs and mEFs were 17.7 ± 3.71 μm and 24.0 ± 7.64 μm respectively.

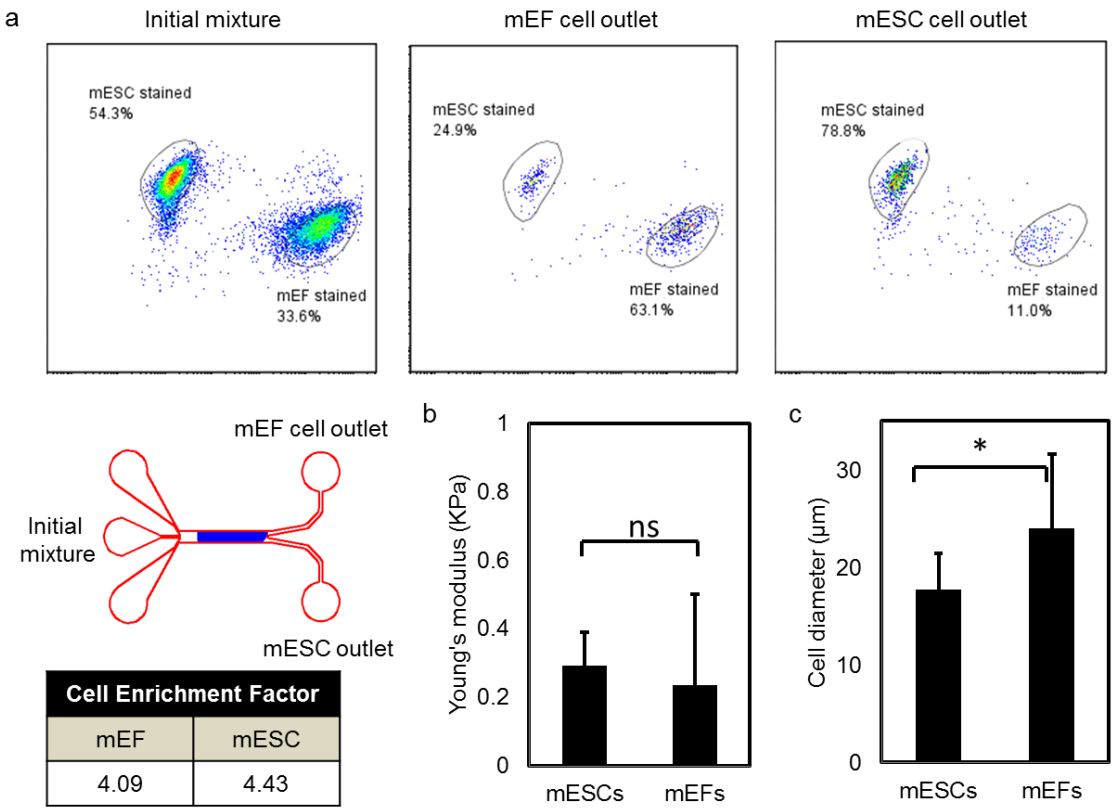

Cell Enrichment Factor	
mEF	mESC
4.09	4.43

Figure 5.9. Cell sorting of mEFs and mESCs. Flow cytometry analyses of cell mixture at inlet and cells collected at the outlets. The cell enrichment factors for mEFs and mESCs are 4.09 and 4.43 respectively. b) mESCs and mEFs do not differ significantly in cell stiffness. The Young's modulus for mESCs and mEFs are 0.29 ± 0.098 kPa and 0.23 ± 0.27 kPa respectively (n = 25 for each cell type). c) mESCs and mEFs differ significantly in cell size. The diameters of mESCs and mEFs are 17.7 ± 3.71 μm and 24.0 ± 7.64 μm respectively (n = 50 for each cell type).

The size-dependent separation of mEFs and mESCs relied on similar sorting mechanism in the HeyA8/RBC case. The gap size selected for microfluidic cell sorter was 18 μm which was greater than the average diameter of mESCs but sufficient to deform mEFs. Since mESCs were not deformed, cell separation was primarily a result of difference in cell size instead of stiffness.

5.2.1 Materials and Methods

The mEFs (SCRC-1008) and mESCs (CRL-1934) were purchased from ATCC. mEFs were cultured and maintained in Dulbecco's Modified Eagle's Medium (DMEM) with 15% v/v fetal bovine serum (FBS). mESCs were cultured in a standard feeder-free culture containing DMEM with 15% v/v FBS. Leukemia inhibitory factor (LIF) was added to prevent mESCs from cell differentiation. Both cells were stored in 37°C with 5% CO_2. Cells were expanded to 80% confluency in a culture flask over five to six days. Red blood cells were isolated from whole blood drawn from healthy donors using Georgia Tech IRB approved protocol (H12002). The isolated red blood cells were diluted with DPBS to desired concentrations. Cell staining process is the same in section 5.1.1.

Atomic force microscopy was used to measure cell stiffness. For the mESCs, 50,000 cells were plated on a glass culture dish in LIF and DMEM media and adhered overnight. Similarly mEFs were also plated on a glass substrate but only adhered for 30 minutes. *Measurements were conducted using a MFP-3D AFM (Asylum Research) attached to an inverted optical microscope (*Nikon Eclipse Ti). *A silicon nitride cantilever with a spring constant equal to 11.43 pN/nm and a pyramidal tip was positioned above the center of a single cell and indented the cell.* The magnitude of indentation force used in all AFM measurements is 5 nN and the rate of indentation is 2 μm/s.

5.3 Separation of Cells Based on Cell Viscosity

We report a microfluidic approach to separate and enrich a mixture of two cell types based on differences in cell viscoelastic behavior during repeated compressions and relaxation events. We demonstrate that variations in viscoelasticity affect the flow trajectory of one type of

leukemia cell (K562) in relation to another type of leukemia cell (HL60) as well as healthy leukocytes. These differences in cell trajectory can be utilized to enrich and sort K562 cells from HL60 cells and leukocytes. The microfluidic device utilizes periodic, diagonal ridges to compress and translate the cells laterally perpendicular to channel axis. The ridge spacing is tuned to allow relaxation of the K562 cells but not the HL60 cells or leukocytes. Therefore, the periodic compression laterally translates weakly viscous cells, while highly viscous cells respond to hydrodynamic circulation forces generated by the slanted ridges. As a result, cell sorting has strong dependency on cell viscosity. We use atomic force microscopy and high-speed optical microscopy to measure cell stiffness, cell relaxation rate constant, and cell size for all cell types. With properly designed microfluidic channels, we can optimize the enrichment of K562 cells from HL60 or leukocytes.

The difference between elasticity and viscosity is that elastic force is proportional to deformation whereas viscous force is proportional to deformation rate. The concept of cell viscosity can be understood as the resistance to deformation or change in cell shape. For example, when a highly viscous cell is deformed at the first ridge, the cell resists the deformation as it moves along the edge of the ridge which is similar to a weakly viscous cell. However, after the ridge compression, the highly viscous cells resist relaxation by remaining in the compressed shape. As a result, the subsequent compressions will not deform the cells as much as the first compression. Therefore, the trajectory of the highly viscous cells is mainly dominated by the secondary flow. However, if the ridge spacing is expanded long enough such that the cell is given sufficient time to relax and restore to the original unreformed state, the trajectory of a highly viscous cell will again be similar to a weakly viscous cell. Consequently, we can exploit

the cell viscosity difference by engineering ridge geometry such as ridge spacing to separate highly viscous cells from weakly viscous cells.

Since the cells are viscoelastic materials, their dynamic response after compression is time-dependent. Cell relaxation depends not only on a short time scale which occur between sequential ridge compressions but also on a longer time scale due to repeated compressions[6]. In a serial micropipette aspiration experiment, Mak *et al* used fluorescence and phase contrast imaging to show that the repeated compression of cells resulted in significant changes in the structures of cytoskeleton and nucleus[6]. Therefore, we consider that the viscous properties of cells vary over the course of repeated cell compression events of cell sorting.

To demonstrate microfluidic sorting of cells based on differences in cell viscosity, we selected two leukemia cell lines K562 and HL60. These two cell types have differences in cell size (Figure 5.10a), cell elasticity (Figure 5.10b), however, exhibit similar calculated cell deformation energies (Figure 5.10c). The cell relaxation rate measured with AFM differed significantly, with the K562 cells less viscous compared to HL60 cells (Figure 5.10d). This result agrees with previous micropipette experiments that reported HL60 cells to flow as if liquid into the micropipette when suctioned[7]. To verify our AFM technique, we tested an extreme scenario in which 4% formaldehyde was added to K562 cells. After the crosslinking treatment, the cells exhibited highly elastic behavior with three fold increase in the relaxation rate constant (Figure 10d). From these measurements we conclude that HL60 cells are highly viscous and significantly different viscoelastic properties than K562 cells.

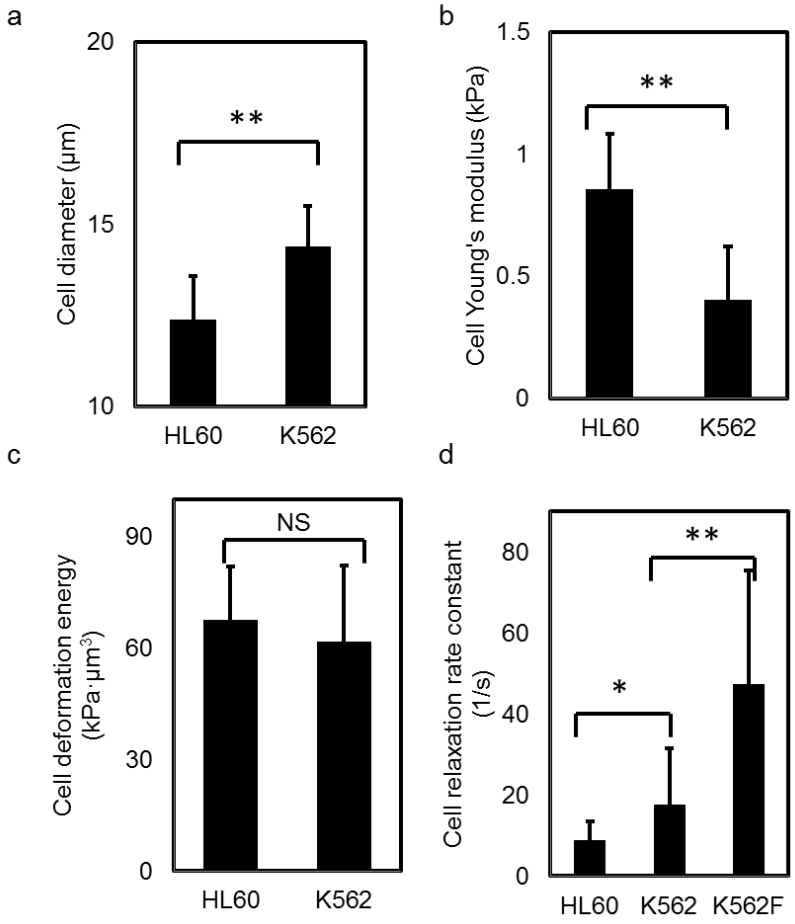

Figure 5.10. Biophysical properties of two leukemia cell lines K562 and HL60. a) K562 is larger than HL60. The average cell diameter for K562 and HL60 cells are 14.4 ± 1.1 μm (n = 25) and 12.4 ± 1.2 μm (n = 36). (b) AFM measurements of cells' Young's modulus show that HL60 (E = 0.86 ± 0.22 kPa, n = 24) is stiffer than K562 (E = 0.40 ± 0.22 kPa, n = 37). c) The average values of Young's modulus and cell diameter were used to calculate cell deformation energy. K562 and HL60 have similar deformation energy (61.9 ± 20.3 kPa·μm^3, and 67.6 ± 14.5 kPa·μm^3 respectively) when compressed with 9 μm channel gap height. d) AFM measurements of cell relaxation show HL60 (8.91 ± 4.6 s^{-1}, n = 63) is slower in size recovery than K562 (17.7 ± 13.7 s^{-1}, n = 69). 4% formaldehyde treated K562 cells (K562F) have the fastest recovery time (47.5 ± 27.9 s^{-1}, n = 42) due to extreme crosslinking of internal cellular structure.

In chapter 4, we discussed the channel geometric parameters have profound effect on cell sorting. Figure 5.11a and 5.11b compares the cell separation of HL60 and K562 mixtures for two channel designs. The channel with ridge spacing L = 200 μm had cell enrichment factor of 6.34

and 4.04 for K562 and HL60 cells respectively (Figure 5.11b). Compared to L = 100 μm, the enrichment was improved by more than 90% for K562 and 75% for HL60. Cell enrichment factors for other channel designs are listed in Figure 5.11c. The channel with 30 degree ridge, L = 200 μm, and 30 ridges has the highest enrichment factors. This result could be predicted by examining the cell lateral displacement listed in Table 4.1 in Chapter 4. We would expect that the 30 degree ridge channel with larger ridge spacing (L = 200 μm) to yield the best separation, since the total divergence in lateral displacement is the greatest. It should be noted when examining Figure 5.11c, if the cell enrichment factor was lowered for one cell type, it also diluted the enrichment for other cell type, since the "unwanted" cells were collected at the "wrong" outlet.

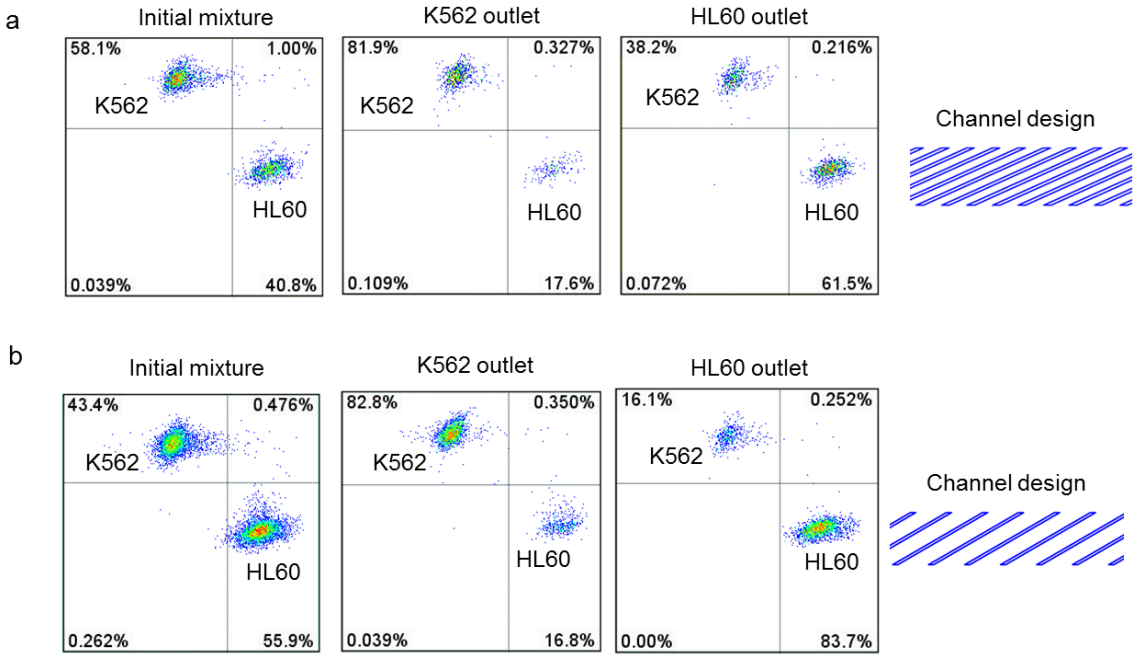

c

Cell Enrichment Factor		
Channel Design	K562	HL60
30 Degree Ridge (*L* =100 μm, 30 ridges)	3.26	2.29
45 Degree Ridge (*L* =78μm , 30 ridges)	2.07	2.85
30 Degree Ridge (*L* =100 μm, 70 ridge)	1.15	1.75
30 Degree Ridge (*L* =200 μm, 30 ridges)	6.34	4.04

Figure 5.11. Cell sorting and optimization of HL60/K562 pair. a) Flow cytometric analysis of cell enrichment from a 30 degree ridge channel with ridge spacing at 100 μm. At the outlets, K562 and HL60 cells were enriched at 3.26 and 2.29 folds respectively. b) Flow cytometric analysis shows the when ridge spacing is increased to L = 200 μm, the cell enrichment factor improved to 6.34 for K562 cells and 4.04 for HL60 cells which represents a 90% and 70% increase respectively compared to smaller ridge spacing channel (L = 100 μm). c) Cell enrichment factors using other microfluidic channel designs are tabulated for K562/HL60 cell pair.

We further demonstrate that our microfluidic approach can enrich K562 leukemia cells from healthy white blood cells due to differences in viscoelastic properties. White blood cells were isolated from whole blood and suspended in saline solution. Roughly 1 to 2 million white blood cells were isolated from 1 mL of whole blood. AFM microscopy was used to measure the

white blood cell stiffness and relaxation time constant. Cell diameter of leukocyte population was smaller than the K562 cells (Figure 5.12a). The leukocytes had higher Young's modulus (Figure 5.12b). K562 cells had higher deformation energy primarily due to large cell diameter since it scaled to the quartic power (Figure 5.12c). Similar to HL60, the leukocytes were highly viscous cells (Figure 5.12d). We found that the coefficients of variation of cell size, stiffness and viscosity distributions were more pronounced compared to cell lines. This result was expected since the leukocyte population consists of multiple cell types.

Since the leukocytes had lower deformation energy and similar viscosity compared to HL60 cells, we expected to observe similar separation properties with respect to K562 cells. The flow cytometric analysis showed this channel design had the best cell separation for the K562 and leukocyte pair. We obtained a 5.3-fold of K562 enrichment (Figure 5.12e). We subsequently tested cell sorting in other channel designs but found that the channel with 30 degree ridge enlarged spacing gave the best separation result.

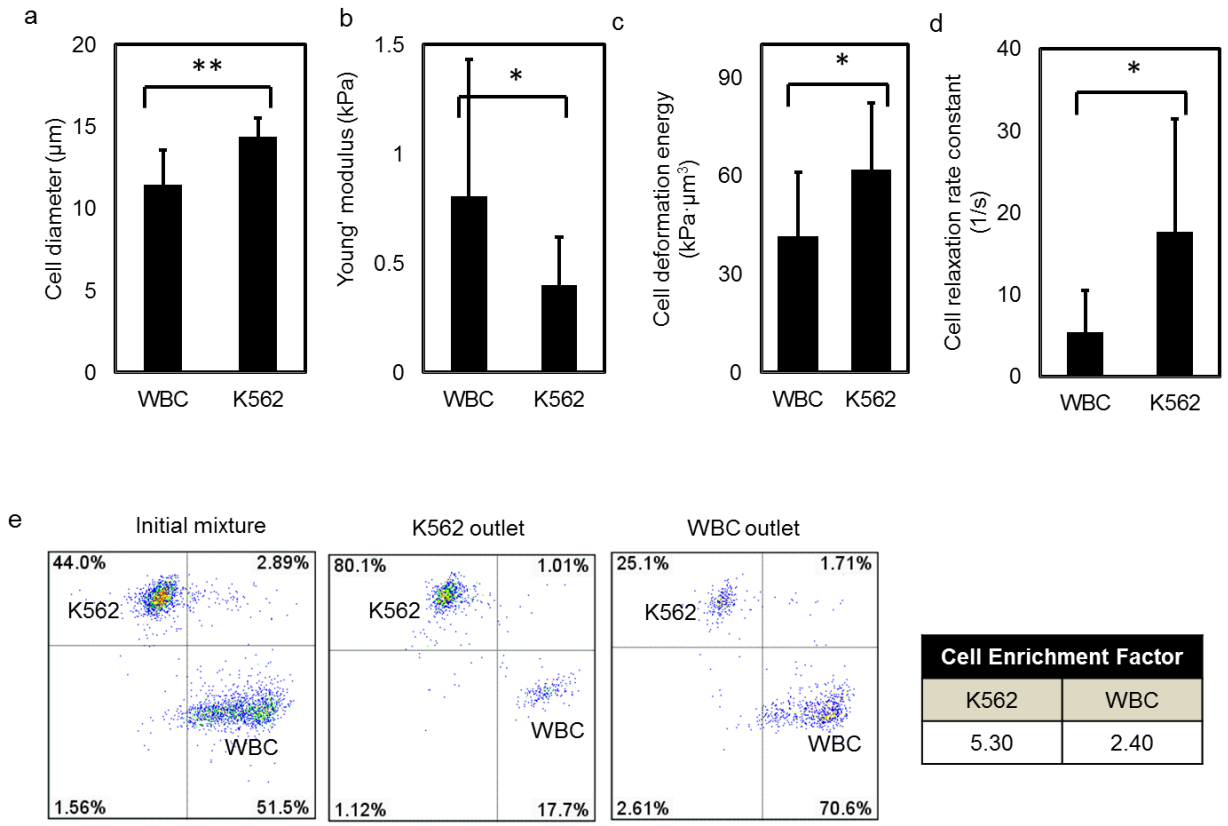

Cell Enrichment Factor	
K562	WBC
5.30	2.40

Figure 5.12. Cell sorting of K562 and white blood cells. a) K562 cells (d = 14.4 ± 1.1 μm, n = 25) are larger compared to leukocytes (d = 11.5 ± 2.1 μm, n = 49). b) Leukocytes (E = 0.81 ± 0.62 kPa, n = 49) have higher Young's modulus compared to K562 cells (E = 0.40 ± 0.22 kPa, n = 37). c) Cell deformation energy for leukocytes and K562 cells are 41.7 ± 19.5 kPa·μm^3, and 61.9 ± 20.3 kPa·μm^3 respectively. d) Leukocytes are highly viscous cells compared to K562 cells. The cell relaxation time constants for leukocytes and K562 cells are 5.47 ± 5.12 s^{-1}, n = 68 and 17.7 ± 13.7 s^{-1}, n = 69 respectively. e) Leukocyte and K562 cell enrichment factor was 5.3 and 2.4 respectively.

The cell sorting mechanism of viscosity-based is different from stiffness-based. As cells undergo initial compression, the cell trajectory is dominated by the size-adjusted elasticity represented by the deformation energy. However, as cells progress through the channel and rapidly compressed by sequential ridges, cell viscosity which sets cell relaxation time plays a more important role. When cell relaxation time is much longer than the time between sequential

compressions, the deformed cells are in disc-shape and their trajectory is primarily affected by the secondary flow induced by the diagonal ridges.

5.3.1 Materials and Methods

HL60 cells (CCL-240) were purchased from ATCC. HL60 cells were cultured and maintained in Iscove's modified Dulbecco's medium (ATCC) with the addition of 10% fetal bovine serum (FBS). Cells were stored at 37 degree Celsius with 5% CO_2. Cells were expanded to 0.5 million cells per mL in a culture flask over two days. Whole blood was withdrawn from healthy donors using Georgia Tech IRB approved protocol (H12002). White blood cells were separated from fresh whole blood using Ficoll-Paque (1.077, GE Life Sciences) through centrifugation. The remaining red blood cells were lysed using red blood cell lysis buffer for human (Alfa Aesar). The isolated white blood cells were from 1 to 2 million cells per mL of whole blood and were resuspended in DPBS. For characterization of sorting by flow cytometetric analysis (Accuri C6, BD), cells were labelled with lipid stains (Vybrant, Life Technologies) at 5 μL reagent per mL of cell suspension.

Cell mixtures at concentration from 1 to 2 million cells per mL were contained in a 3 mL syringe and infused into the microfluidic channel using syringe pumps (PHD 2000, Harvard Apparatus) at controlled flow rates. The cell trajectories were observed by mounting the microfluidic chip on an inverted microscope (Eclipse Ti, Nikon) and recorded by high-speed camera (Phantom v7.3, Vision Research) at a frame rate of 2000 frames per second. The high-speed videos were analyzed with a customized algorithm in ImageJ to extract cell trajectories.

Cell stiffness and relaxation rate data were measured using an atomic force microscope (AFM, MFP-3D, Asylum Research). All cells were measured with a rounded cell shape to closely resemble the morphology within the microfluidic channel. We applied a monolayer of poly-l-lysine (MW 300k, Sigma Aldrich) to serve as anchors to slightly attach cells to the glass substrate to improve cell stability during AFM measurement. The cell stiffness was represented by the average Young's modulus. Beaded silicon nitride cantilevers (spring constant 37.1 pN per nm) were used to indent the center of cells at 1.5 μm per second. We applied force sufficient to achieve at least 4 μm deformations such that it was in close comparison with our microfluidic compression. Each cell was characterized by three force-indentation curves and fit to a Hertzian model to compute the average Young's modulus. The cell viscosity was characterized by the relaxation rate constant. After maximum indentation of the cell, the tip was held in place while the compression force was monitored for 10 seconds so that cell relaxation can be measured. Cell relaxation was fit to an exponential function and the relaxation rate constant of the cell was calculated.

5.4 Cell Fractionation

Because of the overlap of biophysical properties between two cell types, binary separations will face limits in the degree of enrichment that can be achieved. In principle, cell mixtures can be fractionated by implementing multiple outlets to collect highly pure subpopulations by providing finer gradation of cells based on cell biophysical properties compared to the binary outputs. As a proof-of-concept demonstration, we add an additional outlet to our microfluidic cell sorter (Figure 5.13). Along with the additional outlet, we also

incorporate a few new design elements: the expansion region between the ridged segment of the channel and the outlets and serpentine outlets. The expansion region allows the channel fluid to divide evenly among the outlets. The serpentine channels are included in the outlets to increase flow resistance and prevent flow biasing resulted from uneven outlet sizes. Since cells are continuously separated and collected, an automatic cell collection mechanism is beneficial to the cell separation process. The serpentine outlet design eliminates any flow biasing caused by the external automatic cell collection system.

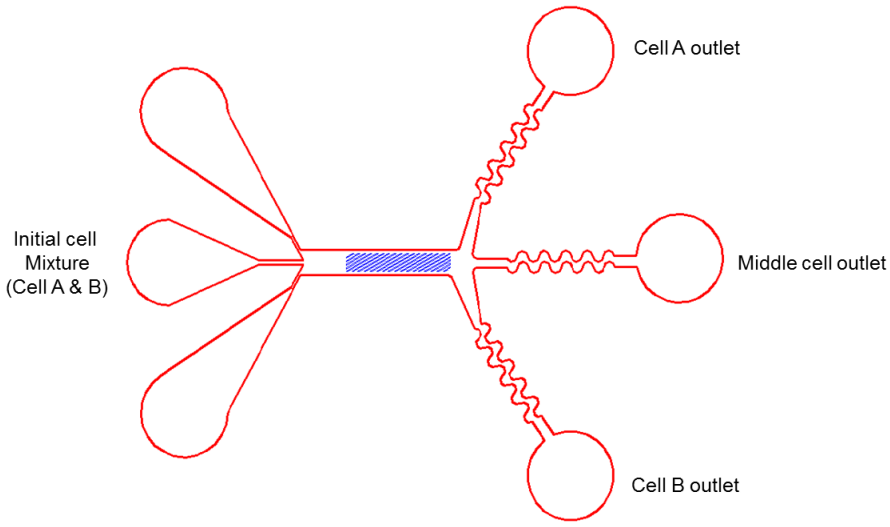

Figure 5.13. Microfluidic cell fractionation sorter.

The hydrodynamics of the cell fractionation is designed using computational fluid dynamics software Ansys Fluent. The flow expansion region and the additional outlet must ensure the even splitting of the channel flow and prevent fluid from biasing. The optimized channel design is shown in Figure 5.14.

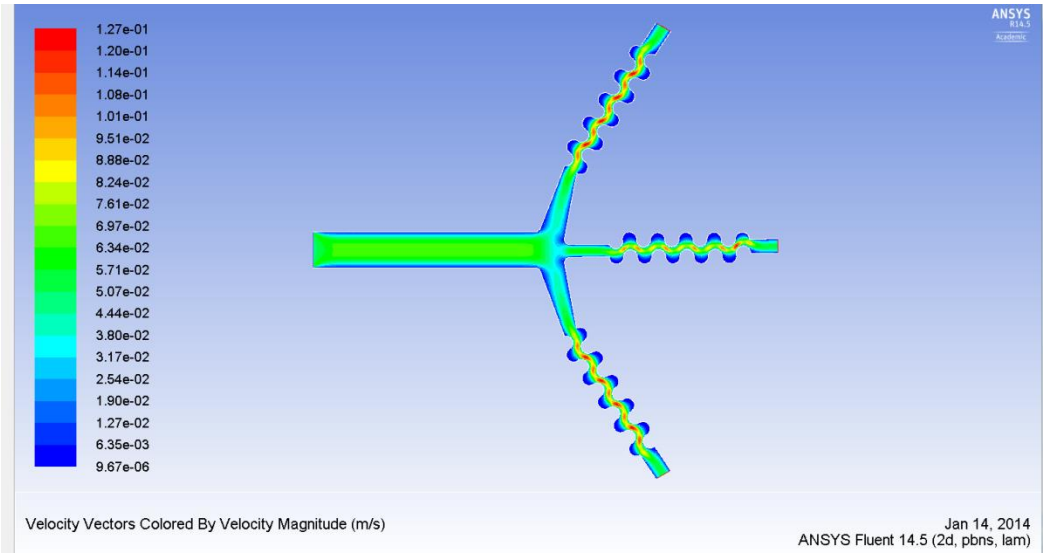

Figure 5.14. Computational fluid dynamics simulation of channel hydrodynamics.

To demonstrate the cell sorting efficiency of the three-outlet channel, we tested cell sorting of K562 and HL60 cells. The biophysical properties and cell separation of K562/HL60 pair is previously reported in section 5.3. The new cell sorting result with the cell fractionation is shown in Figure 5.15. The fractionation concept improves the cell enrichment factor by an order of magnitude compared to previous cell sorting results with binary outputs. The additional outlet in the middle collects K562 and HL60 cells that have overlapping biophysical properties. Therefore, the three-outlet channel shows a dramatic improvement in cell sorting sensitivity and specificity. The cell recovery in each outlet is different. In addition to cell loss during the enrichment process, the K562 cell outlet retained 20% of cells at the inlet, the HL60 cell outlet has 10% and the middle outlet has 50%.

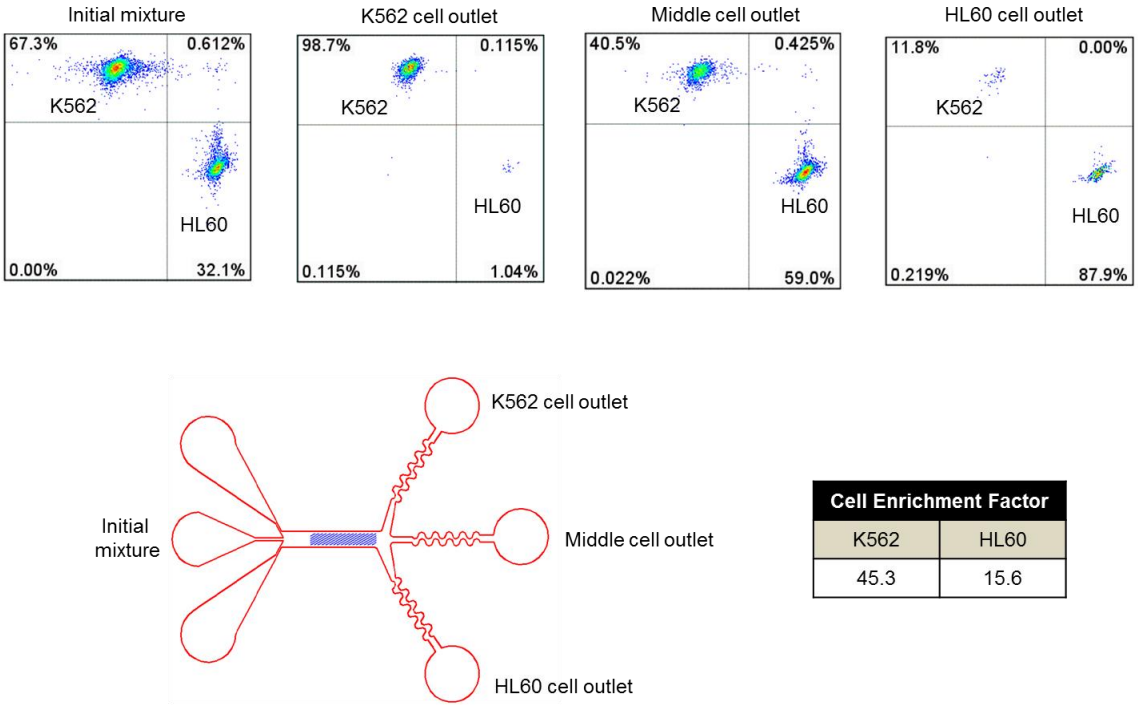

Cell Enrichment Factor	
K562	HL60
45.3	15.6

Figure 5.15. Cell sorting of K562 and HL60 cells in the microfluidic fractionation channel. The flow cytometry results show purity of more than 98% for K562 cells and 87% for HL60 cells. The cell enrichment factors for K562 and HL60 cells are 45.3 and 15.6.

In addition to enrich cell mixtures of different cell types, the three-outlet channel can also be applied to fractionate a single cell type based on differences in biophysical properties. Since biological cells are inherently heterogeneous in nature, their biophysical properties have large spread. For example, K562 cells have average Young's modulus 0.40 kPa and a standard deviation 0.22 kPa. Utilizing the fractionation channel, we are able to distinguish the subpopulations within a single cell type based on subtle differences in biophysical properties (Figure 5.16).

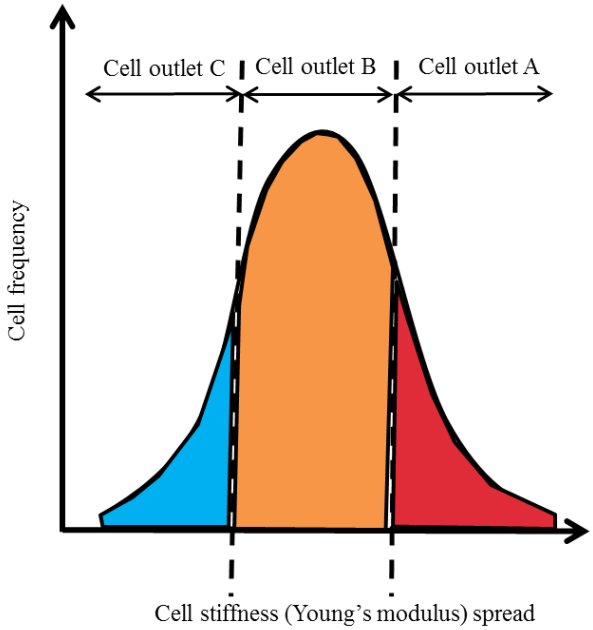

Figure 5.16. Cell fractionation of a single cell type based on biophysical property spread.

K562 cells are fractionated using the three-outlet channel and the separated cells are characterized with AFM immediately after collection at the outlets. The biophysical properties of the K562 cells are provided in section 5.3 and the separated cell subpopulations are shown in Figure 5.17. The AFM measurement shows that K562 cells can be fractionated predominantly based on variations in stiffness and size and less on cell relaxation. The reduction of cell relaxation rate constant in Figure 5.17 d compared to Figure 5.10 d is due to the shortened duration of AFM indentation from 10 seconds to 5 seconds. The size-adjusted elasticity (deformation energy) is significantly different among the cells collected at three outlets. Schematically, the separated cells at outlet A, B and C represent the cell populations at three different colored segments in Figure 5.16.

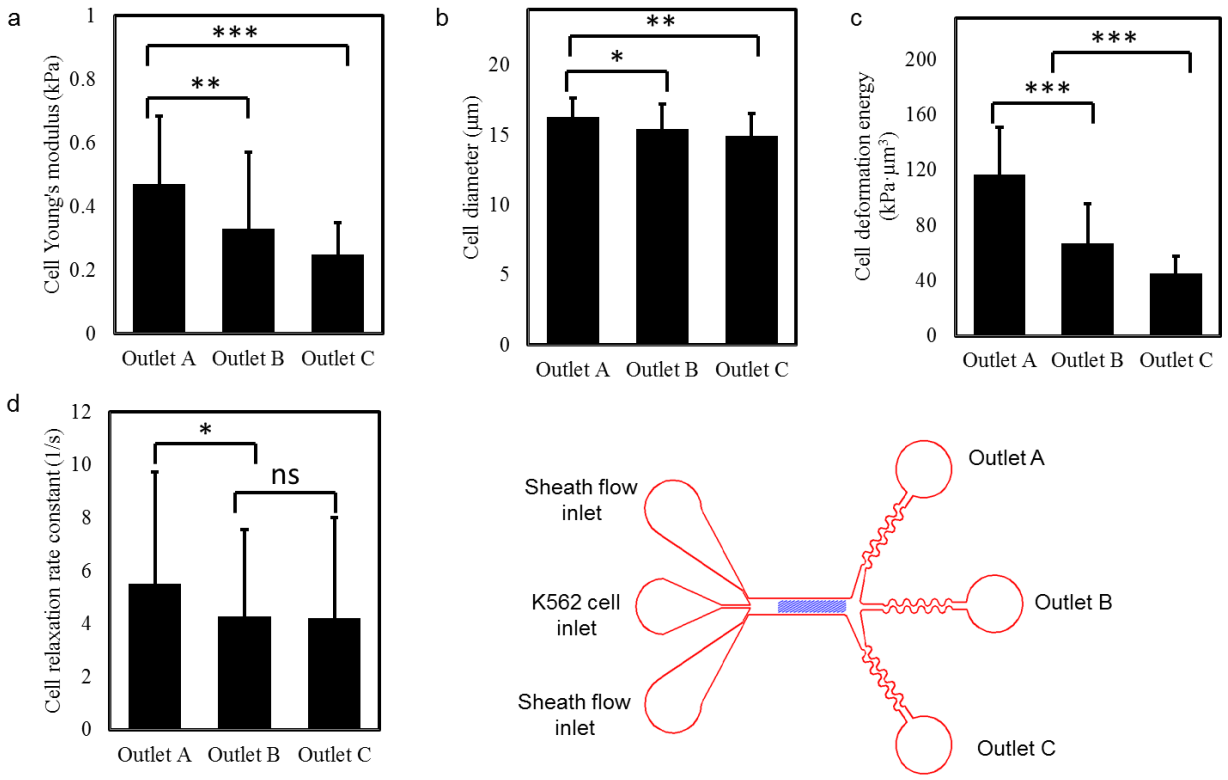

Figure 5.17. K562 cell biophysical properties at three different outlets. a) The Young's modulus of cells collected at outlet A, B and C are E = 0.47 ± 0.215 kPa (n = 27), E = 0.33 ± 0.24 kPa (n = 53) and E = 0.25 ± 0.098 kPa (n = 38) respectively. b) The cell diameters at outlet A, B, and C are d = 16.3 ± 1.4 μm (n = 27), d = 15.4 ± 1.8 μm (n = 53), and d = 15.0 ± 1.6 μm (n = 38) respectively. c) The deformation energy (size-adjusted elasticity) at outlet A, B, and C are 117.1 ± 33.8 kPa·μm^3, 66.9 ± 28.6 kPa·μm^3, and 45.4 ± 12.3 kPa·μm^3 respectively. d) The cell relaxation rate constant at outlet A, B, and C are 5.52 ± 4.23 s^{-1} (n = 20) and 4.29 ± 3.26 s^{-1} (n = 19) and 4.23 ± 3.78 s^{-1} (n = 17) respectively. The statistical significance is marked by ***: $p < 0.0001$, **: $p < 0.01$, * $p < 0.05$, ns: no significance.

In summary, implementing cell fractionation significantly improves cell sorting specificity and sensitivity. In addition, the three-outlet channel enables the detection of subtle differences that exist within a single cell type and separation based on these biophysical property variations.

5.5 References

1. Li QS, Lee GYH, Ong CN, Lim CT (2008) AFM indentation study of breast cancer cells. Biochemical and Biophysical Research Communications 374: 609-613.
2. Rosenbluth MJ, Lam WA, Fletcher DA (2006) Force microscopy of nonadherent cells: A comparison of leukemia cell deformability. Biophysical Journal 90: 2994-3003.
3. Moreno-Flores S, Benitez R, Vivanco MD, Toca-Herrera JL (2010) Stress relaxation microscopy: Imaging local stress in cells. Journal of Biomechanics 43: 349-354.
4. Moreno-Flores S, Benitez R, Vivanco MD, Toca-Herrera JL (2010) Stress relaxation and creep on living cells with the atomic force microscope: a means to calculate elastic moduli and viscosities of cell components. Nanotechnology 21: 445101.
5. Yu M, Stott S, Toner M, Maheswaran S, Haber DA (2011) Circulating tumor cells: approaches to isolation and characterization. Journal of Cell Biology 192: 373-382.
6. Mak M, Erickson D (2013) A serial micropipette microfluidic device with applications to cancer cell repeated deformation studies. Integrative Biology 5: 1374-1384.
7. Schmidschonbein GW, Sung KLP, Tozeren H, Skalak R, Chien S (1981) Passive mechanical-properties of human-leukocytes. Biophysical Journal 36: 243-256.

CHAPTER 6

OUTLOOK AND CONCLUDING REMARKS

In section 6.1, we summarize the main findings and contributions of the research. In section 6.2, we list potential applications of microfluidic cell sorting in the future. In particular, we focus on four areas: scientific research, drug development, therapeutics and clinical diagnostics. In section 6.3, we discuss the limitations of our microfluidic cell sorting approach and provide potential solutions that could circumvent the problems. In addition, we recommend combining cell sorting methods to achieve superior cell sorting results. Section 6.4 concludes the thesis with future research directions.

6.1 Main Findings and Contributions

The main contribution of the research is the creation and characterization of a new microfluidic cell sorting platform that utilizes the biophysical markers to sort cells. We have characterized biophysical properties for cancer and healthy cells from the blood and tissues. We found cell stiffness, cell viscosity and cell size are dissimilar among different cell types and these differences can be exploited to distinguish diseased cells from healthy cells. We invented and developed a new cell sorting platform based on microfluidics. The microfluidic cell sorters are designed and fabricated in-house. We employed the microfluidic cell sorters to sort various types of cells using differences in biophysical properties. We also investigated the effect of channel geometric parameters and flow rates on cell sorting performance and created a general guideline and models for design and optimization of cell sorting. Furthermore, we demonstrated the

practical use of microfluidic cell sorter for potential applications such as cell sample enrichment and preparation, stem cell enrichment, and blood cell separation.

6.2 Potential Applications

Cell sorting has a broad range of applications for scientific research, drug development, therapeutics and clinical diagnostics. The following paragraphs aim to introduce some of the existing applications that routinely use cell sorting technologies and other potential applications that could benefit from cell sorting technologies in the future.

Cell sorting technologies are widely used in bio-related research disciplines. The current researches that routinely use cell sorting include separating differentiated cells from pluripotent cells[1], studying cell fate and function[2], developing new biomarkers[3], and carrying out cell assays. Sorting stem cells from tissue cells is a critical step in tissue engineering and regenerative medicines. The immunogenicity and genomic instability of using naïve stem cells pose considerable safety concerns. Cell sorting allows purification of desired cell types and removal of cells that could harm the patients[4]. Cell fate and functions contain the underlying biological information in revealing disease symptoms, reactions to drugs, or physical stimuli, and other physiological events in living organisms. This information can help researchers to better understanding the root cause of diseases. Furthermore, isolation of abnormal cells can help to identify causes of diseases and to establish preventative measures and potentially eradication of the diseases. Biomarkers are essential in distinguishing cell populations. Cells are naturally heterogeneous and have many overlapping properties. Consequently, new biomarkers such as cell mechanical properties are always needed to differentiate the overlapping characteristics

which can lead to new discoveries in cell biology. There is a growing demand for microfluidic cell-sorting platforms that can test and explore new biomarkers. Cell assays are analytical procedures that frequently apply multiple tests that run in parallel which analyze sub-cellular contents such as proteins, genetic materials, and macromolecules. Cell sorting technologies can be integrated with existing cell assays to improve the sensitivity of assay by enrichment and categorizing cells into subpopulations.

Most drug development starts with cell models[5]. The early stage of drug tests is carried out *in vitro* on selected cells with well-defined properties. The results of drug trials often are affected by the cell sample purity. However, obtaining a pure population of desired cells is a challenging task. Normally, a mixture of cells of different types are cultured and harvested. The cell mixture is then subjected to isolation or purification which is a key step in the upstream part of the bioprocessing. In the bioprocessing industry, the most commonly employed practice is centrifugation where cells having difference in size, density or mass are stratified into layers in centrifuge tubes and extracted. However, centrifugation is a crude cell separation method because the boundary between cell layers is not well-defined. In order to obtain high purity, cells near the interface are disregarded. In addition, the final yield of purity is limited by the overlapping cell properties. New cell sorting platforms can improve cell purity by utilizing new biomarkers such as cell elasticity, which can be a surrogate that indicates abnormalities in cytoskeletal or nuclear properties. Furthermore, cells can be further separated into subgroups which create new cell models that are inaccessible with traditional centrifugation techniques[6].

Cell-based therapy uses cellular materials such as metabolites or whole cells[7] in intervention procedures (Figure 6.1). For example, in immunotherapy, T-cells capable of fighting infections and cancers are injected into patients. Stem cell therapy is another example where

patient's own stem cells are used to treat pathologic conditions. For example, bone marrow transplants are commonly used in the treatment of life-threatening leukemia. Moreover, gene therapy uses viral vectors derived from packaging cell lines to deliver DNA into patient's cells. The packaging cells are harvested from a mixture of cells and the purity of the packing cells affects the quality of viral vectors. Another application is stem cell or cord blood cell banking where the mother's fetal cells are stored for future use. All aforementioned therapeutic interventions require cell sorting and purification. The purity of the enriched cells has tremendous impact on patient outcomes.

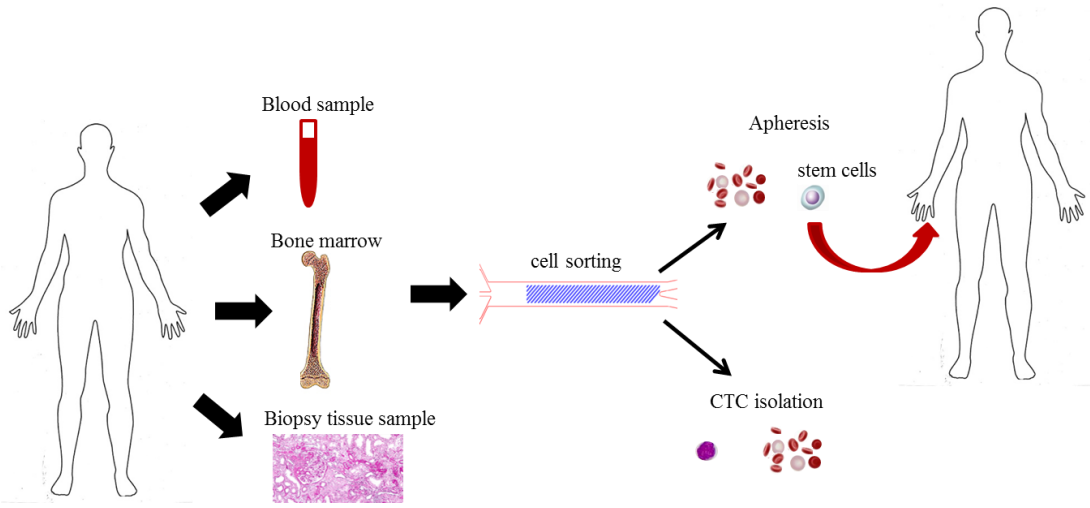

Figure 6.1. Applications of microfluidic cell sorting: apheresis of stem cells and circulation tumor cell isolation.

Compared to traditional tissue biopsy and imaging based diagnostics, single cell analysis offers much higher sensitivity, the potential for early detection, and the genetic information that could provide prognosis[8]. Cell sorting is a crucial part of the single cell analysis that isolates target cells from a mixture of cells (Figure 6.1). For instance, circulating tumor cells are rare cells and normally can not be detected by conventional cell separation methods such as

centrifugation. With recently developed immunomagnetic cell sorting techniques, these rare cells (one in a billion) can be detected using less than 10 mL of blood samples[9]. Rare abnormal cells can sometimes signal diseases at early stages. Therefore, capturing rare abnormal cells in routine medical exams can lead to early detection[10]. In addition, the isolated cells can be further analyzed using PCR for comparative analysis of gene expression patterns[11].

In summary, cell sorting is central to many biological research and clinical applications. Although at early stage, microfluidic cell-sorting approaches already have shown promising results in exploring many previously uncharted territories of biomedical capabilities. The continued efforts in developing microfluidic cell sorters will improve cell-sorting specificity, sensitivity and throughput. In the near future, we will see wide usage of microfluidic cell sorting in both research and clinical settings.

6.3 Limitations and Potential Solutions

Cell populations can be heterogeneous in size, stiffness, viscosity and other characteristics. More often, the heterogeneity is more pronounced in patient samples than cell lines. Consequently, cell separation based on biophysical properties depends on multiple convoluted and overlapping properties and relying on any single cell property to separate cells under realistic conditions is difficult. Due to these natural variations, achieving high specificity in cell sorting is challenging when cell biophysical properties are used alone. For instance, HL60 and leukocytes have large overlap in cell viscosity. In another instance, although the viscosity is different for Jurkat and HL60 cells, the relaxation for the soft Jurkat cells is similar to the viscous

HL60 cells. For these cell pairs, solely using these biophysical signatures would prove difficult for separation.

Our research effort is primarily focused on cell separation utilizing multiple cell biophysical properties whether it is cell stiffness, cell viscosity or cell size. However, like all single-property cell sorting methods, overlapping properties is a major limitation to the use in practical applications and a single property may be insufficient to achieve a high level of specificity. For example, breast and ovarian cancer cells have similar stiffness; therefore it is unlikely that stiffness alone is able to distinguish these two types of cancer. Due to the complex nature of cells, we need to combine several other cell characteristics such as cell size, adhesion properties as well as biomolecular markers to accurately identify cell subpopulations. One solution is to combine these biophysical and biomolecular markers in series. This multi-faceted approach can boost both sensitivity and specificity of the single cell analysis (Figure 6.2).

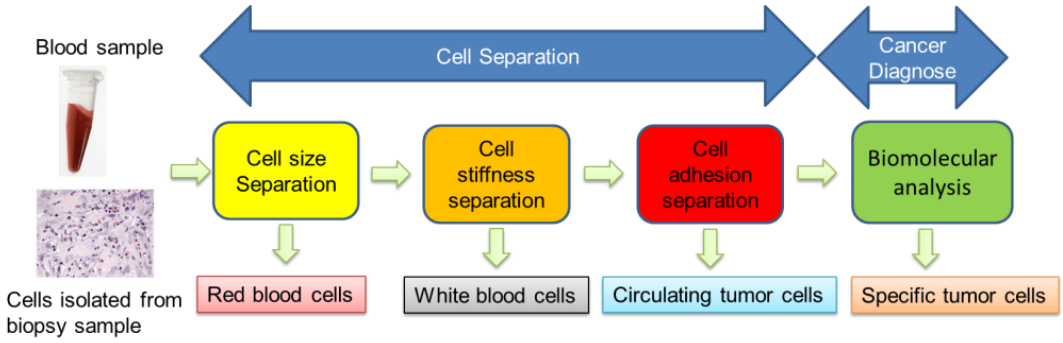

Figure 6.2. An integrated multistage single cell analysis. Cell sorting can be divided into multiple stages to achieve superior enrichment and specificity. The sensitivity of the downstream biomolecular analysis will be improved due to high purity of target cells at the input.

Although red blood cells can be separated from cells that are larger, sorting healthy red blood cells from diseased red blood cells based on stiffness is a challenging task. First, unlike

other types of cells, red blood cells are not spherical; instead, they are biconcave discs. Therefore, when they are compressed the cell deformation is quite different from spherical cells. For instance, the red blood cells did not roll along the ridges but were trapped underneath the ridges. Second, the red blood cells are much smaller. Although their diameter is about 8 μm, their thickness is only about 3 μm. During the compression, the cells are deformed in the direction of their thickness. As a result, the cell trajectory is extremely sensitive to the gap size. Unlike other cell sorting experiment where a 1 μm deviation in the gap size is less significant, the inaccuracy in gap size has major impact on red blood cell trajectory. We have tested channels with 2 μm and 4 μm gap sizes. In a 2 μm gap channel, red blood cells quickly "piled up" at the ridges and the channel was clogged whereas in a 4 μm channel, both soft red blood cells and drug stiffened red blood cells flowed through the channel without noticeable difference in their trajectories. To successfully sort red blood cells of different stiffness, we need to have a better understanding of the relationship between cell deformation and cell trajectory. In addition, we need to fabricate the channels with high precision. Further, the ridge width should be reduced to decrease cell-ridge contact surface so that cells are less liked to be trapped underneath the ridge.

To improve cell sorting throughput, multiple channels can be utilized simultaneously in parallel. In addition, the width of the channels can also be expanded so that cell-cell interaction is avoided when higher concentrations of cells are injected into the microfluidic cell sorter. Sensitivity can be improved by connecting several microfluidic channel designs in series to sort individual cell types in each channel. Finally specificity can be improved by implementing additional outlets to allow finer fractionation of the cell samples.

Table 6.1 provides comparisons of a list of microfluidic cell separation methods including our newly developed cell sorter.

Table 6.1 Comparisons of microfluidic cell separation methods.

Microfluidic Cell Separation Comparisons				
Method	Sensitivity and Specificity (cell purity)	Separation Criteria	Throughput	Cost
Fluorescent-activated cell sorting[12-14]	>90%	Fluorescence	>1,000 cells per second	High
Magnetic-activated cell sorting[15,16]	>80%	Magnetic properties	>1,000 cells per second	High
Dielectrophoresis[17,18]	>70%	Intrinsic charge and size	>10,000 cells per second	High
Acoustophresis[19,20]	>80%	Size and density	>3,000 cells per second	High
Deterministic flow[21,22]	>90%	size	>40,000 cells per second	Low
Constrictive filtration[23,24]	>70%	Stiffness and size	<300 cells per second	Low
Hydrodynamic filtration[25,26]	>90%	Size	>2,000 cells per second	Low
Inertial microfluidics[27,28]	>90%	Stiffness and size	<500 cells per second	Low
Our microfluidic cell sorter	>90%	Stiffness, viscosity and size	~1000 cells per second	Low less than $0.60 per chip

6.4 Conclusion

Microfluidic cell sorting is an important analytical tool that contributes significantly to the discovery of new frontiers in biological research and advancement in clinical applications. Microfluidic cell sorting is also the key to unlock many mysteries of genetic materials of

individual cells. Furthermore, microfluidic cell sorters can utilize newly developed biomarkers to discover previously undetected cell subpopulations. However, the technology development of microfluidic cell-sorting is still at infant stage. There is much more to be learned. The links between diseases, cell properties, and cell functions have produced a wealth of information for motivating the development of new microfluidic cell sorters. The major challenges are overcoming the vast natural-occurring heterogeneity among cell populations and being able to distinguish cell subpopulations that have multiple convoluted cell properties. The future research effort should focus on improving the three competing criteria: specificity, sensitivity and throughput. Specificity refers to the selection or enrichment of targeted cells in high purity. Sensitivity refers to isolation of rare cells in a cell mixture that contains many other types of cells. Throughput means the amount of samples or number of cells can be analyzed per unit time. The ultimate goal for microfluidic cell-sorting is to sort cells in highly complex and heterogeneous samples and output high purity of subpopulations of cells in short processing time at low cost.

6.5 References

1. Roda B, Reschiglian P, Zattoni A, Alviano F, Lanzoni G, et al. (2009) A Tag-Less Method of Sorting Stem Cells from Clinical Specimens and Separating Mesenchymal from Epithelial Progenitor Cells. Cytometry Part B-Clinical Cytometry 76B: 285-290.
2. Ekpenyong AE, Whyte G, Chalut K, Pagliara S, Lautenschlager F, et al. (2012) Viscoelastic Properties of Differentiating Blood Cells Are Fate- and Function-Dependent. Plos One 7: 9.
3. Mao XL, Huang TJ (2012) Exploiting mechanical biomarkers in microfluidics. Lab on a Chip 12: 4006-4009.
4. Basma H, Soto-Gutierrez A, Yannam GR, Liu LP, Ito R, et al. (2009) Differentiation and Transplantation of Human Embryonic Stem Cell-Derived Hepatocytes. Gastroenterology 136: 990-999.
5. Gutova M, Najbauer J, Gevorgyan A, Metz MZ, Weng YH, et al. (2007) Identification of uPAR-positive Chemoresistant Cells in Small Cell Lung Cancer. Plos One 2: 2.
6. Shah AN, Summy JM, Zhang J, Park SI, Parikh NU, et al. (2007) Development and characterization of gemcitabine-resistant pancreatic tumor cells. Annals of Surgical Oncology 14: 3629-3637.
7. Dewitte T, Hoogenhout J, Depauw B, Holdrinet R, Janssen J, et al. (1986) Depletion of donor lymphocytes by counterflow centrifugation successfully prevents acute graft-versus-host disease in matched allogeneic marrow transplantation. Blood 67: 1302-1308.
8. Andersson H, van den Berg A (2003) Microfluidic devices for cellomics: a review. Sensors and Actuators B-Chemical 92: 315-325.
9. Cristofanilli M, Budd GT, Ellis MJ, Stopeck A, Matera J, et al. (2004) Circulating tumor cells, disease progression, and survival in metastatic breast cancer. New England Journal of Medicine 351: 781-791.
10. Xu Y, Phillips JA, Yan JL, Li QG, Fan ZH, et al. (2009) Aptamer-Based Microfluidic Device for Enrichment, Sorting, and Detection of Multiple Cancer Cells. Analytical Chemistry 81: 7436-7442.
11. Sanchez-Freire V, Ebert AD, Kalisky T, Quake SR, Wu JC (2012) Microfluidic single-cell real-time PCR for comparative analysis of gene expression patterns. Nature Protocols 7: 829-838.
12. Cho SH, Chen CH, Tsai FS, Godin JM, Lo YH (2010) Human mammalian cell sorting using a highly integrated micro-fabricated fluorescence-activated cell sorter (mu FACS). Lab on a Chip 10: 1567-1573.
13. Wolff A, Perch-Nielsen IR, Larsen UD, Friis P, Goranovic G, et al. (2003) Integrating advanced functionality in a microfabricated high-throughput fluorescent-activated cell sorter. Lab on a Chip 3: 22-27.
14. Wang MM, Tu E, Raymond DE, Yang JM, Zhang HC, et al. (2005) Microfluidic sorting of mammalian cells by optical force switching. Nature Biotechnology 23: 83-87.
15. Xia N, Hunt TP, Mayers BT, Alsberg E, Whitesides GM, et al. (2006) Combined microfluidic-micromagnetic separation of living cells in continuous flow. Biomedical Microdevices 8: 299-308.
16. Pamme N, Wilhelm C (2006) Continuous sorting of magnetic cells via on-chip free-flow magnetophoresis. Lab on a Chip 6: 974-980.

17. Hu XY, Bessette PH, Qian JR, Meinhart CD, Daugherty PS, et al. (2005) Marker-specific sorting of rare cells using dielectrophoresis. Proceedings of the National Academy of Sciences of the United States of America 102: 15757-15761.
18. Pommer MS, Zhang YT, Keerthi N, Chen D, Thomson JA, et al. (2008) Dielectrophoretic separation of platelets from diluted whole blood in microfluidic channels. Electrophoresis 29: 1213-1218.
19. Yang AHJ, Soh HT (2012) Acoustophoretic Sorting of Viable Mammalian Cells in a Microfluidic Device. Analytical Chemistry 84: 10756-10762.
20. Shi JJ, Huang H, Stratton Z, Huang YP, Huang TJ (2009) Continuous particle separation in a microfluidic channel via standing surface acoustic waves (SSAW). Lab on a Chip 9: 3354-3359.
21. Green JV, Radisic M, Murthy SK (2009) Deterministic Lateral Displacement as a Means to Enrich Large Cells for Tissue Engineering. Analytical Chemistry 81: 9178-9182.
22. Holm SH, Beech JP, Barrett MP, Tegenfeldt JO (2011) Separation of parasites from human blood using deterministic lateral displacement. Lab on a Chip 11: 1326-1332.
23. Zhang WJ, Kai K, Choi DS, Iwamoto T, Nguyen YH, et al. (2012) Microfluidics separation reveals the stem-cell-like deformability of tumor-initiating cells. Proceedings of the National Academy of Sciences of the United States of America 109: 18707-18712.
24. McFaul SM, Lin BK, Ma HS (2012) Cell separation based on size and deformability using microfluidic funnel ratchets. Lab on a Chip 12: 2369-2376.
25. Yamada M, Kano K, Tsuda Y, Kobayashi J, Yamato M, et al. (2007) Microfluidic devices for size-dependent separation of liver cells. Biomedical Microdevices 9: 637-645.
26. Hou HW, Bhagat AAS, Chong AGL, Mao P, Tan KSW, et al. (2010) Deformability based cell margination-A simple microfluidic design for malaria-infected erythrocyte separation. Lab on a Chip 10: 2605-2613.
27. Wu ZG, Willing B, Bjerketorp J, Jansson JK, Hjort K (2009) Soft inertial microfluidics for high throughput separation of bacteria from human blood cells. Lab on a Chip 9: 1193-1199.
28. Hur SC, Henderson-MacLennan NK, McCabe ERB, Di Carlo D (2011) Deformability-based cell classification and enrichment using inertial microfluidics. Lab on a Chip 11: 912-920.

APPENDIX A

THREE DIMENSIONAL PARTICLE TRACKING USING HIGH-SPEED MICROSCOPY

In order to understand what factors affect cell trajectory, we needed a method to accurately record cell trajectory inside the microfluidic channel. Depending on flow pressures and channel designs, cells normally flow at the speed on the order of meters per second. Traditional video microscopy fails to capture the details of cells moving through the channel. Thus, a high-speed microscopy which can take several thousands of frames per second is a good candidate for cell tracking. There are a plenty of high-speed velocimetry methods published in the literature[1,2]. However, many of them require sophisticated equipment such as laser beams and delicate setup.

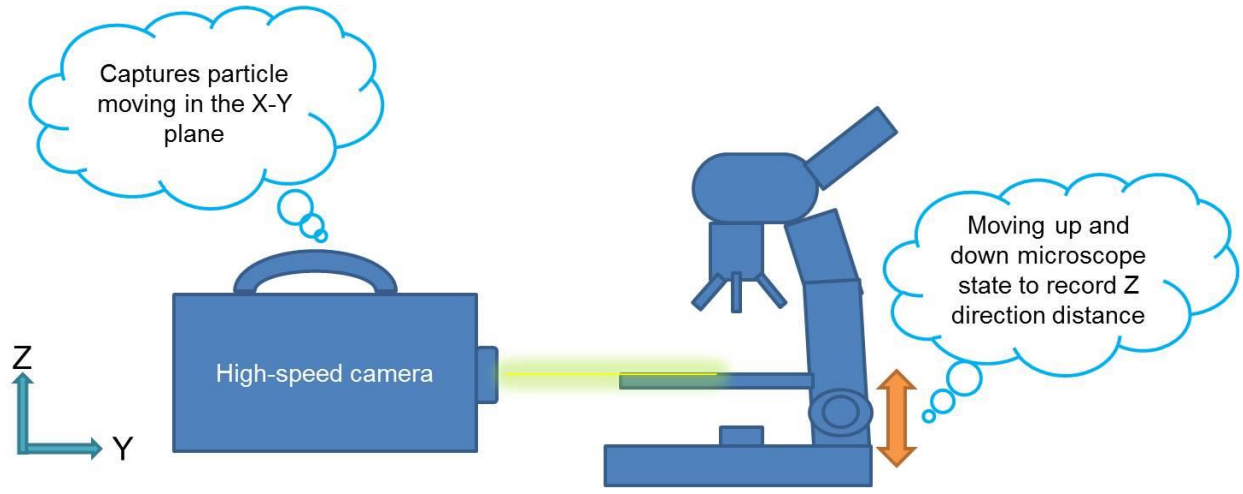

Figure A1. A customized high-speed video micrograph acquisition system. Cells moving through the microfluidic cell sorters can be captured through an inverted microscope and a single high-speed camera.

We developed a simple algorithm that can track particles/cells using a single high-speed camera mounted on an inverted microscope (Figure A1). The algorithm analyzes a series of two

dimensional images taken from video microscopy and extract three-dimensional data to track particles in all three dimensions during flow. We correlate the size of a particle in an image to a z-position through linear interpolation to determine the instantaneous z-position at any given point in time. Control images are taken at fixed distances relative to the focal plane of the microscope and used to obtain the correlation between the particle size and the particle's z-position relative to the focal plane. The digital images are decomposed to three-dimensional data matrices and analyzed with MATLAB as the scripting language (Figure A2). Using this method we are able to use a single camera bright field microscopy system to track particles in all three dimensions.

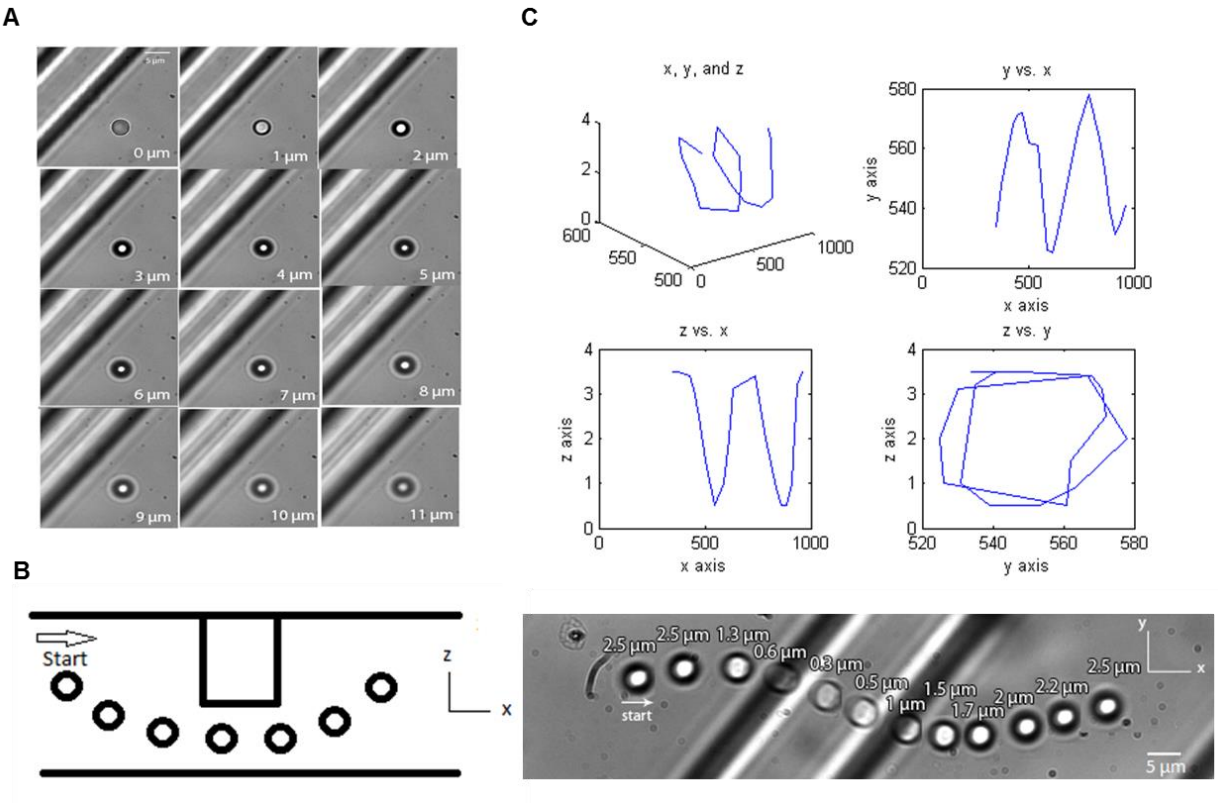

Figure A2: Three-dimensional particle tracking. (A) A 6 µm particle was fixed onto the bottom of the microchannel. A stack of 12 frames were taken at increasing height to create a global reference. The top left was positioned at 0 µm when the particle was focused and the bottom right was positioned at 11 µm which was the maximum height that a particle could travel, with

all other frames lying 1 μm increment. (B) Schematic of the side view (left) of the particles when it travels underneath the ridge. Particles move in and out of focus when travelling underneath the ridge (right). (C) A full three-dimensional particle trajectory can be seen in the top left corner, while other graphs show the trajectory of individual planes.

References

1. Santiago JG, Wereley ST, Meinhart CD, Beebe DJ, Adrian RJ (1998) A particle image velocimetry system for microfluidics. Experiments in Fluids 25: 316-319.

2. Olsen MG, Adrian RJ (2000) Out-of-focus effects on particle image visibility and correlation in microscopic particle image velocimetry. Experiments in Fluids 29: S166-S174.